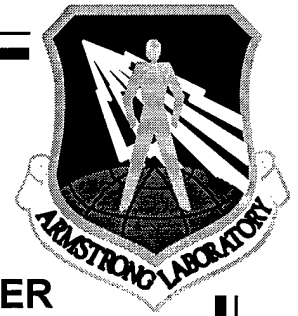


USAFSAM-TR-90-8



**EFFECTS OF ACUTE AND PROLONGED MILLIMETER
WAVE RADIATION EXPOSURE UPON CORNEAL
ENDOTHELIAL MORPHOLOGY**

**Roger P. Farrar
Kenneth R. Diller
H. Grady Rylander**

**University of Texas
Department of Kinesiology & Health Education
Austin, TX 78712**

**USAF SCHOOL OF AEROSPACE MEDICINE
Human Systems Division
2602 West Gate Road
Brooks Air Force Base, Texas 78235-5252**

June 1990

Final Technical Report for Period January 1989 to December 1989

Approved for public release; distribution is unlimited.

DTIC QUALITY INSPECTED 3

**AIR FORCE MATERIEL COMMAND
BROOKS AIR FORCE BASE, TEXAS**

**ARMSTRONG
LABORATORY**

19970707 100

NOTICES

When Government drawings, specifications, or other data are used for any purpose other than in connection with a definitely Government-related procurement, the United States Government incurs no responsibility or any obligation whatsoever. The fact that the Government may have formulated or in any way supplied the said drawings, specifications, or other data, is not to be regarded by implication, or otherwise in any manner construed, as licensing the holder or any other person or corporation; or as conveying any rights or permission to manufacture, use, or sell any patented invention that may in any way be related thereto.


The mention of trade names or commercial products in this publication is for illustration purposes and does not constitute endorsement or recommendation for use by the United State Air Force.

The Office of Public Affairs has reviewed this report, and it is releasable to the National Technical Information Service, where it will be available to the general public, including foreign nationals.

This report has been reviewed and is approved for publication.

Government agencies and their contractors registered with Defense Technical Information Center (DTIC) should direct requests for copies to: Defense Technical Information Center, 8725 John J. Kingman Rd., STE 0944, Ft. Belvoir, VA 22060-6218.

Non-Government agencies may purchase copies of this report from: National Technical Information Services (NTIS), 5285 Port Royal Road, Springfield, VA 22161-2103.


MICHAEL R. MURPHY, Ph.D.
Chief, Radiofrequency Radiation Division

REPORT DOCUMENTATION PAGE

Form Approved
OMB No. 0704-0188

Public reporting burden for this collection of information is estimated to average 1 hour per response, including the time for reviewing instructions, searching existing data sources, gathering and maintaining the data needed, and completing and reviewing the collection of information. Send comments regarding this burden estimate or any other aspect of this collection of information, including suggestions for reducing this burden, to Washington Headquarters Services, Directorate for Information Operations and Reports, 1215 Jefferson Davis Highway, Suite 1204, Arlington, VA 22202-4302, and to the Office of Management and Budget, Paperwork Reduction Project (0704-0188), Washington, DC 20503.

1. AGENCY USE ONLY (Leave blank)		2. REPORT DATE JUNE 1990	3. REPORT TYPE AND DATES COVERED FINAL, JANUARY 1989 - DECEMBER 1989	
4. TITLE AND SUBTITLE EFFECTS OF ACCUTE AND PROLONGED MILLIMETER WAVE RADIATION EXPOSURE UPON CORNEAL ENDOTHELIAL MORPHOLOGY			5. FUNDING NUMBERS C - F33615-87-D-0627 PR - 7757 TA - 01 WU - 1U PE - 62202F	
6. AUTHOR(S) FARRAR, ROGER P., DILLER, KENNETH R., RYLANDER, H. GRADY				
7. PERFORMING ORGANIZATION NAME(S) AND ADDRESS(ES) UNIVERSITY OF TEXAS DEPARTMENT OF KINESIOLOGY & HEALTH EDUCATION AUSTIN TX 78712			8. PERFORMING ORGANIZATION	
9. SPONSORING/MONITORING AGENCY NAME(S) AND ADDRESS(ES) USAF SCHOOL OF AEROSPACE MEDICINE HUMAN SYSTEMS DIVISION BROOKS AIR FORCE BASE, TX 78235-5301			10. SPONSORING/MONITORING USAFSAM-TR-90-8	
11. SUPPLEMENTARY NOTES				
12a. DISTRIBUTION/AVAILABILITY STATEMENT Approved for public release; distribution is unlimited.			12b. DISTRIBUTION CODE	
13. ABSTRACT (Maximum 200 words) The purpose of this research was to determine the injury threshold to the endothelium of the eye upon exposure to 35 GHz microwave radiation. The criterion for injury was defined as a statistically significant increase in mean cell area of the endothelial cell of the cornea. The experiments were conducted at the microwave radiation facility at Brooks AFB, TX. Four cats were each exposed to 10 mW/cm ² for 2 hours/day on alternative days, over a period of 2 weeks, for a total of 6 exposures per cat (12 hours of total exposure per cat). When the digitized images of the endothelial cells, obtained by noncontact specular microscopy, were examined and compared to that of control cats, no change in mean cell area of the endothelium of the exposed eye was detected. Four additional cats were exposed to 100 mW/cm ² for 2 hours per day on alternative days over a period of 2 weeks for a total of 12 hours of exposure per cat. In a like manner the digitized images of the endothelial cells were compared to those of control cats. No changes in the mean cell size of the endothelial cells were detected, either immediately or up to 2 weeks after the last exposure. The original protocol was to increase the energy deposition to the eye to 500 and 1000 mW/cm ² and subsequently determine the threshold of damage to the endothelium of the eye. We were unable to increase the energy deposition to the cat because a focusing lens for the microwave generator is still being developed for the radiofrequency (RF) facility at Brooks Air Force Base. The dosimetry conducted on site indicated that the cats would receive too much overall RF radiation to allow us to attribute damage to the endothelium of the eye solely to the microwave effects upon the cornea. Therefore, the threshold of damage to the endothelium of the cornea induced by RF radiation, as evaluated by change in mean cell area of the endothelial cells, is above 100 mW/cm ² .				
14. SUBJECT TERMS Corneal endothelium; Millimeter wave bioeffects; Millimeter wave radiation			15. NUMBER OF PAGES 157	
			16. PRICE CODE	
17. SECURITY CLASSIFICATION OF REPORT UNCLASSIFIED	18. SECURITY CLASSIFICATION OF THIS PAGE UNCLASSIFIED	19. SECURITY CLASSIFICATION OF ABSTRACT UNCLASSIFIED	20. LIMITATION OF ABSTRACT UL	

NSN 7540-01-280-5500

Standard Form 298 (Rev 2-89) Prescribed by ANSI Std Z-39-18
298-102 COMPUTER GENERATED

TABLE OF CONTENTS

INTRODUCTION	1
1.1 Radiofrequency Radiation.....	1
1.2 RFR Characteristics.....	2
1.3 Ocular Effects.....	3
1.3.1 Cataractogenesis	4
1.3.2 Contradicting Findings.....	7
1.3.3 Whole Body Exposure Effects on Cataractogenesis.....	7
1.3.4 Corneal Endothelial Effects	8
1.3.5 Animal Study Conclusions.....	10
1.4 Analytical Solution for Human Ocular Damage.....	11
1.4.1 Human Ocular Damage Studies	12
1.5 Nonthermal Effects	12
1.6 Objectives.....	12
THEORETICAL CONSIDERATIONS	15
2.1 Bioheat Transfer Equation	15
2.2 Thermal Conduction.....	17
2.3 Convection to Ambient Air.....	19
2.4 Convection to Blood Flow	19
2.5 Heat Generation.....	21
2.5.1 Electrical Characteristics of the Tissue.....	23
2.5.2 Electrical Field Equations for a Planar Model.....	24
2.6.1 Theoretical Considerations for Endothelial Morphological Assessment.....	29
2.6.2 Techniques Used for Analyzing Endothelial Cell Morphology.....	32
2.7 Digital Image Processing Background.....	36
THERMAL MODEL DEVELOPMENT	39
3.1 Analytical Solutions	39
3.2 Developmental Stages	39

3.2.1 One-dimensional Model	41
3.2.2 Two-dimensional Axisymmetric Steady-state Model.....	43
3.2.3 High Resolution Two-dimensional Axisymmetric Transient Model Using SAR Patterns as the Forcing Function	48
3.2.3.1 Two-dimensional Axisymmetric SAR Forcing Function Model Results	53
SOFTWARE DEVELOPMENT FOR ENDOTHELIAL CELL ANALYSIS.....	65
4.1 Automated Cell Count and Area Measurement	65
4.1.1 Image Editing	83
4.2 Hand-traced Algorithm	88
COMPARISON OF AUTOMATED AND MANUAL METHODS FOR CELL SIZE AND DISTRIBUTION	91
EXPERIMENTAL METHODS AND MATERIALS FOR DATA COLLECTION AT THE RF FACILITY AT BROOKS AIR FORCE BASE, SAN ANTONIO, TEXAS.....	99
6.1 Animal Restraint and Hardware Specifications	99
6.1.1 Animal Selection	99
6.1.2 Experimental Apparatus.....	100
6.3 Endothelial Cell Morphology Acquisition	105
6.4 Thermal Data Acquisition	108
6.5 Thermal Camera Characteristics	108
6.6 Thermistor Digitization	109
EXPERIMENTAL RESULTS	113
7.1 Eye Temperature Experimental Results.....	113
7.2 Discussion of Experimental Thermal Results.....	116
7.3 Running the Code for the Thermal Modeling	117
7.4 Transient Two-dimensional Axisymmetric Model of the Eye Using Electromagnetic Power Absorption as a Forcing Function.....	119
7.5 Depth of Penetration.....	120
7.6 Computer Runs Using the Electrical Field as a Forcing Function.....	122

LIST OF FIGURES

Figure 2.1 Structures Of The Eye	29
Figure 2.2 Section Of Human Cornea	30
Figure 3-1 Steps In Model Development.....	40
Figure 3-2b One-Dimensional Finite Element Grid Of Eye Used To Investigate Boundary Conditions.....	42
Figure 3-3 Two Dimensional Steady-State Axisymmetric Model Used To Investigate Boundary Conditions.....	44
Figure 3-4 Steady-State Temperatures For The Axial Line Of Symmetry In The Eye For A Range Of Blood Perfusion Rates With Dirichlet Boundary Conditions At The Cornea	46
Figure 3-5 Steady-State Temperature Profiles Radially Through The Lens At Varying Perfusion Rates With Dirichlet Boundary Conditions At The Cornea	47
Figure 3-6 Physical Model Of The Eye	49
Figure 3-7 Finite Element Of The Eye	50
Figure 3-8 Measured Heat Generation Term As A Function Of Depth For The Eye And Head Of Monkey Exposed To 2.45 Ghz	52
Figure 3-9 Computed Temperature Contours For The Eye Exposed To 2.45 Ghz (Power Density 200mw/ Cm ²) For 2400 Sec Using The Thermal Properties Of Distilled Water For All Tissues	55
Figure 3-10 Computed Temperature Contours For The Eye Exposed To 2.45 Ghz (Power Density 200 Mw/Cm ²) For 2400 Sec Using Known Thermal Properties And Normal Perfusion Levels	56
Figure 3-11 Computed Temperature Contours For The Eye Exposed To 2.45 Ghz (Power Density 200 Mw/Cm ²) For 2400 Sec Assuming No Perfusion In The And Surrounding Tissues.....	57
Figure 3-12 Computed Temperature Contours For The Eye Exposed To 2.45 Ghz (Power Density 200 Mw/Cm ²) For 2400 Sec Assuming Perfusion Levels 10 Times Normal	60
Figure 3-13 Computed Temperature Contours For The Eye Exposed To 2.45 Ghz (Power Density 200 Mw/Cm ²) For 2400 Sec Assuming Normal Perfusion Rates In The Ciliary Body And Choroid And No Perfusion The Muscle And Fat	61
Figure 3-14 Computed Temperature Contours For The Eye Exposed To 2.45 Ghz (Power Density 200 Mw/Cm ²) 2400 Sec Assuming Normal Perfusion In The Ciliary Body And Choroid And With Perfusion And No Heat Generation In The Surrounding Fat And Muscle Layers	63
Figure 4.1.1 Original Image Obtained From The Slit Lamp	66

Figure 4.1.2 Original Image With Chosen Window Drawn	67
Figure 4.1.3 Windowing Algorithm Flowchart	68
Figure 4.1.4a Gray Level Histogram For The Window Of The Original Image	69
Figure 4.1.4b Gray Level Histogram Of Equalized Image.....	70
Figure 4.1.5a Equalized Image	71
Figure 4.1.5b Median-Filtered Image.....	71
Figure 4.1.6 Gaussian Filter.....	72
Figure 4.1.7 Histogram Of The Gray Levels To Be Thresholded	74
Figure 4.1.8 Simple Threshold To Obtain Binary Image	75
Figure 4.1.9a Original Image.....	75
Figure 4.1.9b Gray-Leveled Image.....	75
Figure 4.1.9c Adaptive Thesholding Image.....	75
Figure 4.1.9d Binary Image	75
Figure 4.1.10 Flowchart Of Algorithm Implemented To Obtain Binary Image Of Cell Centers	76
Figure 4.1.11 Flowchart Used In Obtaining The Edges Of The Cells From Their Centers.....	77
Figure 4.1.12 "Rolling Ball" Template Tij	78
Figure 4.1.13 Object Dilation Algorithm.....	80
Figure 4.1.14 Incomplete Cell Removal Algorithm	82
Figure 4.1a.1 Example Of An Image With Missing Boundaries	83
Figure 4.1a.2 Image Shown On Fig. 4.1a.1 After Editing	85
Figure 4.1a.4 Cell Area Distribution Obtained With The Automated Algorithm.....	86
Figure 4.1.14 Cell Area Distribution Of A Normal Corneal Endothelium	87
Figure 1. Area Of Hexagon	89
Figure 2. Area Of Triangle	89
Figure 3. Image With Hand-Traced Boundaries.....	90
Figure 5.1 Manual Traced Image With Binary Image Overlayed	91
Figure 5.1a Cell Area Distribution Of A Normal Cornea.....	92

Figure 5.1b Cell Area Distribution Of A Damaged Cornea.....	92
Figure 5.2 Mean Cell Area Comparison	94
Figure 6.1 Block Diagram Of Experimental Apparatus Used In Obtaining Thermal Data From The Eye Of Cats Being Exposed To Radiofrequency Radiation	101
Figure 6.2 Effects Of Anesthesia During 35 Ghz 10 Mw/Cm ² Exposure.....	103
Figure 6.3 Animal Set-Up And System Configuration For Obtaining Images	106
Figure 6.4 Configuration Of The Image Grabbing And Digitizing System	107
Figure 7.1 Measured Temperatures Within The Eye And Surrounding Tissue During 35 Ghz 125 Mw/Cm ² Exposure	114
Figure 7.2 Measured Temperatures Within The Eye And Surrounding Tissue During 35 Ghz 125 Mw/Cm ² Exposure.....	115
Figure 7.3 Calculated Heat Generation For The Lens Nucleus And Fat At 2.45 Ghz And Experimental Measured Heat Generation (SAR)	124
Figure 7.4 Calculated Heat Generation At 35 Ghz And 125 Mw/Cm ²	125
Figure 7.5 Computed Temperature Contours For The Eye Exposed To 2.45 (Power Density Of 125mw Cm ²) For 2400 Sec Using Electrical Field Equations As Forcing Function	126
Figure 7.6 Computed Temperature Contours For The Eye Exposed To 2.45 (Power Density Of 125mw Cm ²) For 2400 Sec Using SAR Pattern As Forcing Function	127
Figure 7.7 Computed Temperature Contours For The Eye Exposed To 2.45 (Power Density Of 125mw Cm ²) For 2400 Sec Assuming 10 Times Normal Perfusion	128
Figure 7.8 Computed Temperature Contours For The Eye Exposed To 2.45 (Power Density Of 125mw Cm ²) For 2400 Sec Assuming 10 Times Normal Perfusion	129
Figure 7.9 Temperature History For Node 298 Within Periobital Fat (35 Ghz And 125 Mw/ Cm ²).....	130
Figure 1 Typical Mean Cell Area Distribution Factor	135
Figure 2 Mean Cell Area For 10 Mw/Cm ² Exposure	136
Figure 3 Mean Cell Area For 100 Mw/Cm ² Exposure	137
Figure 4 Control Measurement	138

LIST OF TABLES

Table 1-1 Endothelial Damage Classification	9
Table 2-1 Thermal Conductivity, Density and Heat Capacitance for Eye Tissue	18
Table 2-2 Perfusion Rates for Eye Tissue.....	21
Table 2-3 Basal Metabolic Rates	23
Table 2-4 Permittivity and Conductivity of Tissue at 2.45 Ghz at 37C.....	27
Table 2-5 Permittivity and Conductivity of Rabbit Tissue at 35 Ghz at 37C	27
Table 2.6.1 Time Required for Technician to Measure Endothelial Cells with the Four Different Techniques .	35
Table 5.1 Comparison of Mean Cell areas obtained with the hand-traced and automated techniques from samples of cats (1-5) and rabbits (6-10) corneal endothelium. Each sample consisted of @100 cells.....	93
Table 6-1 Transmitter Characteristics at 35 Ghz and 94.5 Ghz.....	102
Table 7.1 Attenuation Constant, Characteristics Impedance, and Phase Angle at 2.45 Ghz and 35 Ghz.....	121

EFFECTS OF ACUTE AND PROLONGED MILLIMETER WAVE RADIATION EXPOSURE UPON CORNEAL ENDOTHELIAL MORPHOLOGY

Introduction

1.1 Radiofrequency Radiation

The use of radiofrequency radiation (RFR) in clinical applications such as hyperthermia and diathermy and in military applications such as radar and communications systems is becoming so widespread that the entire population is expected to be increasingly exposed to RFR at a wide range of frequencies and power densities. Despite a fairly intensive international research effort little is known about the biological effects of RFR. An area of research which is receiving an increased amount of attention is the thermal effects of RFR on biological systems. Although the exact nature of the deleterious effects of microwave radiation is not completely understood, most of the experimental data supports the concept that the effects are primarily due to elevated temperatures. Recent studies which have exposed cells and subcellular structures in vitro to relatively low levels of microwave radiation seem to indicate that nonthermal effects may be important [1]. However the relevance of extrapolating these results to in vivo systems is questionable due to factors such as penetration depth, geometry, large body mass and blood perfusion.

Thermal biological effects of RFR are more pronounced on the poorly vascularized surface of the human body. The eye is of particular interest because it is more susceptible to microwave injury than many other heat sensitive parts of the body. The eye is very vulnerable because it lies within the penetration depth of microwaves and it lacks effective cooling

mechanisms. Researchers have shown a direct relationship between microwave exposures exceeding 100 mW/cm^2 at 10 GHz and lens opacities in test animals [2,3]. Morphological changes in the endothelial cell layer of the cornea have been shown to occur at power densities as low as 10 mW/cm^2 at 2.45 GHz [4]. The retina may also be susceptible to RFR radiation, since degeneration of retinal neurons in rabbits has been reported at microwave power densities as low as 55 mW/cm^2 [5].

1.2 RFR Characteristics

The general term RFR is used to include other designations commonly found in the literature, such as microwave radiation, microwave fields, electromagnetic radiation, nonionizing electromagnetic radiation, electromagnetic fields and others. The frequencies of primary concern range from 10 kHz to 300 GHz.

RFR may be emitted in two forms: continuous wave (CW) or pulsed wave. A peak power generated by pulsed wave may be orders of magnitude greater than that of the same average power density for continuous wave. In a study done by Frei et al. [6], a direct relationship was found to exist between the average power density used in the two different exposure modalities and the increase in temperatures in different tissues. The pulsed RFR gave temperature increases ranging as high as 20 percent greater than the continuous wave. Their conclusion was that pulsed RFR consistently causes a greater change in temperature than CW RFR.

In the RFR-bioeffects literature, absorption of energy by a biological entity is generally quantified by the "specific absorption rate" (SAR). The SAR of a small volume at any locale within an entity is defined as the rate of

energy absorption per unit volume divided by the mean mass density of the volume, and is usually expressed in units of W/kg [7]. The use of phantom models with equivalent tissue characteristics was introduced by Guy [8]. The phantom models allow for experimental measurement of the SAR for different treatment protocols. Knowing the temperature increase, the heat capacity of the phantom, and the time of exposure the SAR is then calculated.

Theoretical and empirical studies by Johnson et al. [9] and Durney et al. [10] have demonstrated that the depth of penetration and absorption of RFR energy depends upon the electrical properties of the absorbing tissue which are a function of the frequency. Also, the depth of heat penetration depends greatly on the electrical and thermal properties of the tissue. Overall, the depth of penetration is less in tissues with high absorption rates and varies inversely with the frequency.

These studies give an overview of the general characteristics of RFR on biological entities. The effects of RFR on the eye can thus be said to be a function of the frequency, the type of RFR (CW or pulsed), and the electrical and thermal properties of the various eye tissues.

1.3 Ocular Effects

No clear standards exist for the exposure of humans to RFR. The interaction of RFR with humans is restricted to the surface of the body: skin, testes, superficial vessels, and the eye. One of the earlier studies on the effects of RFR exposure on the eye by Richardson, [11] and Daily [12,13] demonstrated that cataracts would result from acute exposures by application of the energy from a standard clinical diathermy applicator within a few inches of the eye. Their research was instrumental in setting the U.S. Army and Air Force

maximum permissible levels. Their investigations showed that power densities approximately equal to 100 mW/cm^2 was necessary to produce any effect of biological significance. Because of the uncertainties concerning the possible effects of certain variables, it was decided to include a safety factor of ten in the proposed safe level. On this basis the maximum exposure level of 10 mW/cm^2 was declared. This tolerance level still stands today.

1.3.1 Cataractogenesis

The first researchers to establish a power density vs. time dependency for the threshold of cataractogenesis in the eyes of rabbits was Williams et al. [4]. They found that cataracts could result from exposures as short as 5 minutes at exposure densities of 500 mW/cm^2 . Power densities of 220 mW/cm^2 required 4.5 hours of exposure to produce cataracts. No cataracts could be produced at exposure levels of 120 mW/cm^2 .

Carpenter [15] established a very precise time-power density dependency for the same exposure conditions based on a large number of acute experiments showing cataract formation for exposures varying from 600 mW/cm^2 for 3 min to 180 mW/cm^2 for 60 min. Carpenter, 1972, [16] investigated the question of cumulative effects with longer term or repeated exposures at lower levels. Carpenter found that exposures repeated from 4-15 times over intervals from 1-14 days resulted in a lower cataractogenic threshold of only 120 mW/cm^2 .

Kramar et al. [17] and Guy et al. [18] replicated Carpenter's work for single acute exposures with essentially the same results. They were also able to quantify the threshold level of cataractogenesis in terms of the

SAR and temperature distribution in the eye. Guy and co-workers, however, were not able to demonstrate the formation of cataractogenesis with repeated subthreshold power density exposures but were able to produce vacuoles in the lenses of the rabbits with repeated exposures at threshold power density levels applied at subthreshold time periods.

Kramar et al. [19] compared results of RFR exposure to rabbits and rhesus monkeys. Rabbits and monkeys were irradiated with 2.45 GHz resonant slot radiator for varying times of 10 minutes to 120 minutes to determine cataractogenic thresholds. Rabbits developed cataracts at power densities of 100 mW/cm². Monkeys sustained facial burns, but no lens damage, even at power densities of 500 mW/cm². Their results were substantiated by computer thermal models. The computer model used a finite element code, which divided the eye into a series of quadrilateral elements. The parameters which were included in the model were: thermal conduction, arterial heat transfer, and evaporation and convection from the eye surface. Kramar et al. used flow rates obtained by O'Day et al. [20] for the arterial heat transfer calculations. Kramar and co-workers also used the thermal conductivity values of the eye tissue obtained by White [21]. Heat transfer coefficients which assume no tearing and no blinking were given for convection to environmental temperatures by Kramar. The nodal network assumed a fixed retinal temperature of 37.1 C and ambient temperatures of 25 C. Numerical results for the rabbits showed an agreement between predicted values and assumed values for a basal total ocular blood flow of 2.7 cm³/min. Calculated isotherm regions revealed that temperatures peaked near the posterior surface of the lens.

Numerical results for the monkeys show that due to configuration of the facial bones the deposition patterns in the monkey are different than that of the rabbit. The local peaking of temperatures was not observed at the posterior surface of the lens but instead in the vitreous humor. Even at radiation levels of 300 mW/cm^2 the peak retrolental temperature was 40.2°C , in contrast to 45.1°C for the rabbit.

Kramar et al. concluded that at power levels of 300 mW/cm^2 (for ten minutes) and 200 mW/cm^2 (for twenty minutes) and 100 mW/cm^2 (for 120 minutes) damage was detectable in the rabbits. An assumed value of 42°C was the temperature at which no lens injury was to be expected which was determined in a previous study by Guy et al. [18]. For the monkeys, the critical temperature of 42°C was never reached within the lens even at power densities of 500 mW/cm^2 . Anatomical differences explained the disagreement in the temperature distributions between the two species. Whereas the rabbit has very exposed eyes and little surrounding skeletal protection, the monkey has deep-seated eyes shielded by well developed brows. Another factor is the dimension of the lens. The lens in the rabbit from anterior to posterior measures 7-8 mm while the rhesus monkey and in man the lens is about 4-5 mm thick. The smaller lens could thus be cooled better by the surrounding fluid. The study revealed that it is possible to predict the ocular temperatures and hence the cataractogenic thresholds for man due to the good agreement between the measured and the computed temperature fields if the blood flows and the SAR patterns are known. The SAR patterns can be obtained from model studies. However, there is currently insufficient data about the blood flow rates as a function of temperature to effectively predict if cataractogenic thresholds are reached.

1.3.2 Contradicting Findings

In another study done on monkeys by McAfee et al. [22] no deleterious effects were seen. The monkeys were trained to expose their face and eyes to pulsed RFR. An operandum-feeder that could be depressed by the animal's lips simultaneously caused the release of apple juice and activated a RFR generator. The pulsed RFR was at a frequency of 9.31 GHz and an average power density of 150 mW/cm². Twelve monkeys were individually irradiated during 30 to 40 sessions for up to 20 min/day and then observed for a year. Both a control group and an exposed group were used. These animals were given ocular examinations with a slit-lamp microscope. No cataracts or corneal lesions were ever observed. The researchers exposed a 150 ml volume of saline solution at near the same frequency and obtained a 2 C rise in the temperature. Thus, the absence of cataracts was consistent with the finding of Guy et al. that a 5 C temperature increase is needed for cataractogenesis.

1.3.3 Whole Body Exposure Effects on Cataractogenesis

Another important problem requiring attention was the question of possible cataractogenesis resulting from whole body exposures. Appleton [23] demonstrated that a whole body exposures at 3.0 GHz would be lethal to the rabbit at exposure levels insufficient to produce cataractogenesis or other ocular effects. Though considerable data now exist on cataractogenesis due to short-term exposures of the rabbits, the possibility of cumulative effects due to

long-term subthreshold power densities for cataractogenesis also remains an important question. Guy et al. [24] exposed rabbits daily for periods of 23 hours applied for 7 days a week for a full 6-month period, with food and water available ad lib. The whole-body exposures conditions were selected to allow maximum freedom of movement of the animal. In an earlier study, Appleton [25] demonstrated that the minimum lethal whole-body exposure for a rabbit was between 25-50 mW/cm². Guy et al., chose an exposure level of 10 mW/cm² to reduce the possibility of any type of acute effects in the animal. Periodic examinations of the eyes with a Nikon slit lamp microscope were made and the following parameters were monitored through the exposure period: body mass, urinary output, rectal temperature, hematocrit, hemoglobin, white cell count with differential and platelet count. No significant differences were found between experimental and control animals.

1.3.4 Corneal Endothelial Effects

Kues et al. [4] exposed the eyes of 7 monkeys to 2.45-GHz CW RFR and the eyes of 8 monkeys to 2.45-GHz Pulsed RFR (10us pulses at 100pps) in 4 hour sessions in anechoic chamber at an average power density of 5 to 30 mW/cm² with either weekly or daily sessions. Each monkey was examined with a specular microscope. Damage was assessed by a human counter observing the number of lesions in a field of 1 mm² in the central 6 mm² area of the cornea. The degree of endothelium damage was taken to be the number of lesions in the 1 mm² fields that had the most lesions. The overall damage was classified as:

Table 1-1.

Endothelium Damage Classification

Lesions	Classification
0-2	no change
3-10	minor change
11-50	moderate change
> 50	major change

The ocular examinations were done before the initial exposure and at variable time intervals after the exposure.

Seven monkeys were exposed to varying amounts of CW RFR in 4 hour sessions. The most rigorous exposures were at 20 mW/cm² (SAR of 5.2 W/kg) and 30 mW/cm² (SAR of 7.8 W/kg) on 4 consecutive daily 4 hour sessions which yielded a major change in the monkeys according to the damage classification above. A less rigorous study in which a monkey was exposed at 10 mW/cm² (SAR of 2.6 W/kg) for 56 weekly sessions yielded only a minor change in 1 of 12 ocular examinations.

Eight other monkeys were exposed to varying amounts of pulsed RFR in 4 hour sessions. The most rigorous study was done on a monkey exposed at 10 mW/cm² (SAR of 2.6 W/kg) for 4 series of 4 consecutive daily 4 hour sessions. The monkey showed major changes after each series. In a less rigorous study 11 weekly sessions at 10 mW/cm² (SAR of 2.6 W/kg) were performed on a monkey. The monkey exhibited minor or moderate changes in 6 of 11 examinations.

Five monkeys were sham-exposed for a total of 10 sessions. No endothelial damage was detected for any of these monkeys.

An electron microscope was used on four of the exposed monkeys after ocular damage was detected by the specular microscope. A transmission electron micrograph, magnification of 4000, of the corneal endothelium 48 hours after exposure at 10 mW/cm² (SAR of 2.6 W/kg) showed prominent intracellular vacuolization and gaps between the basal endothelial surface and Descemet's membrane. Based on the histology results and the specular microscope observations, the authors concluded that pulsed RFR was more effective in altering the corneal endothelium than CW RFR.

1.3.5 Animal Study Conclusions

Overall, the animal studies showed that there is a relationship between the average power density and the amount of damage within the lens and corneal endothelium. Also the duration of the exposure and the time between exposures are critical factors in determining if damage is going to occur. Also thresholds damage differs among species. The monkeys are more resilient than the rabbits due to anatomical differences. In general, for acute exposure to rabbit eyes threshold values in the order of 100 mW/cm² at 2.45 GHz are necessary to bring about an increase in temperature of 5 C or more which will cause lens damage [18]. Exposures of 500 mW/cm² at 2.45 GHz do not produce lens damage in Rhesus monkeys. At power densities above 500 mW/cm² the monkeys receive facial burns.

The effects of RFR on cataractogenesis and corneal endothelium damage will need to be assessed in future research. The studies by Kues and co-workers are novel because the damage to the corneal endothelium is

assessed rather than the damage to the lens as in earlier studies. The endothelium responds to injury by changes in morphology and hypertrophy [26]. It is an ideal organell for quantifying the relationship between RFR and cellular damage due to its uniformity and is accessable via specular microscopy.

1.4 Analytical Solution for Human Ocular Damage

The previous background literature presented investigated the effects of RFR on animal eyes. The impossibility of experiments on human beings causes a great difficulty in predicting safe levels of human exposure. Kadry et al. [27] presented an analytical solution for temperature distributions within the eye. The eye was assumed as a sphere and the heat diffusion equation was then solved in spherical coordinates. Temperature profiles were presented for different values of RFR heat generation, thermal conductivites, choroidal blood and ambient temperatures. A incident field at the surface of the cornea in terms of (V/m) was assumed causing the heat generation and the field decayed within the homogeneos spherical eye model. The thermal conductivity was taken to be an averaged value over the entire sphere. The effects of heating the tissue surrounding the eye were not investigated. The blood temperature within the choroid was assumed to be a function of the rise in temperature at the center of the eye. Effects due to blood perfusion within the choroid, ciliary body or surrounding tissue were not investigated. Also discussed were the differences in RFR induced temperature profiles and those due to direct heating of the cornea. The authors concluded that heating at the cornea directly negligibly effected the lens, whereas microwaves were

capable of lens injury because of their ability to penetrate into the body. No reference was made to corneal damage.

1.4.1 Human Ocular Damage Studies

Cases of ocular damage in humans due to occupational exposure has been cited in the literature. Hirsh and Parker [28], Zaret[29], and Issel and Emmerlich [30] investigated occupational hazards of RFR on the eye. Open to question in all the studies is the uncertainties regarding actual exposure frequencies, levels, and durations. In summary, most of the data on human eye exposure to RFR yields negative findings for cataractogenesis. The question of damage to corneal endothelium is still a matter of investigation.

1.5 Nonthermal Effects

Several researchers have proposed or have explained results of RFR interactions as being primarily nonthermal. The studies have covered many different topics such as calcium efflux, erythrocyte studies, cellular and subcellular effects. Most of the studies have been done in vitro and are hard to extrapolate to in vivo systems due to the aggregate structure of the tissue.

1.6 Objectives

The objectives of this research project were fourfold. First, to develop a suitable animal restraint apparatus which would allow exposure of a cat eye in vivo while being exposed to RFradiation andwhich would also allow non-contact specular microscopic record to be obtained of the corneal

endothelium or temperature profiles of the surface of the eye to be quantified by a thermal camera. Second, to develop a series of models to explain the energy deposition imposed by the RF radiation upon the eye. The first model used the finite element technique to predict isotherms given the power density and SAR patterns within the eye. This model could then be compared to experimental work and finite element work done by previous investigators for validity. The second model expanded the work done by previous investigators to include an investigation of a range of tissue parameters such as blood perfusion, thermal conductivities and natural convection coefficients. The third model was developed to predict isotherms within the eye using electrical field equations as a forcing function at high frequencies (frequencies greater than or equal to 2.45 GHz) and to compare this to experimental thermal data obtained for the eye at these high frequencies. Also, this electrical field model could then be compared to the model that uses 2.45 GHz SAR patterns for validity. The third objective was to develop an automated image analysis system in which the specular microscopic images could be captured, digitized, and analyzed in an automated way. The fourth objective was to determine a threshold energy level of RF radiation at which there were toxic effects observed on the cornea of the eye as determined by mean cell size and standard deviation about that mean.

THEORETICAL CONSIDERATIONS

2.1 Bioheat Transfer Equation

The temperature distribution in living tissue is characterized by a complicated combination of tissue parameters and by environmental influences. A common expression of this temperature distribution used to evaluate the thermal profiles within living tissue is the bioheat transfer equation first proposed by Pennes [31]. Several assumptions were necessary for bioheat transfer analysis. They include:

1) Blood flow is nondirectional at the capillary level, heat exchange between tissue and blood occurs only at this level. Blood perfusion in the ciliary body and choroid are uniform with respect to time. This assumption implies blood perfusion being unaltered throughout the exposure. It is known that blood perfusion increases with increased temperature and time and at some point blood perfusion reaches a static level. The assumption of constant blood perfusion is a simplification of the physiological reality but due to the stasis of blood perfusion at some temperature and time is a good assumption for high exposure densities and prolonged exposure times.

2) Local heat generation is nondirectional, and thermal and electrical properties are isotropic and homogeneous for each tissue.

3) Metabolic heat generation within the eye and surrounding tissue is important. Without the metabolic heat generation term and with no energy applied the tissue model tends to lose heat and arrive at steady-state temperature contours dependent on the ambient temperature. This basal

metabolic heat generation term is essential in investigating threshold levels of energy dosages that yield small changes in temperature.

4) The frequencies used, 2.45 GHz, and 35 GHz are high enough that the tissue is modeled as a lossy dielectric, exhibiting conduction and dielectric heating effects.

5) The experimental SAR patterns for 2.45 GHz are assumed to decay linearly, while the forcing function calculated from electrical field equations at 2.45 GHz, and 35 GHz is assumed to decay exponentially. The SAR pattern for the eye at 2.45 GHz was obtained experimentally by other investigators and was only obtained for an axial line through the center of the eye. This axial temperature profile has been extrapolated to apply to tissue other than that lying directly on the center line of the eye.

6) The RFR power per unit area at the surface of the eye and surrounding tissue is at a constant value. This is based on the assumption that the generated field is very homogeneous at the plane of the eye.

Subject to these conditions the bioheat equation can be written as:

$$\rho c(\partial T/\partial t) = \nabla \cdot (k \nabla T) + h \nabla T + \omega_b \rho_b c_b (T - T_b) + Q_s + Q_m \quad (2-1).$$

2.2 Thermal Conduction

The first term on the right-hand side of the equation represents the heat conduction due to a temperature gradient. Conduction of heat can take place in a material when different parts of the material are at different temperatures, and the direction of heat flow is always from points of higher to points of lower temperature. If in equation (2-1) a tissue has a large, k , the tissue is a good heat conductor, while if k is small, the material is a poor conductor or a good insulator. For the eye the tissue structure consist of the cornea, aqueous humor, lens, vitreous humor, ciliary body, fat, sclera, nerve and muscle. The values of the thermal conductivities used in equation (2-1) for each of the tissue types is given in Table 2-1.

The specific heat, c , is a constant that is dependent on the material properties of the tissue. The constant relates the heat needed to increase the temperature of a mass of a tissue by an incremental amount. Multiplying by the density yields the amount of heat per unit volume per incremental increase in temperature.

The highly myelinated optic nerve was assumed to be similar to brain white matter. Note that the thermal conductivity of the lens is approximately on third of that of water and the other eye tissues.

TABLE 2-1.

Thermal Conductivity , Density and Heat Capacitance for Eye Tissue

Tissue Type	Density (ρ) ^(a) (g/cm ³)	Heat Capacitance(ρc) ^(a) (J/cm ³ - ° C)	Thermal Conductivity(k) ^(b) k (W/cm- ° C)
Cornea	1.00	4.217	.0058
Aqueous Humor	1.00	4.217	.0058
Lens	1.00	4.217	.0021
Ciliary Body	1.00	4.100	.0042
Vitreous Humor	1.00	4.217	.0058
Optic Nerve	1.05	3.670	.0058
Choroid	1.00	4.217	.0058
Sclera	1.00	4.217	.0058
Fat	0.85	3.230	.0020
Water	1.00	4.217	.0058
Muscle	1.08	4.100	.0042
blood	1.05	3.630	-

(a) Ref. 32,33

(b) Ref. 34,35

(c) Ref. 30,31

2.3 Convection to Ambient Air

The next term, $h\nabla T$, represents the the transfer of heat by motion of the ambient air surrounding the eye. The heat lost or gained by a surface at one temperature in contact with air at another temperature depends on many factors, such as the shape and orientation of the surface, the nature of the air flow, and in this case the nature of the fluid flow over the eye. The cornea is assumed to be exposed to free convection to still air at 25 C. The convective heat transfer coefficient, h , for the cornea is assumed to be $.01 \text{ W/cm}^2\text{-C}$. The convective heat transfer coefficient for all other tissue exposed to the air was is assumed to be $.001 \text{ W/cm}^2\text{-C}$ [38].

2.4 Convection to Blood Flow

The next term, $\omega_b \rho_b c_b (T - T_b)$, represents the heat transfer by flow of the blood within the eye. Because the rise in tissue temperature is influenced by tissue blood perfusion rates, the effect on heating on the blood flow rates has a tremendous influence on the temperature contours within the eye. There is evidence that blood perfusion in skin can increase by a factor of 30 or more with elevation in tissue temperatures [39]. Tissue responds to heating by a prompt increase in blood flow. The detection of an increase or decrease in temperature is communicated through temperature receptors in the skin. The receptors transmit impulses to the medulla and hypothalamus. The hypothalamus in turn controls dilation by decreasing impulses via the sympathetic nervous system. The withdraw of sympathetic neurotransmitters such as norepinephrine allows smooth muscle and arteries to relax and causing vasodilation. Other sympathetic nerves release

acetylcholine which directs smooth muscles in the arterial walls to relax, causing dilation. Also, an increase in temperature directly induces vasodilation, as shown in nerve-free blood vessels [40]. High temperatures also trigger the release of compounds such as histamine and bradykinin that cause vasodilation. In short, heat is dissipated through the blood flow, the body utilizes a feedback mechanism in order to return to its normal temperature.

In a study by Dudar [41], the response of tissue blood flow below a critical temperature was found to be dependent on a temperature-time relationship. The critical temperature was found to be 45.7 C, when the temperature rose above 45.7 C then blood flow rates initially increased but eventually shut off completely. After this critical temperature is reached a finite exposure time at high temperatures causes damage. It is reasonable to assume that blood perfusion rates in the eye are also a bimodal function of temperature and time: however, since there is no experimental data available to describe the temperature dependence within the vascular tissue of the eye, perfusion rates in this study were varied over an order of magnitude to demonstrate the significant effects that increased levels of perfusion can have in cooling the eye during hyperthermia.

In the unheated eye, most of the heat conducted in the lens and vitreous humor comes via the blood flow from the ciliary body and the choroid. The temperature of the incoming blood is at or near core temperature. The temperatures within the eye are at lower temperatures because of the evaporation and convection at the surface of the eye; thus, the eye is at some steady-state condition with a resultant temperature distribution anterior to posterior. And this steady-state condition is determined by the environmental temperature and the arterial temperature. On the other hand,

the irradiated eye transfers heat to the blood in an attempt to maintain a homeostasis within the eye by the mechanisms discussed above. O'Day et al. [36] measured the flow of microspheres suspended in the arterial system and determined the flow rates during nonthermally loaded conditions. The flow rates were reported as percentages of the total blood supply to the eye: 72% for the choroid, retina and sclera; and 27% for the ciliary body . Table 2-2 gives the total blood supply for each tissue in (cm^3 blood/ sec-ml of tissue). The normal blood supply to the entire eye was assumed to be 0.045 cm^3 of blood/sec, and the volume of the eye was assumed to be 6.40 cm^3 .

TABLE 2-2.
Perfusion Rates for Eye Tissue

Tissue Type	Perfusion Rate (ω_b)(a) (cm^3 blood/sec- cm^3 tissue)
Ciliary Body	2.018×10^{-3}
Choroid	5.006×10^{-3}
Fat	2.917×10^{-3}
Muscle	8.036×10^{-3}

(a) Ref. 30,31

2.5 Heat Generation

Two terms on the right side of equation 2-1, Q_s and Q_m , define in order the heat generated due to exposure to RFR and heat generated due to metabolism. The term Q_s can be found experimentally by measuring the

energy dissipated at a position with a electromagnetic radiation monitor. Kramar et al. [19] measured the energy deposition for a frequency of 2.45 GHz within the eye. Figure 2-1 shows the SAR deposition pattern for this frequency. The SAR pattern was only obtained for an axial position through the center of the eye. No information is given on how the energy deposition changes within the eye and surrounding tissue as a function of distance from this axial line.

Measuring the true SAR pattern is relatively difficult for several reasons. Measuring precise values over small distances is difficult since the cross sectional area of the measuring probe, typically 1.4 mm, is large in comparison to tissue dimensions. Also, the electrical-magnetic field is perturbed an unknown amount during the measurement, and if one probe is used it must be inserted several times at different points within the tissue causing slight changes in the tissue properties.

The term, Q_m , defines the energy from cell metabolism. This term is a complicated function of the individual animal and is dependent on temperature, physiology, hormones and anatomy. Van't Hoff's equation [2], simplifies Q_m to be only a function of temperature:

$$M = M_0 (1.1)^{\Delta T} \quad (2-2)$$

where M_0 is the resting metabolic rate in (W/kg), and ΔT is the temperature rise. Table 2-3 gives the metabolic heat generation for known tissues. For the vitreous humor and aqueous humor metabolic heat generation was assumed to be negligible. The ciliary body and choroid metabolic heat generation values were assumed to be that of muscle and the heat generation values for sclera, cornea and lens were assumed to be similar to that of skin. The resting

metabolic rate was multiplied by the tissues density to arrive at a metabolic heat generation, Q_m , in units of (W/cm^3). These heat generation values are small relative to the energy influx, but they are necessary to maintain the correct temperature gradient within the eye if no energy is applied.

Table 2-3.
Basal Metabolic Rates

Tissue	M_o (W/g)
-----	-----
skin	.00100
fat	.00032
muscle	.00067

2.5.1 Electrical Characteristics of the Tissue

The term, Q_s , can also be calculated from the electromagnetic field equations. Tissue exposed to electromagnetic fields absorbs energy as a result of their electrical and magnetic properties. The Poynting vector relates the instantaneous power density flowing through the surface to the magnitudes of the fields:

$$S = (E \times H) \quad (2-3).$$

The amount of power deposited into a medium by the fields is determined by applying Stokes' theorem to equation (2-3):

$$P = \text{Re}\{(\sigma + j\omega\epsilon)|E^2| + j\omega\mu|H^2|\} \quad (2-4)$$

Biological systems exposed to high frequency RFR fields is represented as lossy dielectrics which have characteristics of both conductors and dielectrics. A lossy media is defined as a material in which the conductivity, σ , nor the permittivity, ϵ , dominate in the heating of the material. The general nature of the material can best be appreciated in terms of two limiting cases: (1) low-loss systems having $\sigma \ll j\omega\epsilon$ and (2) high-loss systems for which $\sigma \gg j\omega\epsilon$. For low-loss systems the material is considered a good dielectric, since the displacement current which represents energy storage is related to $j\omega\epsilon$. High-loss materials, on the other hand, are considered good conductors, since the conduction current which represents an energy loss mechanism is related to σ . Equation (2-4) gives the mathematical relationship of three distinct properties of media which undergo power absorption. The term, $\text{Re}\{\sigma E^2\}$, represents the power dissipated in a volume due to resistance; the term, $\text{Re}\{j\omega\epsilon|E^2|\}$ represents the energy stored in a volume due to the dielectric properties; and the term, $\text{Re}\{j\omega\mu|H^2|\}$, represents the energy stored in a volume due to the magnetic properties.

2.5.2 Electrical Field Equations for a Planar Model

The integration of the Poynting vector over a closed surface yields the total power crossing the surface in (W/cm^2). The direction of the vector \mathbf{S} indicates the direction of the instantaneous power flow at that point. Since \mathbf{S} is given by the cross product of \mathbf{E} and \mathbf{H} vectors this gives propagation at any point which is normal to both the \mathbf{E} and \mathbf{H} vectors. This gives for a uniform plane wave propagation through the eye in the z direction which is associated

with the E_x and H_y at the surface of the eye. Selecting a planar representation of heating of the eye is a good assumption in this study, since the RFR generated is highly uniform at the surface of the eye; thus, the E and H vectors are highly uniform in the x and y directions at the surface of the eye. This leads to the simplification of the electrical field equations to the field varying in only the z direction. This simplification also allows for a good comparison between the resulting heating isotherms from the linear SAR patterns obtained by Kramar et al. [19] and the resulting heating patterns from the electrical field equations in this study at the same frequency.

The polarized uniform plane waves of the E and H fields are given by:

$$E_x = E_{x0} e^{-\alpha z} \cos(\omega t - \beta z) \quad (2-4)$$

$$H_y = (E_{x0}/\eta) e^{-\alpha z} \cos(\omega t - \beta z) \quad (2-5).$$

Where α is the attenuation constant, η is the characteristic wave impedance and β the phase constant for lossy media. Materials subject to electromagnetic field exposure behave in different ways depending on their material properties. For example, conductors carry current with little resistance while dielectrics store electrical energy in the form of static charges, carrying little current. The variables α , β , and η are all dependent on the angular frequency (ω), the permittivity of the tissue (ϵ), the conductivity of the tissue (σ), and the magnetic permeability (μ) of the tissue.

$$\alpha + j\beta = j\omega(\mu\epsilon)^{1/2}[(1 - j\sigma/\omega\epsilon)^{1/2}] \quad (2-6)$$

$$\eta = [j\omega\mu/(\sigma + j\omega\epsilon)]^{1/2} \text{ (ohms)} \quad (2-7)$$

The coefficient, α , represents the attenuation of the electromagnetic field through the tissue in the z direction. The term, β , the phase constant, gives a relationship between the magnitudes of E and H . And, the characteristic impedance represents the intrinsic resistance of the tissue. The angular frequency is a parameter that is known and is related to the frequency by $\omega = 2\pi f$, where f is the operating frequency. The permittivity is a constant that relates the ability of a material to hold a charge between two parallel oppositely electrically charged plates-- capacitance. In this study the analogous components that correspond to the charged plates are the surface of the eye which is at some potential and some point within the skull which is at a lower potential. The process of charging this biological capacitor consists of transferring charge from the plate at higher potential to the plate at lower potential. The charging process therefore requires the expenditure of energy which leads to heating of the tissue. The conductivity is also a variable that is dependent on the frequency. The conductivity relates the ability of a material within an electric field to carry a current. The lower the conductivity of the material the greater the electric field needed to establish current density. The permittivity and the conductivity of eye tissue at 2.45 GHz and 35 GHz are given in Table 2-3 and Table 2-4 respectively.

Table 2-4.

Permittivity and Conductivity of tissue at 2.45 GHz at 37 C [43,44].

Tissue	Conductivity $\sigma(1/\text{ohm-m})$	Permittivity $\epsilon'(\text{F/m})$
muscle	1.6	50.5
saline	1.7	55.5
lens nucleus	1.1	30.0
fat	0.1	5.0

Table 2-5.

Permittivity and conductivity of rabbit tissue at 35 GHz and 37 C [45].

Tissue	Conductivity $\sigma(1/\text{ohm-m})$	Permittivity $\epsilon'(\text{F/m})$
saline	49.8	28.8
muscle	39.9	19.1
lens nucleus*	17.3	8.9
fat	3.6	2.7

* 23 C

$\epsilon = \epsilon' \epsilon_0$, where $\epsilon_0 = 8.85 \times 10^{-12} \text{ F/m}$

Since the electrical properties of the vitreous humor, cornea, aqueous humor, sclera and optic nerve are unknown, they were assumed to be that of the lens nucleus.

The magnetic permeability relates the ability of a material to be magnetically induced with another magnetic field. Biological tissue magnetic characteristics are that of paramagnetic materials. In a paramagnetic material with no external field applied the internal currents add to zero. But when a field is applied by an external source, the electron motion is altered by the induction of a macroscopic current by the changing magnetic flux. Since the eye is modeled as a paramagnetic material and μ for paramagnetic materials is slightly larger than μ_0 (the permeability of a vacuum), the permeability of eye tissue will be assumed to be μ_0 ($4\pi \times 10^{-7}$ H/m).

To find the time-average power density in W/cm², $\text{Re}(\mathbf{E} \times \mathbf{H})$ is integrated over one cycle and divided by the period [46].

$$P_{z,av} = (|E_{x0}|^2 e^{-2\alpha z} / 2 \eta_m) \cos^2(\theta_\eta) \quad (2-8)$$

where η is expressed in polar form $\eta = \eta_m \angle \theta_\eta$.

The volumetric power absorption in units of W/cm³ is the derivative of $P_{z,av}$, with respect to z .

$$P_{z,vol} = (|E_{x0}|^2 \alpha e^{-2\alpha z} / \eta_m) \cos^2(\theta_\eta) \quad (2-9).$$

Thus, the transient temperature distribution as a function of z is described by a modified bioheat transfer equation where the volumetric power absorption, P_{Vol} , is the heat source term, Q_s .

2.6.1. THEORETICAL CONSIDERATIONS FOR ENDOTHELIAL MORPHOLOGICAL ASSESSMENT.

The principal structures of the eye are shown in Figure 2.1. The outer protective layer of the eyeball, the sclera, is modified anteriorly to form the transparent cornea, through which light rays enter the eye. Inside the sclera is the choroid, a pigmented layer that contains many of the blood vessels which nourish the structures in the eyeball. Lining the posterior two-thirds of the choroid is the retina, the neural tissue containing the receptor cells. [47]

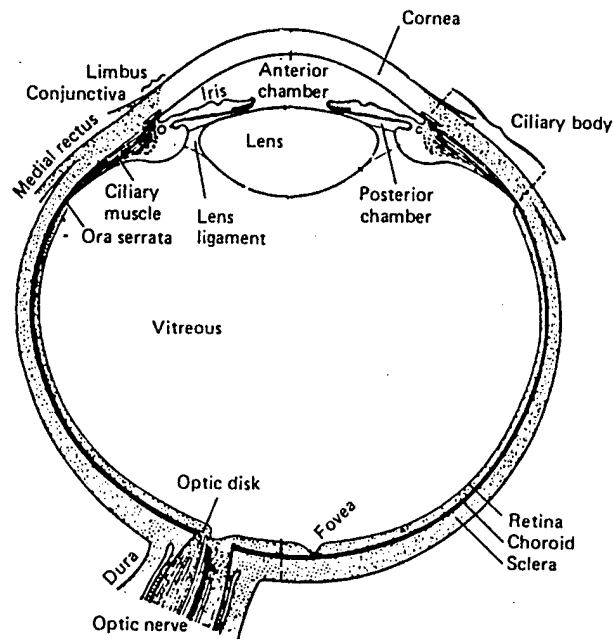


Figure 2.1. Structures of the eye.

The cornea is the transparent tissue at the anterior one-sixth of the eye. The cornea is made up of the stroma which is bounded externally by Bowman's membrane and the epithelium, and internally by Descemet's membrane and the endothelium (See Figure 2.2.) The total thickness in man is around 0.5 mm in the central region; in the periphery is around 0.75 mm

thick. The cells at the base are columnar, but as they are squeezed forward by new cells they become flatter. Three layers of cells can be recognized: basal, wing-shaped, and squamous cells. Replacement of cells occur by mitotic division, the average life of a cell being from 4 to 8 days [48].

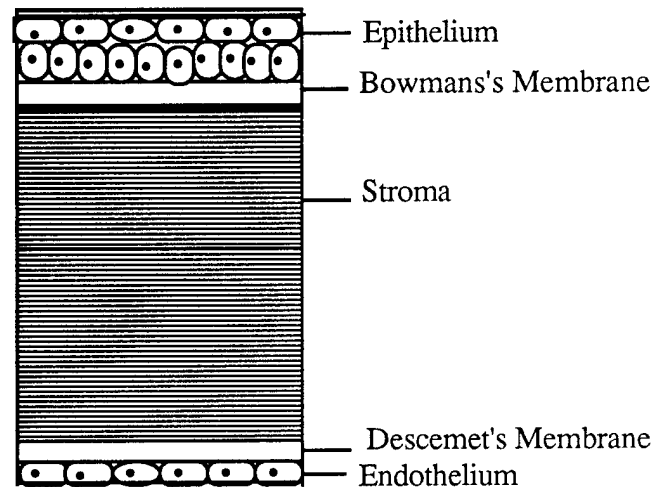


Figure 2.2. Section of human cornea.

The epithelium is 50μ to 90μ thick and covers the stroma anteriorly. Epithelial cells form the basal layer, become progressively flatter, and are shed from the superficial layer 7 days later.

The substantia propria, or stroma, constitutes 90% of the corneal thickness. Its anterior portion, the Bowman zone, is made up of collagen fibers that form an acellular region resistant to deformation, trauma, and the passage of foreign bodies or infecting organisms. Once destroyed, its typical

architecture does not restore, causing scarring or irregularity in corneal thickness that results in irregular astigmatism [48].

The endothelium is a single layer of flattened cells about 5 mm high and 20 mm wide with centrally located wide oval nuclei. The intercellular spaces are sealed off by tight junctions so that when colloidal material is introduced into the anterior chamber its passage is held up in these regions. The endothelium's main function is to control corneal hydration and nutrition with a leaky barrier formed by the apical gap and macula occludens junctions that keep some water out of the stroma but allow nutrient to pass [49]. Division of endothelial cells only occurs during growth and this is mitotic. During growth, multiplication of cells is faster than the area increase, that is why the cells become flatter. By contrast with the epithelium, the endothelial cells are normally a non-renewable population. They do not regenerate in adult humans. After damage, there is considerable mitotic division and neighboring cells flatten and spread into the damaged area [50]. Endothelial wound healing involves flattening and enlargement of cells to maintain an intact monolayer as well as production of abnormal collagenous material posterior to Descemet's membrane [49]. Injury to the endothelium (or epithelium) causes edema of overlying corneal stroma [48].

In a normal eye, the endothelial cells are densely packed (2,267 cells per square millimeter) and show a hexagonal appearance [51].

2.6.2. Techniques used for analyzing endothelial cell morphology.

In vivo, the corneal endothelium is exposed to a variety of abuses, each of which can produce cell damage. These include trauma, surgery, drugs, intraocular inflammation, and elevated intraocular pressure. Also, endothelial cell density decreases significantly with increasing age [52,53].

In 1968, D.M. Maurice developed the specular microscope to observe endothelial cells in situ [54]. Modifications were made by Laing, Sandstrom, and Leibowitz to obtain photographs of the endothelium in vivo [55].

Investigators have used the corneal specular microscope to evaluate the effects of various chemicals and surgical procedures on the corneal endothelium. The specular microscopic procedure examines approximately 0.04 mm^2 of the central corneal endothelium, which normally measures between 100 and 147 mm^2 [51]. Most investigators count the number of endothelial cells in a rectangle (fixed frame analysis) and report a cell density (cells per square millimeter). This method may be inaccurate, because cells that touch two sides of the rectangle are counted as whole cells, while those touching the other two sides are omitted from measurement. A counting method that outlines specific borders of a group of endothelial cells or of individual cells (variable frame analysis), such as planimetry or digitization, might be more precise. The technical training required for these methods could be minimized by using a cell sizer, which estimates endothelial cell size by visual comparison with cells of known size [56].

The four most common methods to measure endothelial cell density and area are: the rectangle, the planimeter, the digitizer and the sizer. The mode of operation for each one are described in the following paragraphs.

Rectangle. The rectangle outlines a known area so the number of endothelial cells in that area can be counted. Using a parallel ruler, a rectangle is drawn around a clear, continuous group of cells on the print. The cells that did not touch any of the borders of the rectangle were counted and then added to the cells that touched the left and top border. The number of cells per print, the dimensions of the rectangle, and the overall magnification of the print gave the cell density (cells per square millimeter) and the mean cell area (square micrometers.)

Planimeter. The planimeter traces the outline of a single cell or group of cells and measured their area directly. The planimeter will measure areas as small as 10 mm^2 . The magnifying glass on the arm of the planimeter blurred the cell borders enough to make it difficult to outline individual cells. Therefore, the cells have to be individually outlined with a felt-tip pen and numbered. The cell areas, the identification number of each individual cell, the number of cells in the group, and the overall magnification of the print are entered into the computer to calculate mean cell density and mean cell area. The computer can also print a frequency distribution histogram of the individual cell areas in $20 \text{ }\mu\text{m}^2$ intervals [55,56].

Digitizer. A digitizer records the X-Y coordinates of cell apices directly when the photograph is placed on an electronic grid and apices of the cell outline are touched with a pen. Then the operator enters the print

magnification, the number of cells in the group and the overall magnification of the print into the computer, which calculated areas of individual cells, mean cell density, and mean cell area. The computer then prints out a replica of the endothelial mosaic and a frequency distribution histogram of individual cell area in $20 \mu\text{m}^2$ intervals [56,57].

Cell Sizer. The cell sizer estimates the area by visual comparison of the endothelial photograph with a picture of cells of known size. It consists of a disc that contains 12 drawings of endothelial cells with known mean cell area, ranging from 50 to $1,980 \text{ mm}^2$. As the observer turns the disc, which is between two plastic plates, the successive patterns of cells and their mean areas appear in a window [56].

All four methods are very time consuming and labor-intensive. Each cell in the photograph has to be outlined and analyzed. This outlining takes a long time and is very stressful to the operator because regardless of the magnification used, the cells will still be of a relatively small size. Table 2.6.1 shows the time required to measure endothelial cells with the four different techniques [56].

	Technique	Time
Groups of Cells 5 prints/eye	Rectangle	30 min.
	Planimeter	30 min.
	Digitizer	30 min.
Individual Cells 100-150 cells/eye	Planimeter and computer	2 hr.
	Digitizer and computer	1 hr.
	Cell sizer	15 min.

Table 2.6.1. Time required for technician to measure endothelial cells with the four different techniques.

The most widely used method for counting corneal endothelial cells on specular micrographs is the Rectangle method, since it gives as precise results as the digitizer and planimeter and is the fastest and most inexpensive of the four methods. But many doctors agree [51] that the ideal method for measuring endothelial cells is computerized scanning, in which the image analyzer detects cell boundaries directly from the image and transmits the information into the computer.

2.7. DIGITAL IMAGE PROCESSING BACKGROUND

In the last few years, different computer algorithms have been developed to identify living organisms in various contexts. A number of automated systems are available to analyze different morphologies and body functions. Digital image processing is used in the medical imaging field to increase the usefulness of the images in their subsequent applications.

Image processing can be used for manifold purposes: from the basic data collection processes to image analysis, where boundary and shape detection algorithms in combination with heuristic methods are used for assuring that the final computed images are of biological significance [58-64]. For example, digital image processing is used for evaluating cardiac function using echocardiography via the analysis of shape attributes, such as the heart wall thickness or the shape change of the heart wall boundaries [62,63].

These algorithms can use a number of special shape discriminations techniques, such as the Hough transform [60,65] to identify boundaries in the presence of other image features that could easily be mistaken for the true boundaries, or simple thresholding to locate specific areas to detect edges [63]. In addition, after the features are segmented from the overall image, metric parameters are measured to quantify the size and shape [58,60,63,66]. Typically there is reasonably good control over the appearance of the image being analyzed; the objects in question are well separated on a featureless background and stains are used to give them optical densities. Under these

conditions, a combination of contour tracing and heuristic searching can effectively trace the boundaries of the cells of interest [61,62].

Image processing involves substituting visual analysis of an image. For example, in the past, morphologies were analyzed with very rudimentary techniques [66], looking at hundreds of images and trying to distinguish special features. In most cases, an image processing technique can be implemented to emulate the methodology used by the morphologists to analyze the images.

Some medical image processing packages are already in the market [67-69] but they work only on certain kinds of images. It is very hard to develop an algorithm that works universally because every image has its own characteristics, and must be treated differently.

Although many different image processing techniques have been developed, there is not a fully automated algorithm developed for analyzing corneal endothelial cell morphology. Obtaining a fully automated image processing is a very difficult problem due to the nature of these images. Slit lamp data have a great variation of light intensities and a poor gray level differentiation; common segmentation does not work on these kind of images. Also, since endothelial cells can lose their shape due to several factors mentioned before [70-71], a shape discrimination technique, like the Hough transform, is not useful in these kinds of images.

THERMAL MODEL DEVELOPMENT

3.1 Analytical Solutions

If the tissue properties, perfusion and heating rates are uniform and not dependent on temperature then the heat transfer equations can be solved analytically for simple geometries [27]. The eye and surrounding tissue have various tissue thermal and electrical properties and are of irregular geometry. Therefore, the finite element method a numerical procedure for solving steady-state and transient heat conduction problems with complex geometries and various tissue properties has been implemented to investigate RFR bioeffects.

3.2 Developmental Stages

Several stages of modeling went into developing a relatively high resolution two-dimensional axisymmetric model that included a electromagnetic volumetric power absorption forcing function. A flow chart representation of the stages involved in developing this particular heat transfer model is shown in Figure 3-1. This thought process could apply to any type of situation where a model is desired to faithfully predict a desired outcome given known input parameters. Modeling in the heat transfer biological realm is rather difficult because all of the input parameters may not

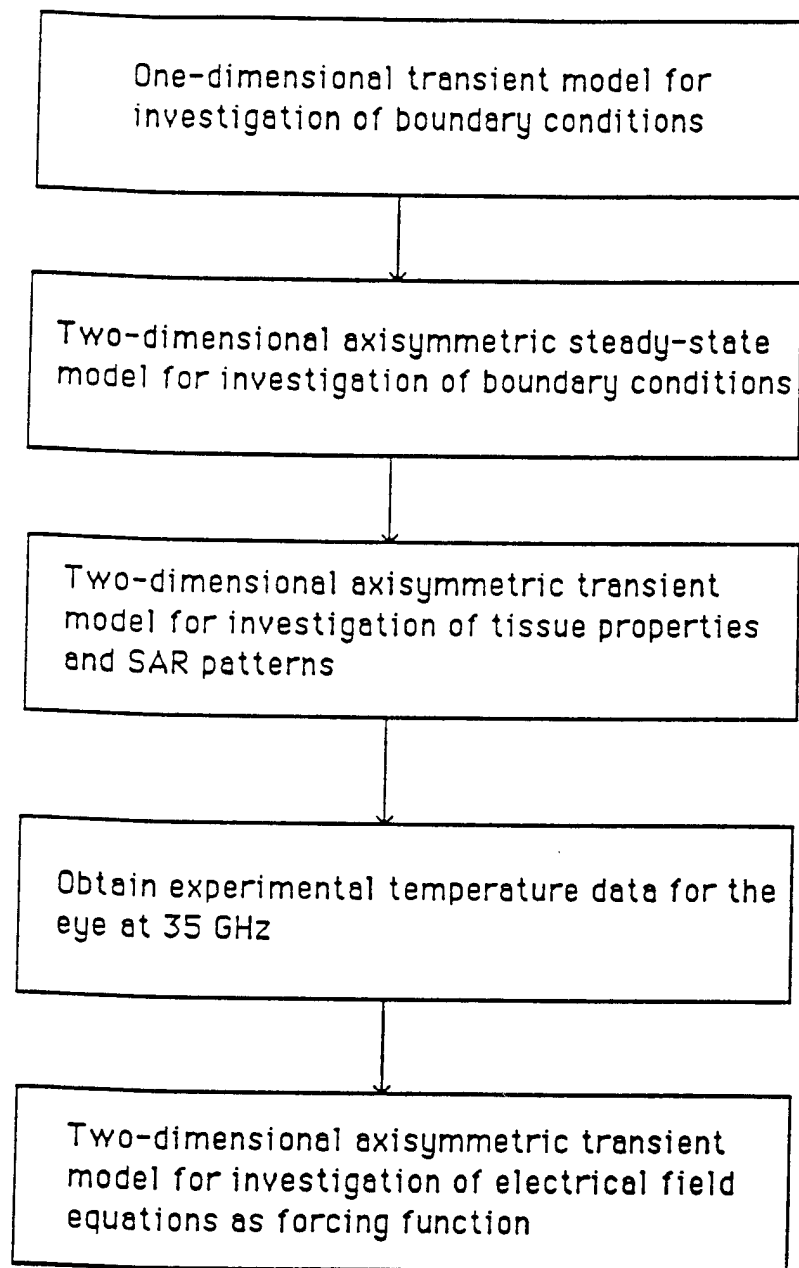


Figure 3-1. Steps in model development

be precisely known or may be a function of some unforeseen variable. Thus, ultimately the objective of a biological model is to reliably predict an outcome given a reasonable range of foreseeable input parameters. An example of an unforeseeable input parameter may be the health of the biological entity. Poor health compounded with the effects of a heat load as in this study may lead to unpredictable results. Thus, it is important to emphasize that the conditions and all parameters being used in the model are of laboratory origin which are ideal conditions. It is also important to note that a hypothesis made at the initial stages of the modeling process shown in Figure 3-1 may be wrong after further investigation, with the advent of new information, or with a newer model that emulates a particular phenomena better. It is essential to make an hypothesis and to test the hypothesis, then a decision can be made to take the hypothesis as fact, discard the hypothesis or continue investigating the hypothesis.

3.2.1 One-dimensional Model

First of all a simple one-dimensional model was used that included two Dirichlet boundary conditions. The grid is shown in Figure 3-2 and consisted of 2 quadratic elements per tissue layer. Each layer was assumed to have the thermal properties of water ($k = .0058 \text{ W/cm-C}$ and $\rho c = 3.23 \text{ J/cm}^3 \text{ -C}$) except for the lens and fat which have thermal properties of ($k = .0021 \text{ W/cm -C}$ and $\rho c = 4.217 \text{ J/cm}^3 \text{ -C}$). The model was executed for a insult scenario in which the surface of the eye at time zero experienced a scaled temperature rise of one. The entire eye before time zero was assumed to be at a uniform temperature of zero. The assumption of no temperature rise at the posterior region of the eye was confirmed by comparing results runs made

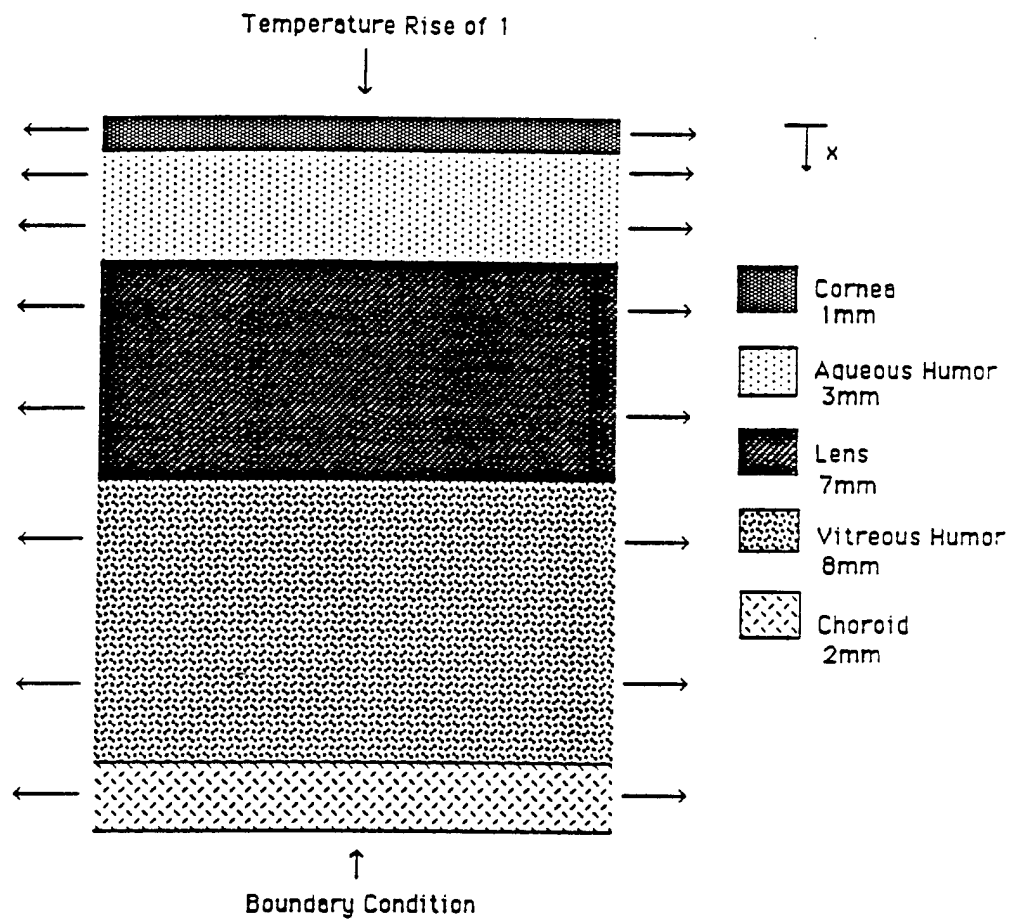


Figure 3-2a. Transient semiinfinite model of the eye.

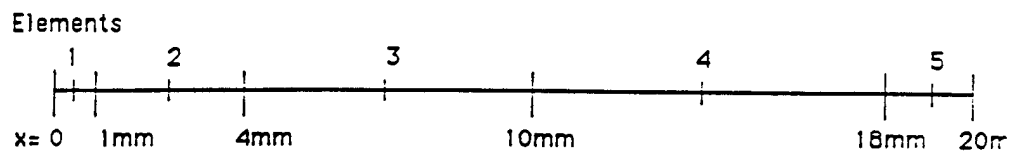


Figure 3-2b. One-dimensional finite element grid of eye used to investigate boundary conditions.

with no flow conditions at the posterior region behind the choroid and results from runs with a fat layer 10 mm thick posterior to the choroid region and results from runs with no temperature rise. A fat layer of 10 mm thick corresponds to the anatomy surrounding the eye. The temperature distribution of the one-dimensional no temperature rise at the back of the choroid model was within 10 percent of the values obtained for the one-dimensional model that included an extra layer of fat. Thus, the initial hypothesis that two factors: 1) the distance from the energy source to the choroid and, 2) the continual blood flow at constant temperature at the choroid contribute to there being no temperature rise in the choroidal layer is supported.

3.2.2 Two-dimensional Axisymmetric Steady-state Model

A two-dimensional finite element model was used to investigate the effects of perfusion on temperature distributions in the eye. The two-dimensional study was used to judge if there were any great effects due to increased perfusion. In other words, to test the feasibility of the hypothesis that blood perfusion effects the thermal contours within the eye. The two-dimensional axisymmetric model used represents the eye as a sphere, as shown in Figure 3-3. The code used quadratic elements with 43 elements representing the eye. The values for tissue properties that were used for this test run are given in Table 2-1. The perfusion coefficient, $\omega_b \rho_b c_b$, was varied from 0, to 0.05, 0.5 J/C-sec for the ciliary body. The calculated normal blood flow for the ciliary body assuming a normal blood flow of 2.7 cm³/min-ml of tissue for a total eye volume of 4.187 cm³ yields a perfusion coefficient of .012 J/C-sec for the ciliary body assuming 27% of the total blood flows in the ciliary

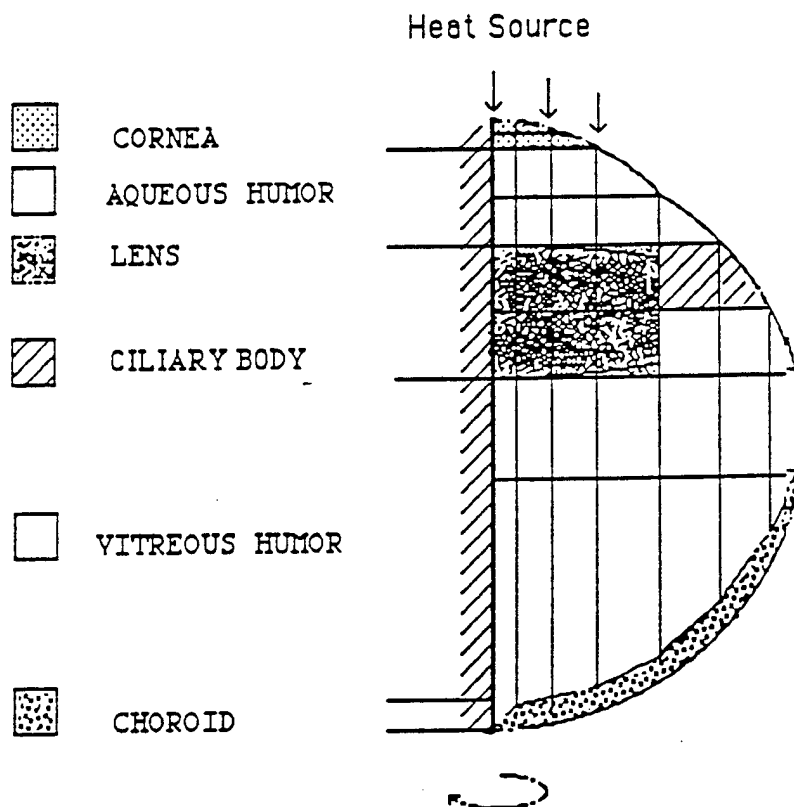


Figure 3-3. Two-dimensional steady-state axisymmetric model used to investigate boundary conditions.

body. Thus, the selected perfusion coefficient range from 0 to 4.167 times normal perfusion. The choroid in all test runs was assumed to receive 0.1 J/C-sec where as the normal value is .033 J/C-sec assuming the 72 % of the total blood flows in the choroid. This high value for the choroid was assumed because the elevated temperatures of the eye and surrounding tissue increase perfusion and in this test run the effects of heating and perfusion on the lens and cornea were the primary concern.

The model was executed for a insult scenario in which the surface of the cornea at time zero experienced a scaled temperature rise of one. The entire eye before time zero was assumed to be at a uniform temperature of zero. Along the line of symmetry and at rear of the eye below the choroidal region no flow conditions were specified. The assumption of no flow boundary conditions were made because fat is a good thermal insulator and the high perfusion rate in the choroid mimicked a no temperature rise conditions which was investigated by the one-dimensional study.

The temperature corresponding to the line of symmetry is plotted versus distance for the range of blood perfusion rates in Figure 3-4. This graph shows that the perfusion rate does have an effect on the temperature distribution within the eye. The graph also shows that the greatest temperature differential between the curves occurs at a region 8 to 10 mm from the apex of the cornea, corresponding to a position within the lens. At this distance the line of symmetry is most proximal to the ciliary body: thus, the blood perfusion within the ciliary body has the greatest effect. Figure 3-5 shows the temperature profiles radially across the lens with the varying perfusion rates. The temperature profiles vary in the radial direction along the center of the lens and beginning from the line of symmetry and extend through the ciliary body. As expected the temperatures decay as they

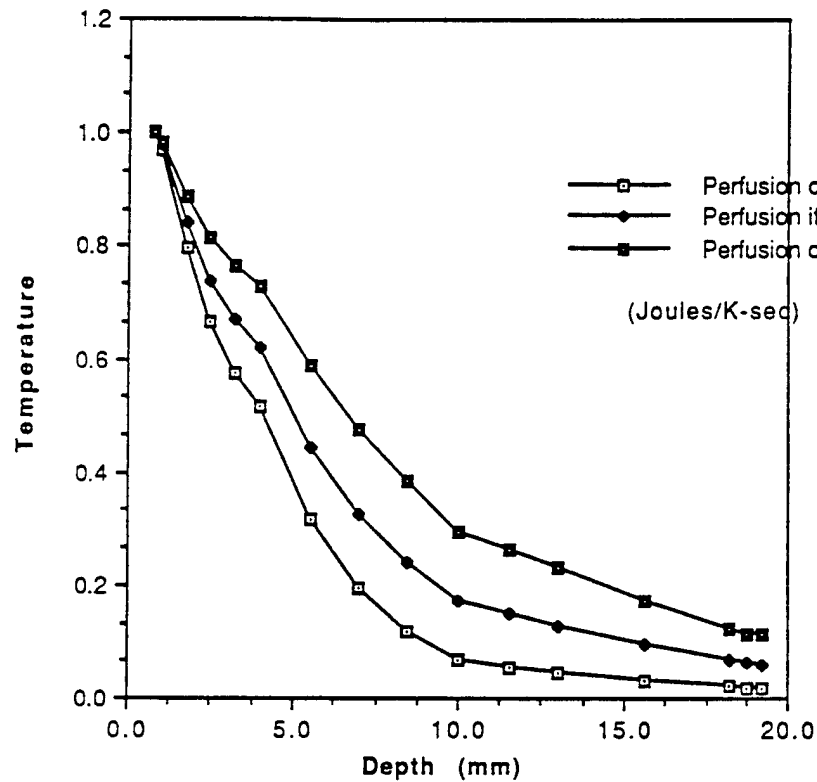


Figure 3-4. Steady-state temperatures for the axial line of symmetry in the eye for a range of blood perfusion rates with Dirichlet boundary conditions at the cornea.

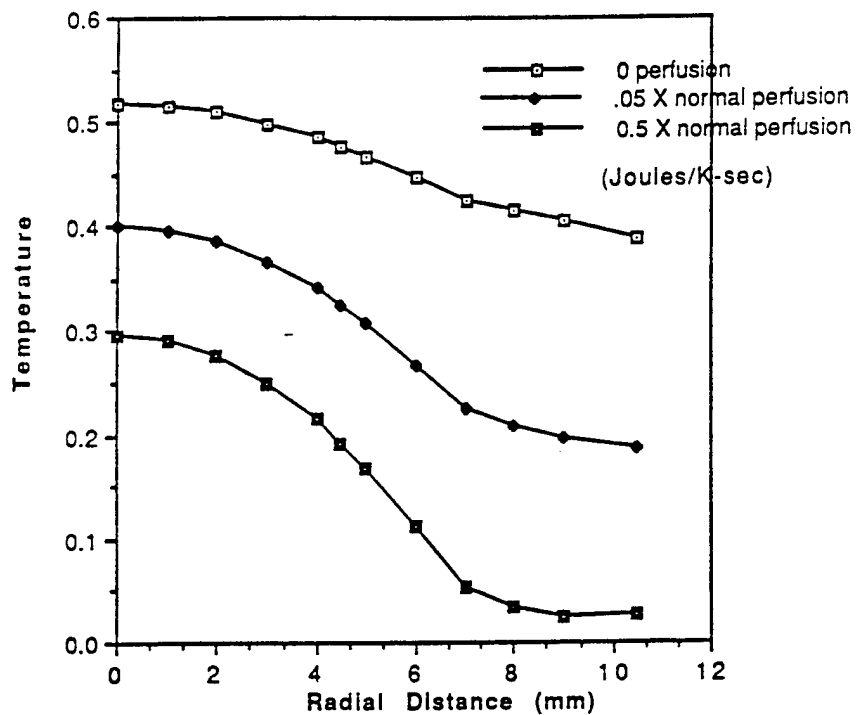


Figure 3-5. Steady-state temperature profiles radially through the lens at varying perfusion rates with Dirichlet boundary conditions at the Cornea.

approach the ciliary body. The maximum temperature difference due to the varying perfusion rates occurs at the interface between the lens and the ciliary body. The sharp decays in the temperatures in the radial direction are due to the perfusion in the ciliary body acting to shunt the heat away. Overall, the greatest temperature increases occur along the line of symmetry of the eye due to the ciliary body acting as a radial heat sink. This corresponds to the point at which most cataracts occur. This analysis shows that the perfusion rate within the ciliary body are important in determining the actual temperature profiles within the lens and cornea.

3.2.3 High Resolution Two-dimensional Axisymmetric Transient Model Using SAR Patterns as the Forcing Function

Next a higher resolution two-dimensional axisymmetric model based on a sagittal slice through the eye was used. Figure 3-6 shows the physical geometry and Figure 3-7 shows the corresponding finite element grid. The finite element grid consists of 121 quadratic triangles and rectangles and 367 nodes. The sagittal slice is rotated about the axis of the eye to create a symmetric body of revolution. The tissue structure consist of the cornea, aqueous humor, lens, vitreous humor, ciliary body, fat, sclera, and muscle. This model gives a reasonable representation of the interior geometry of the eye and the surrounding tissue. Equation (2-1) was solved using the finite element grid shown in Figure 3-7.

In this model blood perfusion rates are assumed to be constant with time. There is evidence that the blood perfusion in skin can increase by a factor of 30 or more with elevation in tissue temperatures [39]. It is reasonable to assume that blood perfusion rates in the eye are also temperature

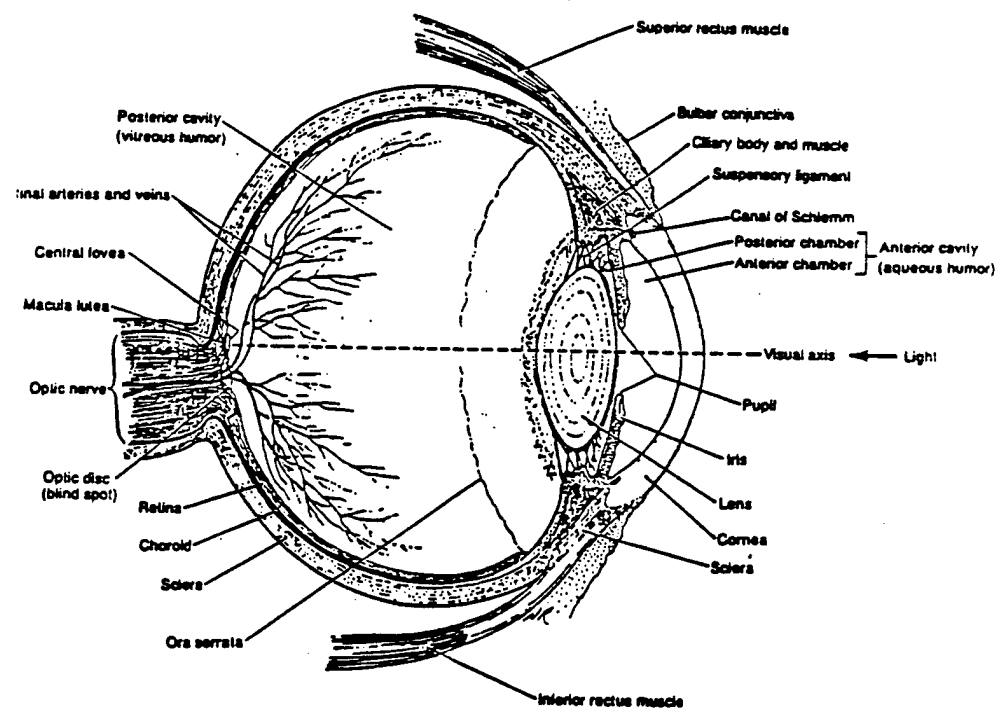


Figure 3-6. Physical model of the eye [28].

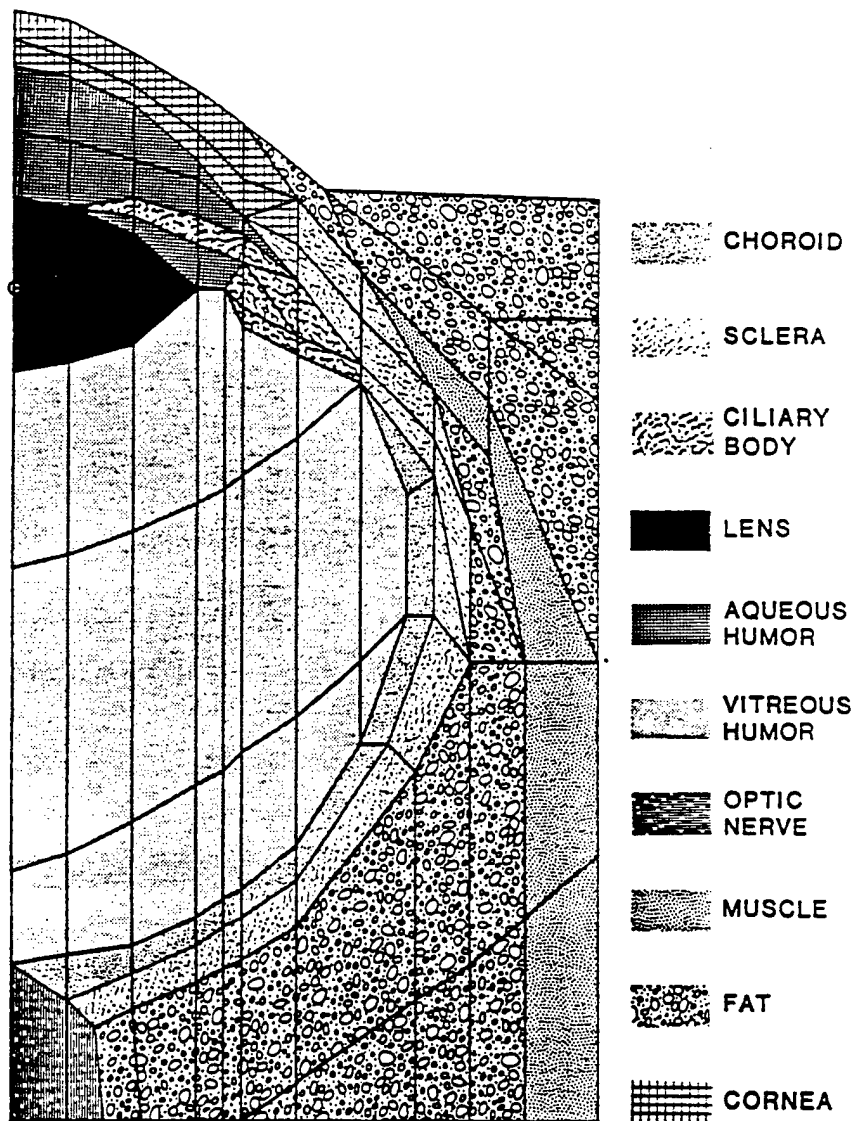


Figure 3-7. Finite element grid of the eye.

dependent; however, since there is no experimental data available to describe the temperature dependence, perfusion rates in this study were varied over an order of magnitude to demonstrate the significant effects that increased levels of perfusion can have in cooling the eye during hyperthermia.

The heat generation term is calculated from a linear function derived from experimental SAR values (2.45 GHz) for the eye and head of a monkey shown in Figure 3-8 [19]. Although the experimental data indicates that the microwave energy decreases exponentially with depth through the eye and head. The data in the eye alone (0 to 22mm) was approximated very well by the linear segment in Figure 3-8. A peak value of 0.38 W/kg per mW/cm² was employed at the apex of the cornea and decreased linearly to a value of 0.21 W/kg per mW/cm² at the back of the eye. The linear function was multiplied by the applied power density of 200 mW/cm² and the density of the tissue to arrive at a heat generation term in W/cm³. The linear heat distribution was applied throughout the eye and surrounding tissues. Although this type of one dimensional electrical heating was obtained from experimental data taken along the center of the eye [10], there is little reason to believe that the heating patterns would develop uniformly in for the system geometry. A more sophisticated model would include solving the electrical field equations for the system geometry and coupling these with the thermal equations.

The values of the thermal properties used in equation (2-1) for each of the tissue types are given in Table 2-1. The highly myelinated optic nerve was assumed to be similar to brain white matter. One should note that the thermal conductivity of the lens is approximately one third of that of water and the other eye tissues. This model gives a very realistic representation of the interior geometry of the eye and the surrounding tissue.

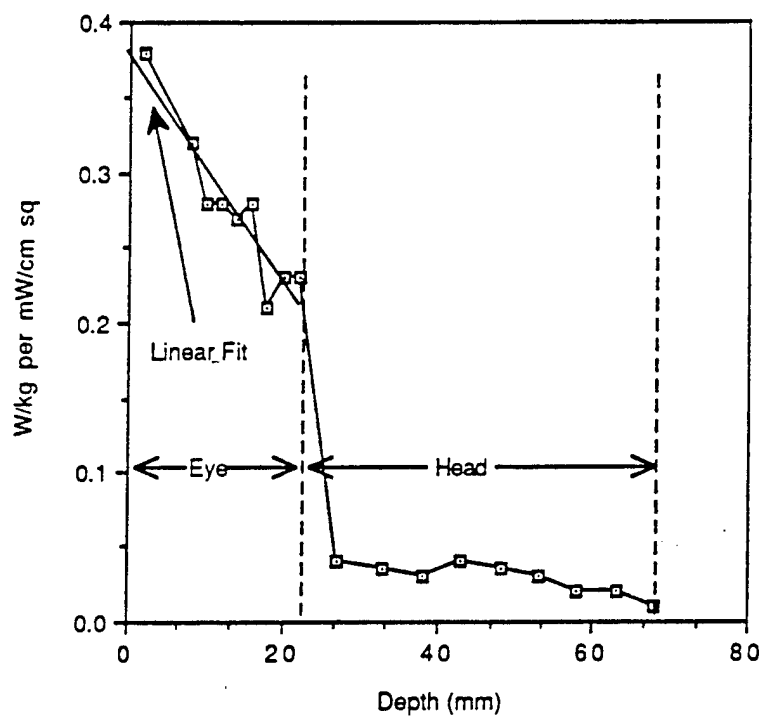


Figure 3-8 Measured heat generation term as a function of depth for the eye and head of monkey exposed to 2.45 GHz

Schwartz and Feller [72] found that the normal temperature of the eye varied from 32 C at the surface to 37 C at the retina. Therefore, in this model we have assumed a uniform initial temperature of 34 C in the eye. This assumption is reasonable since long term temperature increases are of interest which develop in the eye as opposed to the initial transient behavior. The arterial temperature is also taken to be 34 C because it is reasonable to assume that the core temperature will have cooled and equilibrated to some degree with the tissue temperature in the eye. A no flow or insulated boundary condition is applied on both the left and right lateral boundaries. The left lateral boundary of the grid is an axis of thermal and geometric symmetry, and the assumption that the eye is encased in a layer of fat which has a very low conductivity is made for the right lateral boundary. The rear surface of the eye is held at 34 C since a layer of fat was added behind the choroidal layer. The assumption is that at further distances from the heat source the tissue will have a tendency to maintain a temperature consistent with the core temperature. The front surface of the eye and surrounding tissue which is exposed to free convection to still air at 25 C has a convective resistance at the surface of $h=0.001 \text{ W/cm}^2\text{-C}$ [34]. The transient temperature fields were solved using a backward difference time stepping method with a time step of 20 seconds, and microwave heating was simulated for 2400 seconds in all cases.

3.2.3.1 Two-dimensional Axisymmetric SAR Forcing Function Model Results

Several simulation runs were made to show the effect of accurate thermal property values for various tissue types and of perfusion on the thermal fields. The numerical results are presented in terms of temperature

contours and thermal histories at a point in the lens since in all cases the maximum temperature occurs in the lens. The first test case is presented in order to compare the effects of having thermal properties obtained from the literature for the various tissues within the eye as opposed to simply applying the properties of water uniformly throughout the eye. The correct thermal properties of fat and muscle were used in the surrounding tissues and the previous linear heat generation for the entire grid was assumed. Perfusion was assumed to be at normal values for the ciliary body, choroid, fat and muscle. Figure 3-9 shows the thermal contours corresponding to using the thermal properties of distilled water throughout the eye. Figure 3-10 is the base case and includes all known thermal properties and the normal perfusion rates given in Table 2-1. The thermal fields are virtually identical for both cases except the area which is near the lens. The thermal properties in the various tissues of the eyes are not well known, and in fact, in many cases we assume properties similar to water. This is a reasonable starting assumption except in tissues, such as the lens which has thermal properties similar to fat and acts like a localized insulating tissue. In these areas the correct thermal properties can play significant role in accurately predicting thermal fields, even if the total volume of that tissue is quite small.

Next, the effects of perfusion in the eye were considered. Figure 3-11 presents the temperature contours for the linear SAR heating, but with no perfusion either in the eye or in the surrounding tissues. This data shows that if perfusion is ignored, then extremely high temperatures are predicted within the eye with a maximum temperature of 54.5 C occurring in the lens. By comparing this data to Figure 3-10 which assumes a normal perfusion rate in the eye and surrounding tissue, we find that the maximum temperature of 46.5 C occurs in the lens. There is approximately an 8 C increase in predicted

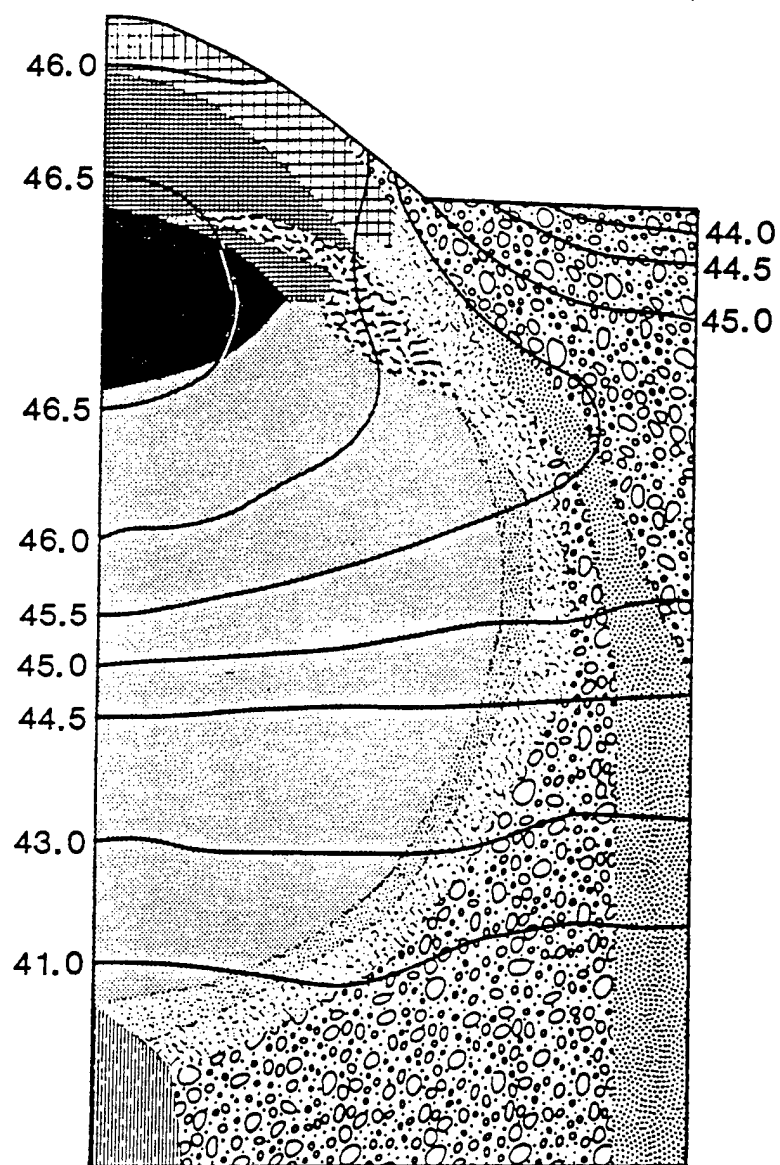


Figure 3-9. Computed temperature contours for the eye exposed to 2.45 GHz (power density of 200 mW/cm^2) for 2400 sec using the thermal properties of distilled water for all tissues.

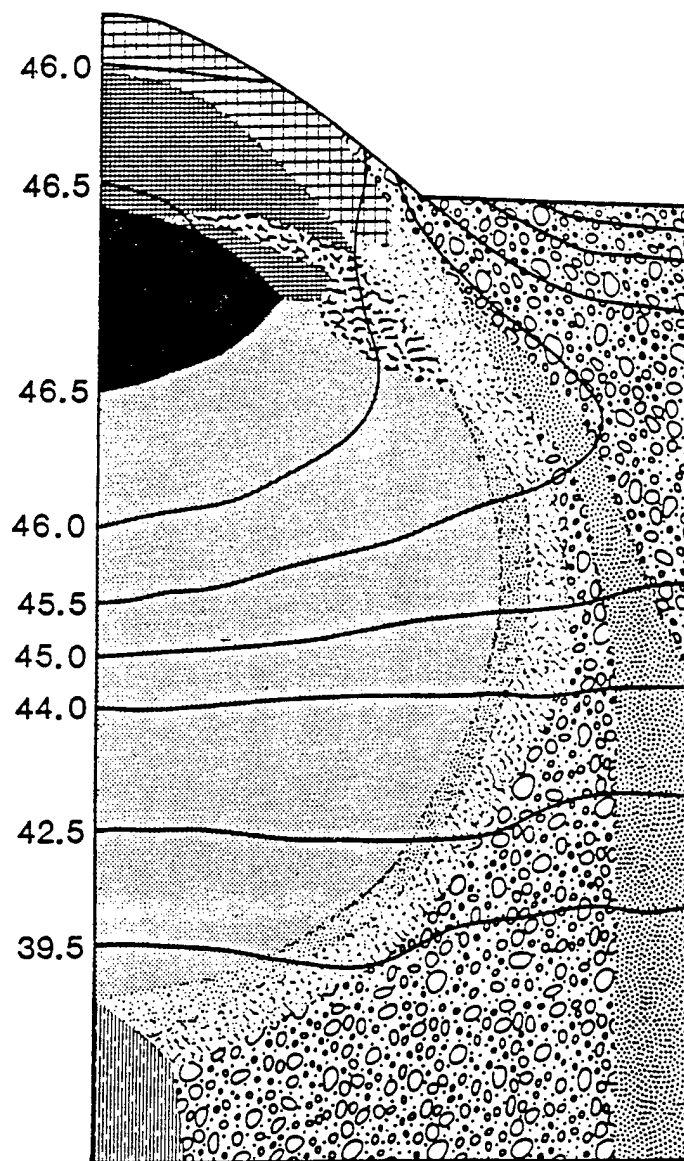


Figure 3-10. Computed temperature contours for the eye exposed to 2.45 GHz (power density of 200 mW/cm^2) for 2400 sec using known thermal properties and normal perfusion levels.

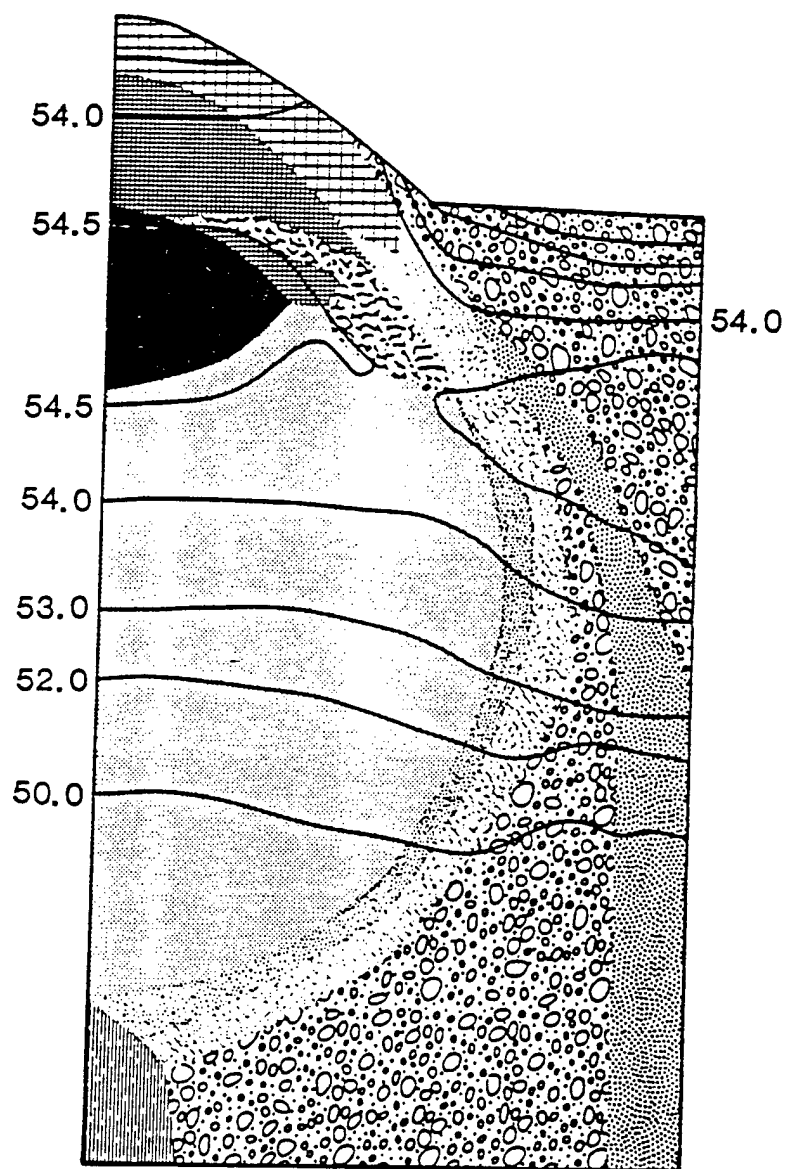


Figure 3-11. Computed temperature contours for the eye exposed to 2.45 GHz (power density of 200 mW/cm²) for 2400 sec assuming no perfusion in the eye and surrounding tissues.

temperatures when perfusion is absent from the model, and without perfusion the temperature contours tend to be quite linear because the heating function is linear. Perfusion acts to bend the temperature contours so that they conform more to the geometry of the perfused tissue, as in Figure 3-11. Figure 3-12 shows thermal contours calculated when perfusion is ten times normal. In this case the perfusion dominates the heat transfer and the thermal contours conform very well to the geometry of the perfused layer. Again, the maximum temperature occurs in the lens; however, this temperature is only 37 C which represents a 3 C increase over the initial value. The temperatures in the eye are approximately 9 C cooler with this higher perfusion level. These figures illustrate the significant role that blood perfusion plays in determining the thermal fields which develop in the eye during a thermal insult. This effect is particularly significant if perfusion increases with temperature.

Figure 3-12 shows the thermal contours for the same thermal insult, but with normal perfusion only occurring in the ciliary and choroid layers, with no perfusion in the surrounding muscle or fat layers. The temperatures presented in this case are significantly higher and the thermal contours tend to be more linear than in the base case corresponding to the dominance of the linear heating term as perfusion decreases. Finally, Figure 3-13 shows the temperature contours for a case which corresponds to perfusion only in the ciliary body and choroid and with no perfusion and no heat generation in the fat and muscle layers. This case is presented because it correlates well to previous data [34] and would correspond to solving an accurate thermal model in the eye assuming the surrounding tissues act as a quasi-insulating material. Again, the maximum temperatures occur in the lens; however, the thermal fields are quite different from the base case. The heating is much

lower, which is to be expected, since the total volume of heat generation has been decreased, and the thermal contours conform much better to the geometry of the eyeball. Again, this is to be expected because both the perfusion and the heating function occur only in the eyeball and not in the surrounding tissues. The contours in Figure 3-13 also illustrate that, with the assumption of no perfusion and no heat generation in the muscle and fat, these two surrounding tissues act as a quasi-insulating material with fairly uniform thermal gradient. However, in comparing Figures 3-10 and 3-13 the temperatures and the geometry of the thermal contours are quite different. This illustrates the significant effect which thermal properties, the geometry, perfusion and heat sources have in both the surrounding tissue and in the eye itself.

One can conclude from this data that if accurate thermal fields are required, it is necessary to use a very accurate numerical model which accurately incorporates geometry, material properties, perfusion rates and heat generation terms. Also, one can conclude that there are several mechanisms within the eye which tend to localize the peak heating in the lens. Convection to the ambient temperature allows heat to escape in the regions closest to the frontal surface of the eye. Blood perfusion acts to cool the eye. Since the choroid is a highly perfused sheath that covers the posterior portion of the eye and the perfused ciliary body circumscribes the lens, the temperatures tend to peak along the axis of the eye. Also, since the thermal conductivity of the lens is low compared to other tissues, it tends to act as a local non-conducting body with internal heat generation. All of these phenomenon act to concentrate the heating near the lens. The cooling is more pronounced as the perfusion rates increase.

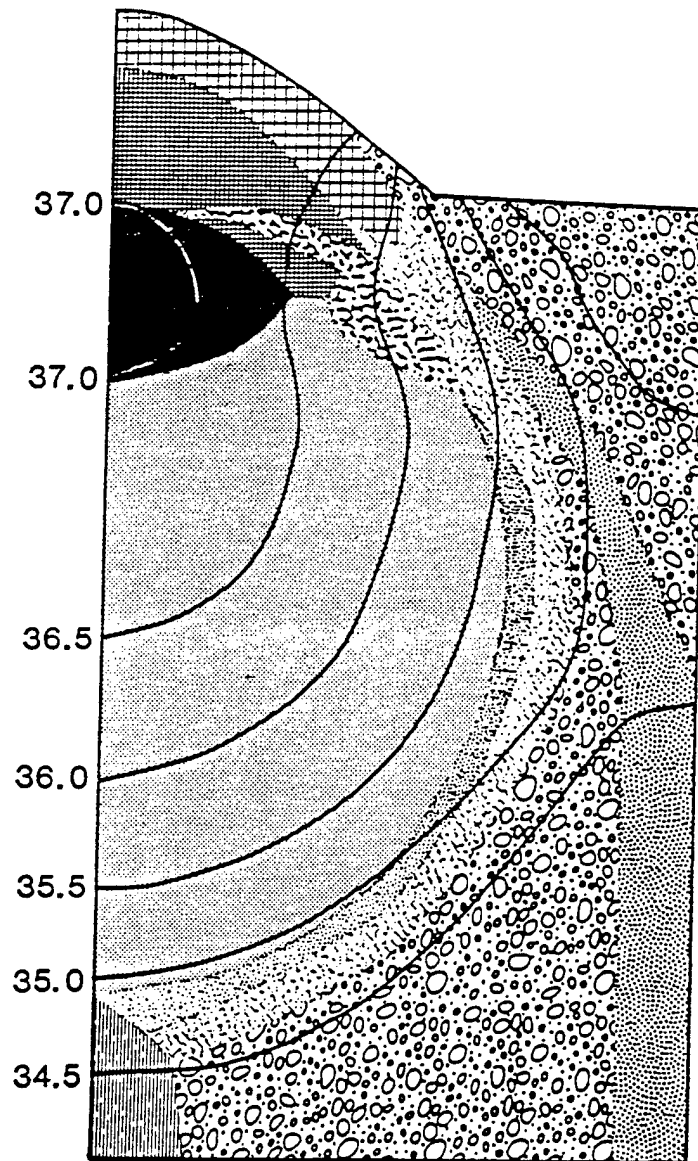


Figure 3-12. Computed temperature contours for the eye exposed to 2.45 GHz (power density of 200 mW/cm^2) for 2400 sec assuming perfusion levels 10 times normal.

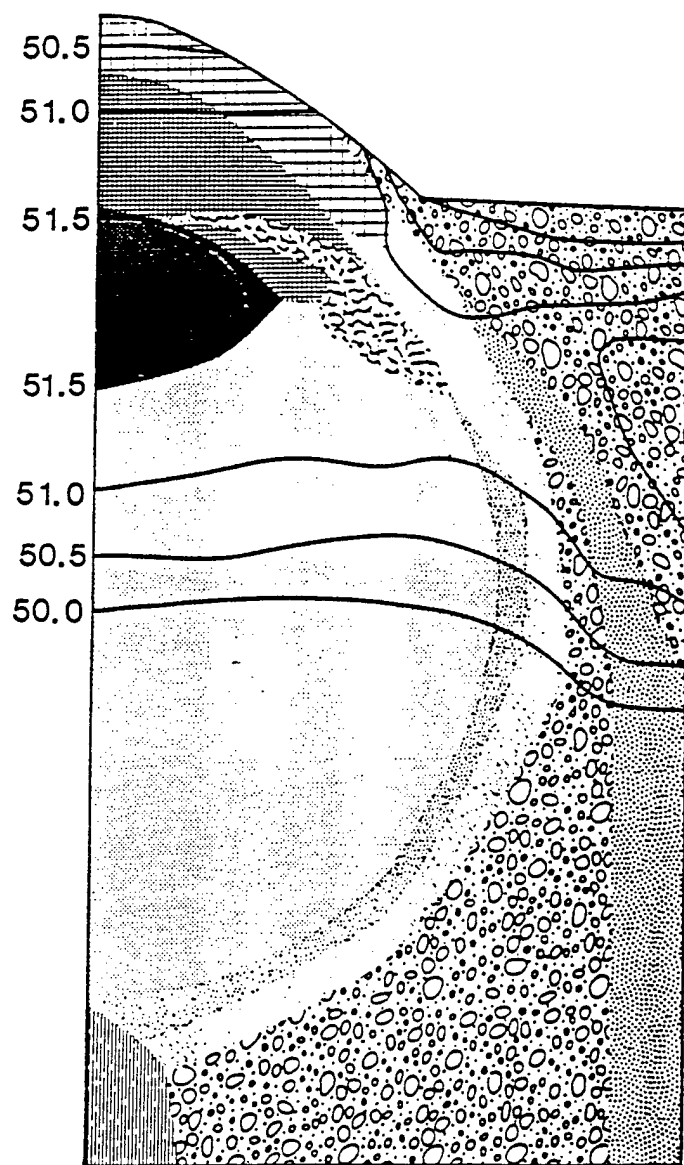


Figure 3-13. Computed temperature contours for the eye exposed to 2.45 GHz (power density of 200 mW/cm^2) for 2400 sec assuming normal perfusion rates in the ciliary body and choroid and no perfusion in the muscle and fat.

Both with no perfusion and with normal perfusion the contour lines tend to be linear in the posterior portion of the eye. This indicates that the thermal fields are dominated by the linear heat source. However, in the high perfusion case, the contours tend to conform more to the radial geometry of the perfused tissue. Figure 3-14 shows temperature verses time for the node within the lens which is high-lighted on the finite element grid. This node corresponds closely to the maximum temperature which occurs in the eye. These temperature histories are presented for this node for 0.5, 1.0, and 10 times the normal perfusion rate. In all cases the temperatures increases as a function of time. However, the higher perfusion rates act to limit the increase. In fact, when perfusion is 10 times normal, perfusion dominates the thermal process and steady state occurs very rapidly following the initiation of heating.

Overall, an axisymmetric transient finite element model of a thermal insult protocol at 200 mW/cm^2 (peak SAR of $0.38 \text{ W/kg per mW/cm}^2$) was simulated for 2400 sec. The model accurately incorporates the geometry of the eye as well as values of thermal properties that are known. The model includes perfusion and a linear heat source both in the eye and in the surrounding muscle and fat tissues. These results indicate that an accurate representation of both the internal geometry and thermal properties is required if these properties differ significantly from the values for water. It also illustrates that heat transfer, perfusion and heat generation in the surrounding muscle and fat bed can be significant and should not be ignored. The role of perfusion is crucial in accurately determining thermal fields within the eye, and it is particularly significant if perfusion levels increase with elevated temperatures.

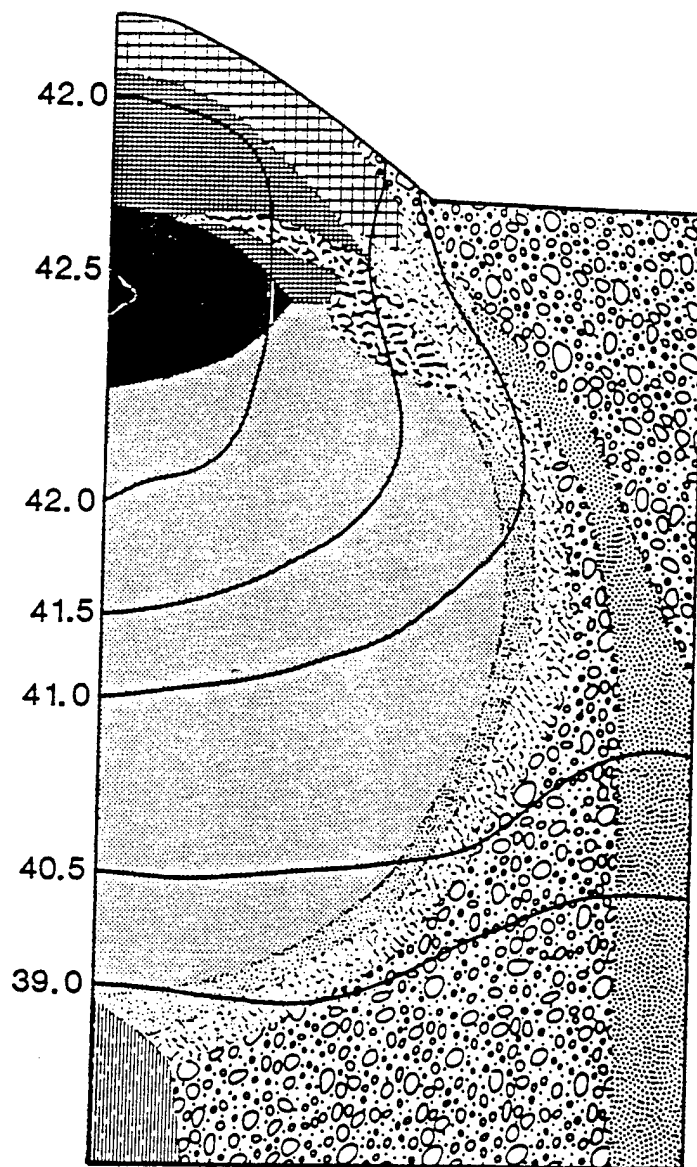


Figure 3-14. Computed temperature contours for the eye exposed to 2.45 GHz (power density of 200 mW/cm^2) for 2400 sec assuming normal perfusion in the ciliary body and choroid and with perfusion and no heat generation in the surrounding fat and muscle layers.

In all cases the maximum heating occurred in the lens, due in part to the local insulating effect caused by low thermal conductivity of the lens and by perfusion in surrounding tissue layers. In this study a linear heat source based on measured, one-dimensional SAR patterns was used. This approach does not accurately represent the actual heat generation which would be induced by microwaves. A significant improvement in the model would be accomplished by coupling the electrical field equations with the thermal equations. Next, following the flow chart in Figure 3-1, experimental data obtained from exposure of a cat eye to 35 GHz at 125 mW/cm², 75 mW/cm² and 10 mW/cm² will be investigated and new information will be incorporated into a transient two-dimensional axisymmetric with electromagnetic volumetric power absorption as the heat source term.

CHAPTER 4

SOFTWARE DEVELOPMENT FOR ENDOTHELIAL CELL ANALYSIS

The inherent morphological characteristics of the endothelial cell images make them very difficult to determine the cell boundaries automatically by computer. These include a strong background gray scale gradient, low contrast boundaries, extraneous non-boundary structure, and image blurring due to eye movement.

After exploring several candidate image processing techniques, the one described below gave the best results when applied to a typical image of corneal endothelial cells. To test the accuracy of this automated technique, a hand-traced technique was also developed and both techniques were applied for comparing several images.

4.1 AUTOMATED CELL COUNT AND AREA MEASUREMENT

Images of the corneal endothelial cells were obtained on a slit lamp microscope, as described in the previous chapter. The images were evaluated off line and the ones with the best resolution and the highest contrast were stored in the computer for analysis.

Images on the MicroVax are analyzed with an algorithm for automated cell count and area measurement. A primary objective of the analysis

protocol is identification of the boundaries of the individual cells in a designed portion of field of view.

The first concern is the detection of intensity changes. The gray level differentiation is not very clear in the image, and the intensity changes occur at different scales in the image due to the illumination differences throughout the whole image. Figure 4.1.1 shows an example of a typical digitized image of the corneal endothelium obtained from the slit lamp.

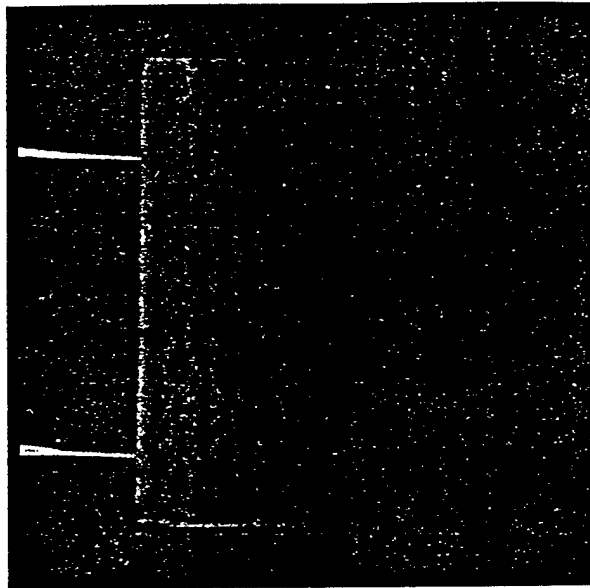


Figure 4.1.1. Original Image obtained from the slit lamp.

Since the image is obtained from a slit lamp and the light variation is so intense, there is only a small portion of the picture that contains the cellular information that is relevant to the analysis. The operator must choose interactively a window of the total image area where the cells are differentiated. Also, inside the portion of the image that contains the cells, due to the background light intensity shading, not all sections of the cell area

have a common appearance. By identifying only a subsection of the image, the noise contained in the rest of the picture will not affect the analysis. Choosing the window of analysis is performed interactively with a mouse on the MicroVax by overlaying a frame onto the viewing monitor. This area is stored into memory for analysis, and the original image is kept for later reference.

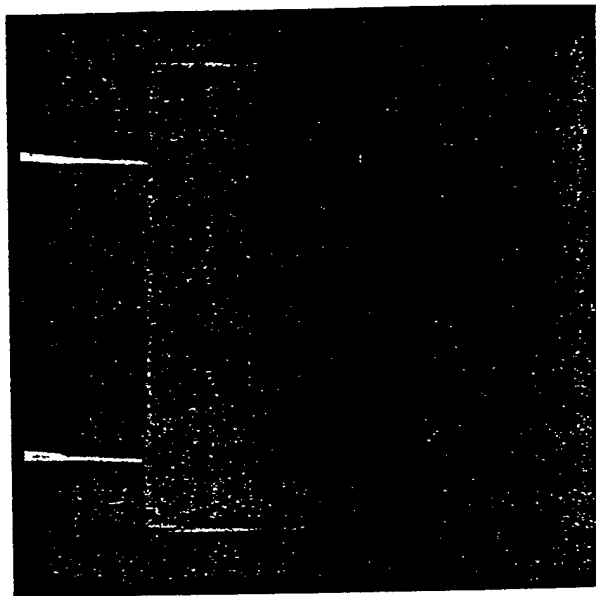


Figure 4.1.2. Original image with chosen window drawn.

The windowing algorithm is illustrated in the flowchart on Figure 3.

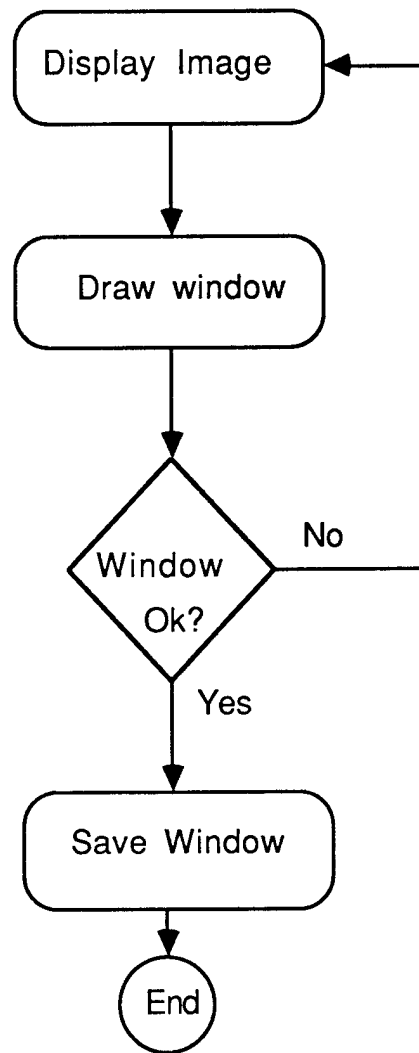
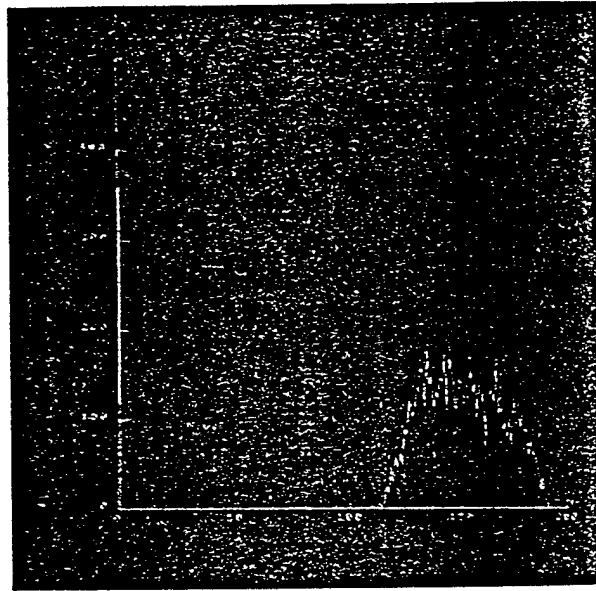


Figure 4.1.3. Windowing algorithm flowchart

To reduce the gray level gradient across the picture a linear operator is applied to the original image to equalize the gray level biasing in the image. The gray levels vary linearly from column to column: they decrease in value (image is darker) from the left side of the image to the right side, but it remains relatively constant within a given column. By taking the average of the 10th column of the image and the average of one of the last columns and subtracting these averages, the gray level variation is obtained. By taking the

pixel value and subtracting the average obtained before and subtracting from it the pixel column number multiplied by four, the gray levels becomes more uniform through the whole image. Figure 4.1.4a shows the histogram of the original image and Figure 4b show the histogram of the processed image.



4.1.4a. Gray level histogram for the window of the original image.

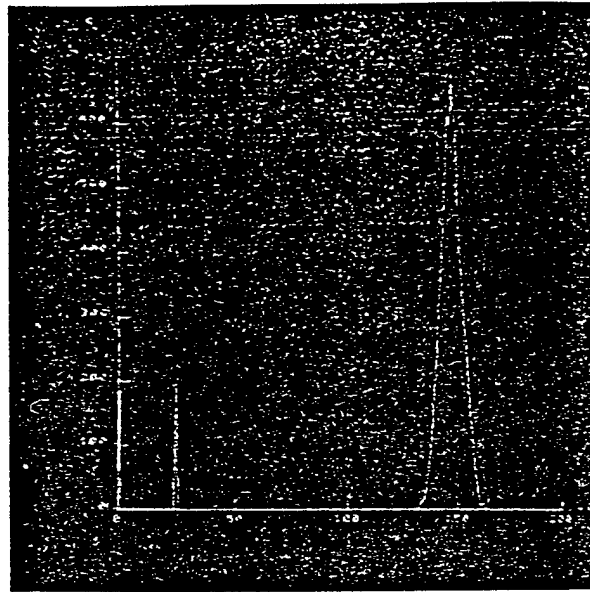


Figure 4.1.4b. Gray level histogram of equalized image.

After gray level modification, image is analyzed to count the one number of cells located within the window, their spatial distribution, and individual areas and morphology. To the naked eye, the cell boundaries look slightly darker than the centers, but the actual difference is not very big because gray level variations throughout the image are quite small due to the low contrast. The differential between boundary and interior may be less than the magnitude of local background shading. Fig. 4.1.4b shows that the gray levels do not vary much throughout the image. Another common feature in these images is that the boundaries may often appear to be quite broad. Due to these restrictions it is generally not possible to distinguish the boundaries by simple thresholding schemes. The first step is to remove the granularity of the image by applying a median filter of size 3X3 [51,56], which operates as a low-pass filter but does not blur edges as a regular low-pass filter would. Figure 4.1.5a shows the image after it has been equalized and Figure 4.1.5b shows the same image after the application of the 3X3 median filter.

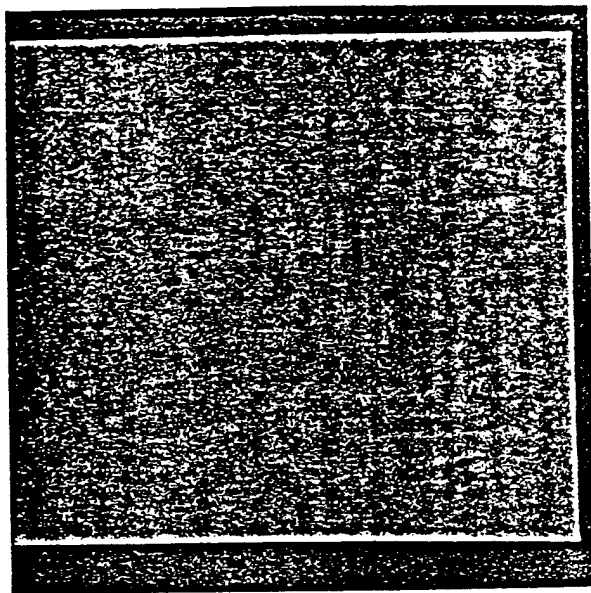


Figure 4.1.5a. Equalized image

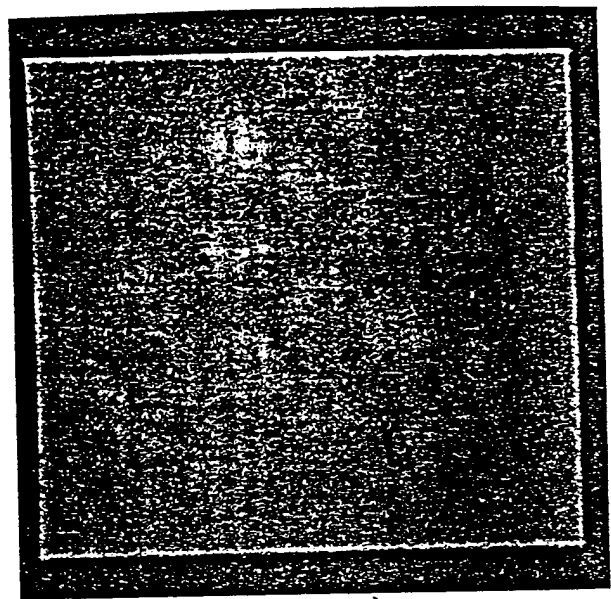


Fig. 4.1.5b. Median-filtered image.

In order to detect intensity changes associated with a cell boundary a filter with the following features is necessary. First, it should be a differential operator, taking either a first or second spatial derivative of the image; second, it must be capable of being tuned to act at any desired scale, so that large filters can be used to detect blurry shadow edges and small ones to detect sharply focused fine detail in the image [56].

This operator adopted is a Gaussian filter, with a shape resembling a circularly symmetric Mexican hat whose distribution in two dimensions may be expressed in terms of the radial distance from the origin as:

$$g_s(x,y) = \frac{1}{(2\pi s^2)^{1/2}} \exp\left\{-\frac{(x^2+y^2)}{2s^2}\right\} \quad (1)$$

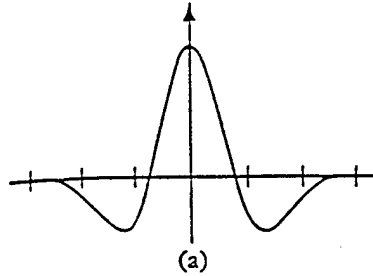


Fig. 4.1.6 Gaussian filter.

The Gaussian filter blurs the image, wiping out all structures at scales much smaller than the space constant of the Gaussian. In this case, the s was chosen to be 1.5, and the Gaussian is a 3X3 template because the objects to be detected, i.e., the cells, are very small (approximately 15 pixels in diameter). s has to be small enough so it will not remove the cell boundaries. The Gaussian distribution has the characteristic of being smooth and localized in both the spatial and frequency domains, so if the blurring is as smooth as possible, it is least likely to introduce any changes that were not present in the original image. The image is processed by convoluting $g(x,y)$ with the original image, is then convoluted with the Laplacian template:

$$\begin{bmatrix} 1 & 0 & 1 \\ 1 & -4 & 1 \\ 1 & 0 & 1 \end{bmatrix}$$

The numerical values in the Laplacian of Gaussian (LOG) filtered image are both positive and negative. It is rendered binary by setting the positive values white and negative values to black. In this image the boundaries should be well differentiated with not much noise. However, the weak features of the original images compromise the effectiveness of the LOG filter to give a binary image with all the boundary information contained in the original image. The gray level variation throughout the image does not exceed 50, and all the boundaries are not well differentiated, so the LOG image cannot accurately find all the edges. But it does give the center of each cell, since this part is lighter than the boundaries and adjacent regions. The LOG image is next used to obtain a binary image. First, to obtain 8 bits of gray scale, the image is scaled between 0 and 255. Plotting the histogram of this new scaled LOG image the upper and lower thresholds are set to reduce the noise in the picture, since all the pixels with values above 50 are obviously noise because they correspond to a very small percentage of the gray levels of the image so they cannot contain any valuable information (see Figure 4.1.7). Usually, there is a major peak in the histogram and then little bumps that, for reasons explained before, can be assumed as noise to be removed.

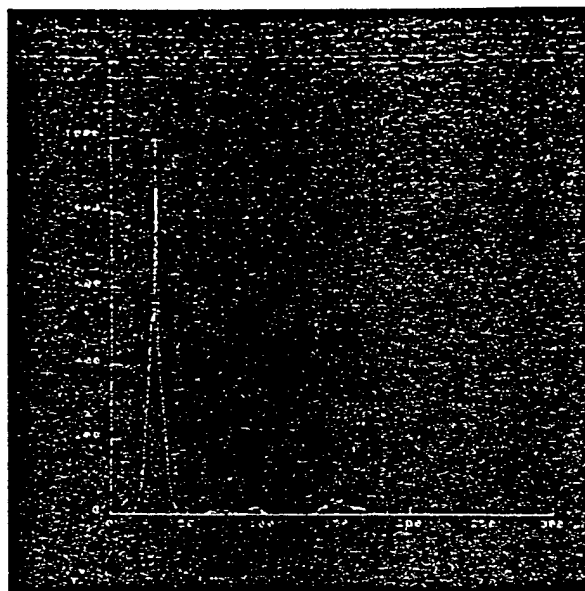


Figure 4.1.7. Histogram of the gray levels to be thresholded.

Thresholds are defined interactively by the user at the left and right sides of the major peak. The histogram of the new image is plotted, and by examining it a new threshold is calculated to obtain a binary image. After this last thresholding is applied, the resulting image will have all the center of the cells displayed white and the rest of the image displayed black. Figure 8 shows the histogram of the semi-thresholded image where only the noise is removed but the image still has several gray levels. The user enters the gray level value to threshold the binary image. If the resulting binary image is not satisfactory, the user can choose another threshold until an appropriate one is identified. Figure 4.1.9a-d show the different stages that the image goes through in transforming into a binary image. Figure 4.1.10 shows the flowchart of the algorithm implemented to obtain the binary image of cell centers.

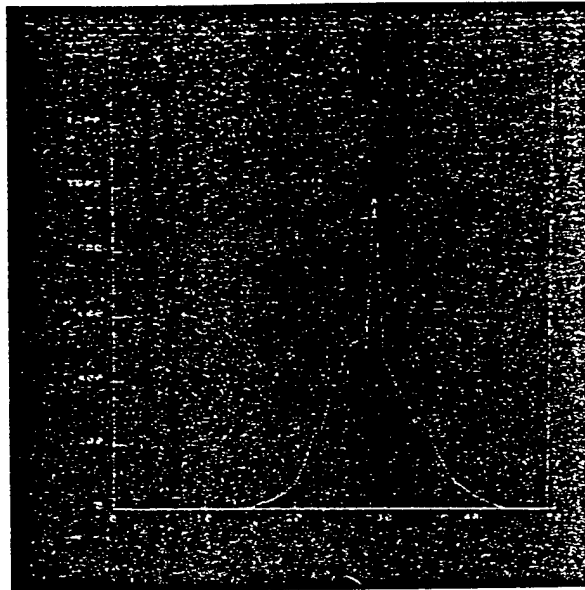


Figure 4.1.8. Simple threshold to obtain binary image.

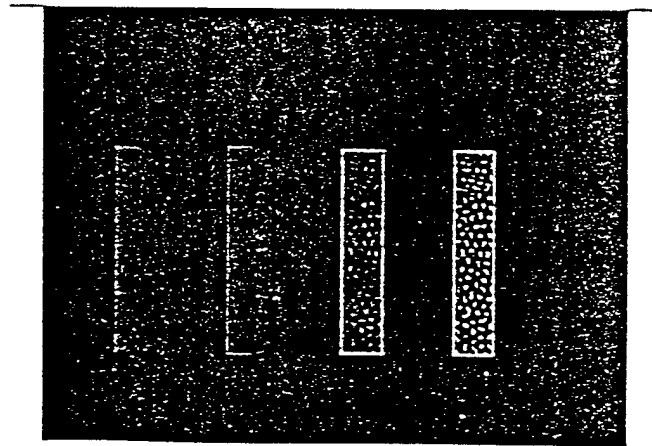
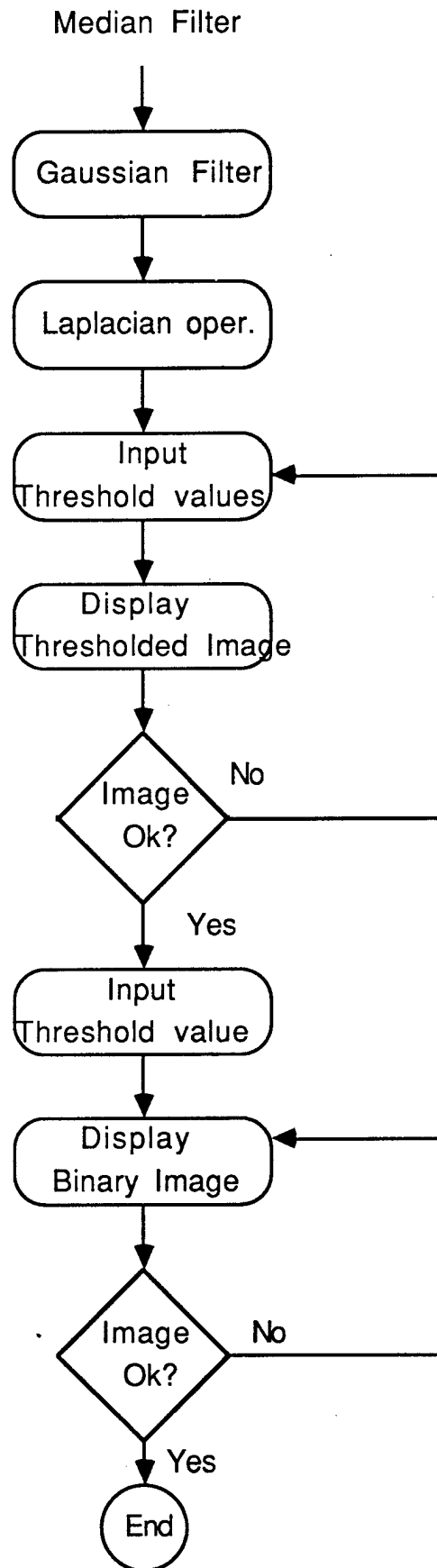
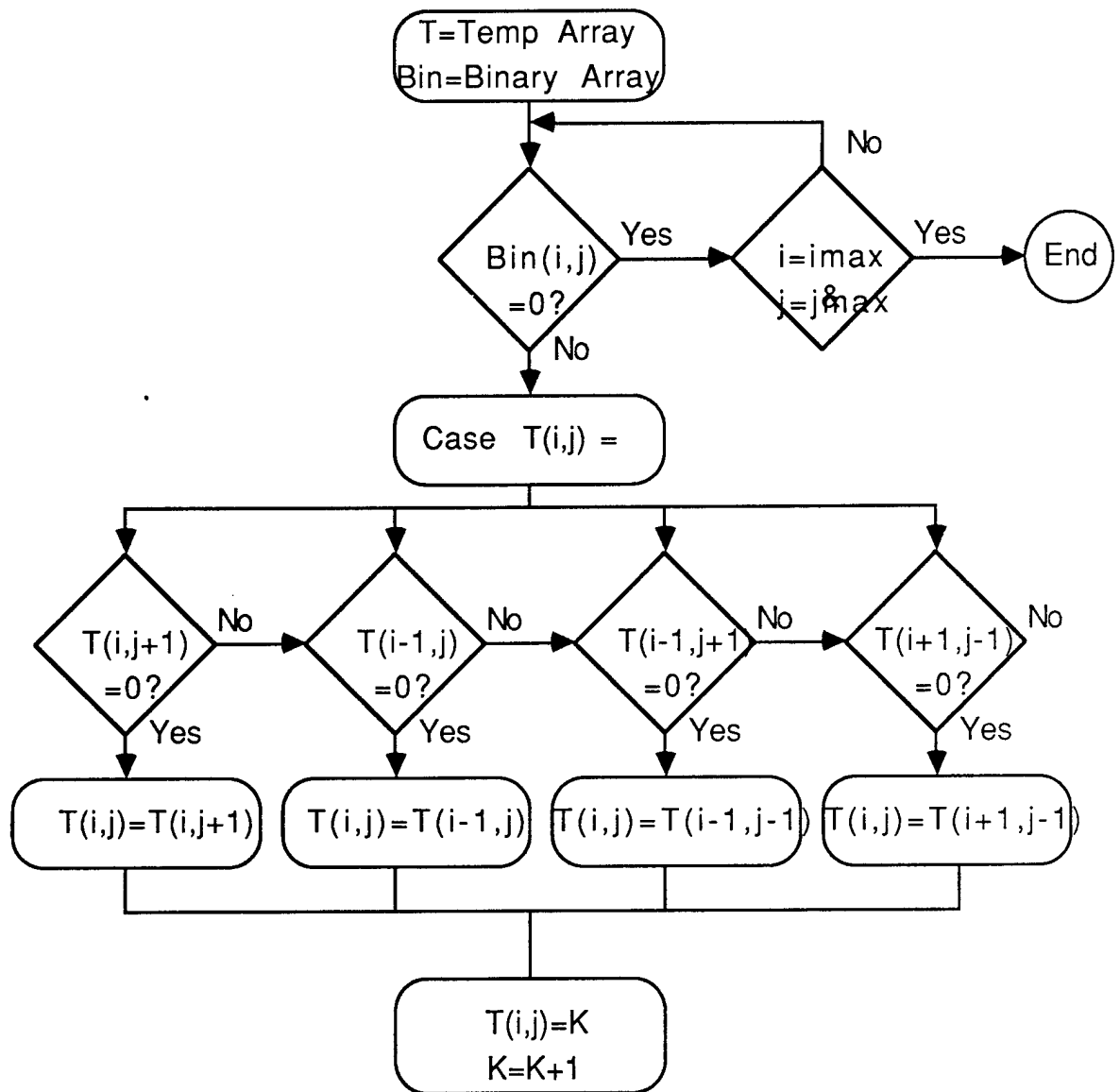


Figure 4.1.9a Original image, 4.1.9b Gray-leveled image,
4.1.9c Adaptive Thresholding Image, 4.1.9d Binary Image.





This image is going to be useful in obtaining the edges of the cells from their centers. In this case, the "colors" are numbers, from 0 to N, where N will be the number of cells contained in the image.

While the blob coloring algorithm was counting the blobs, it was also counting how many pixels formed each blob. This was done in order to find the area, in pixels, of each cell. The output of this procedure are the array $\text{Count}(i,j)$ which contains number of pixels in the center of each cell and the image $\text{Temp}(i,j)$ which contains the colored (numbered) centers of the cells.

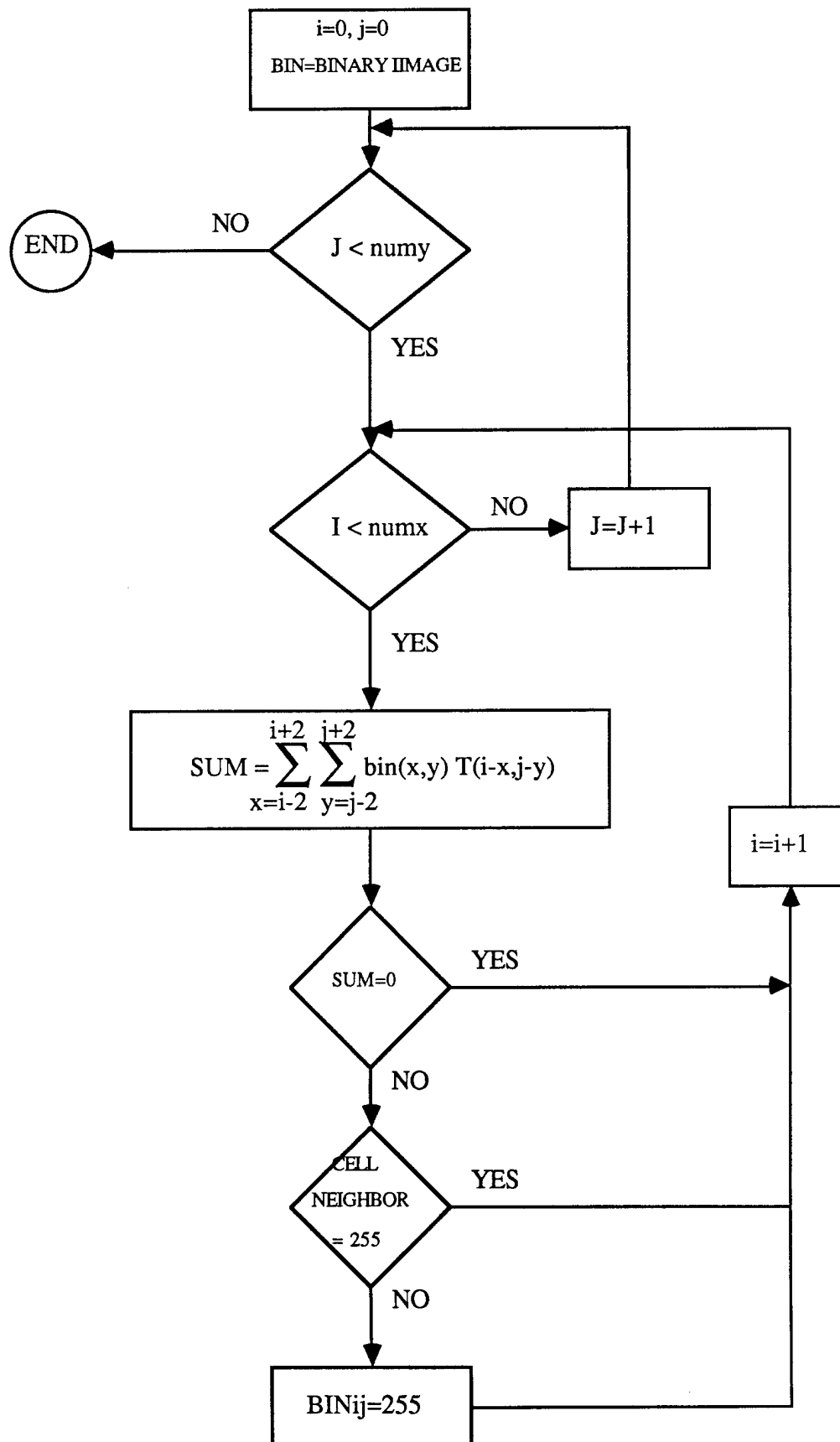
A region growing algorithm is applied to calculate the area of each cell [8]. This algorithm dilates the objects inside an image preserving their shapes. The dilation operation is defined as follows: A template T , which in this case is a 5X5 template in the shape of a cross (See Figure 4.1.12,) interacts with the binary image BIN and transforms it into another form. If the template T has at least one common element with the binary image BIN , then the point in question becomes part of the object, which in this case represent the center of the cells. It is called the "Rolling Ball" algorithm because the template resembles a little ball rolling along the boundaries of the objects and dilating them when appropriate.

	-2	-1	0	1	2
2			1		
1			1		
0	1	1	1	1	1
-1			1		
-2			1		

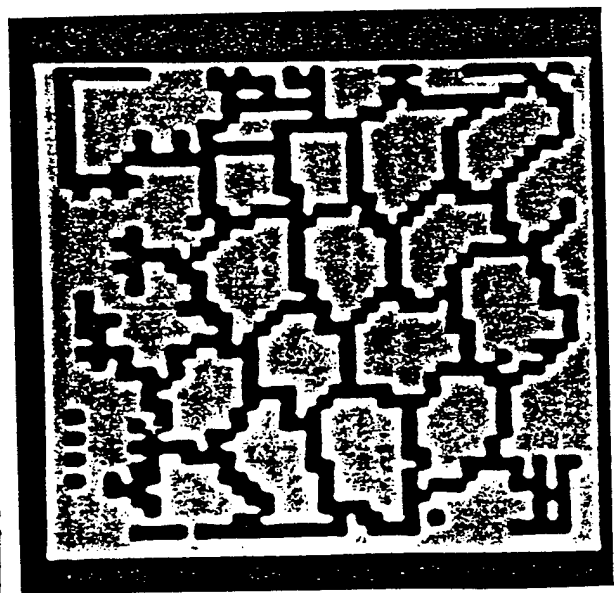
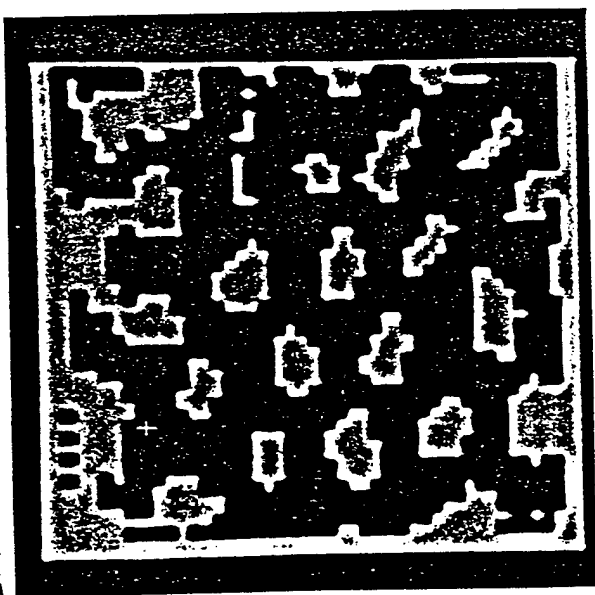
Figure 4.1.12. "Rolling Ball" template T_{ij} .

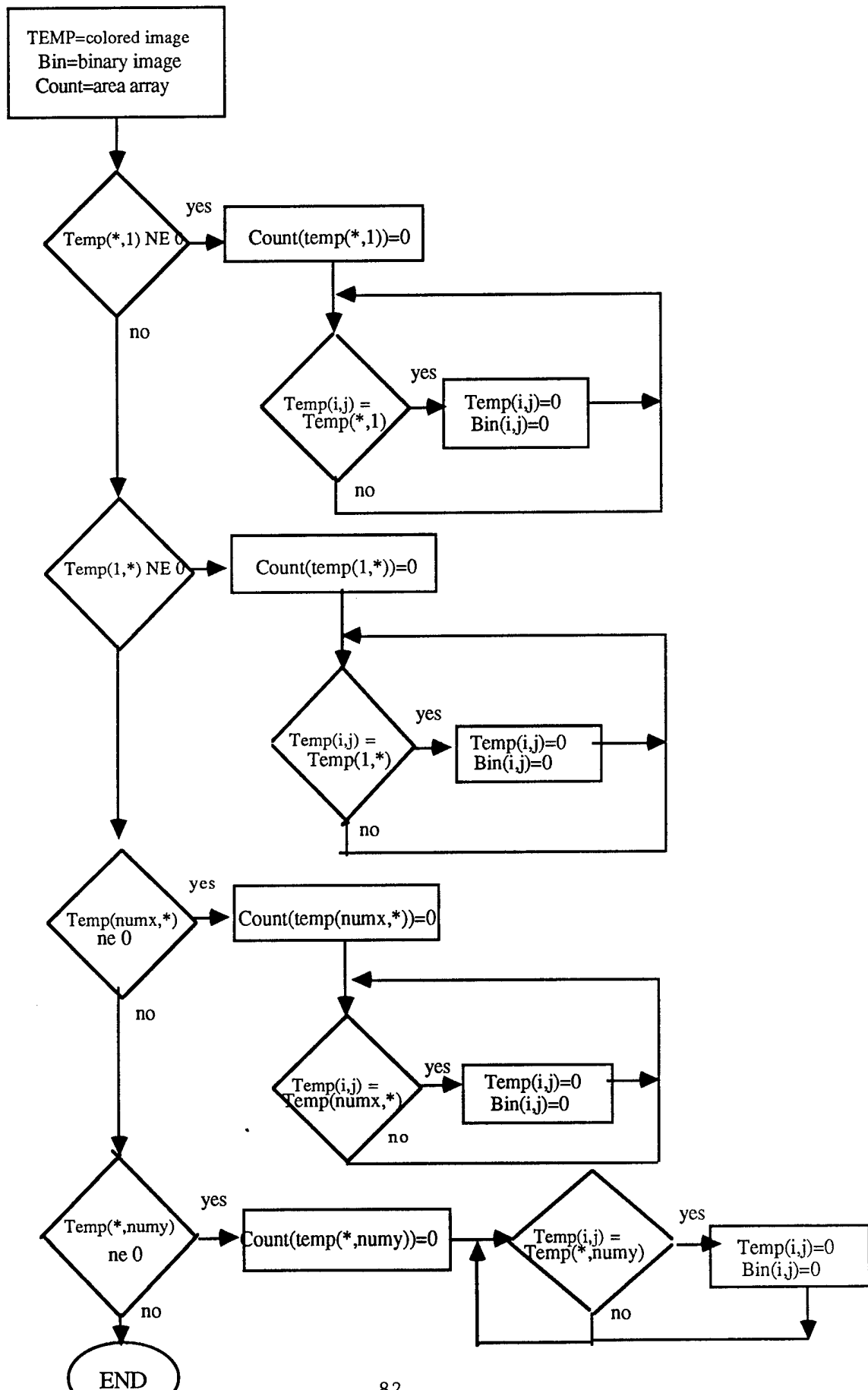
$$\text{BIN}(i,j) = \begin{cases} 1 & \text{if } \sum_{x=i-2}^{i+2} \sum_{y=j-2}^{j+2} \text{bin}(x,y) T(i-x,j-y) \neq 0 \\ 0 & \text{otherwise} \end{cases} \quad (2)$$

This is repeated until the limiting criteria has become true: no object in the binary image can be dilated any more. The acceptance of a point as part of an object depends on the location of the point in question: if this point is already a neighbor of some other object then it is not incorporated as part of the object; it is assigned as a boundary between the two neighboring objects. While the object dilation was taking place, the number of pixels inside each cell were being added to the ones counted while finding the centers. The pixels with the same value in the colored image TEMP belong to one same cell. Now all the data has been collected to plot the distribution function. Figure 4.1.13 shows the object dilation algorithm.



Once the dilation is completed, the cells that have part of them touching the edges of the window being analyzed are discarded because they are not completely included in the unit area being analyzed. This is done by going around the edges of the window and storing the cell number of each cell that touches the edges of the image TEMP. All the pixels that have a value similar to the ones found on the edges are turned to zero. The pixels on the binary image BIN that are on the same location that the ones on TEMP that are turned zero are turned zero too. The location on the array COUNT where the area of the particular cell that is being removed was stored is turned to zero because that area is not going to be included in the cell area distribution function because it does not correspond to the area of a complete cell. The remaining cells are recounted and their areas are plotted in a cell distribution plot. Figure 4.1.14 shows the incomplete cell removal algorithm, where numx and numy are the dimensions of the window (columns and rows, respectively.)





4.1. IMAGE EDITING

Some images, after applying the LOG operator and both adaptive and binary thresholding, have cell centers that are connected with each other (see Figure 4.1a.1.) When these centers are dilated they become one big cell instead of two of normal size. There are also cases where the resulting images have boundaries that do not correspond to a cell on the original image, cells that area divided in two or more pieces (see Figure 4.1a.1.) These abnormalities bring as a consequence an increase in the standard deviation of the distribution function and a variation of the mean cell area. To avoid any kind of erroneous information that may ruin the distribution function some interactive editing has to be performed on the image to make it more accurate and more similar to the original image.

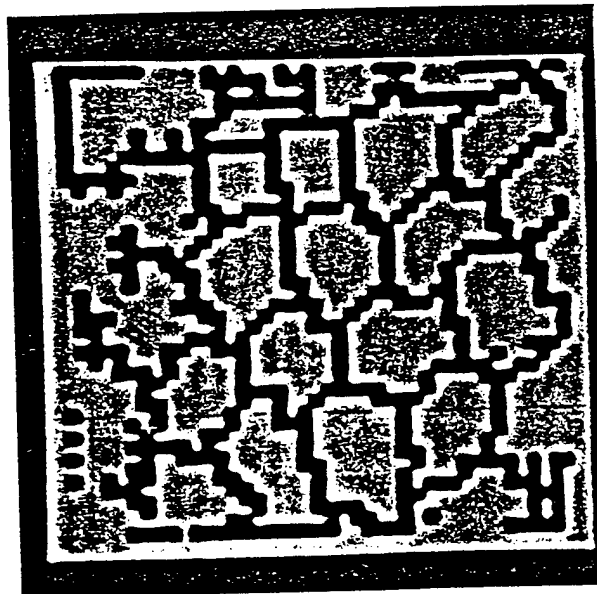


Figure 4.1a.1. Example of an image with missing boundaries.

The editing process consists on drawing with the mouse boundaries where there are missing and eliminate false boundaries. Displaying the original image and the dilated one side by side on the monitor it can be seen where there is a cell boundary missing and draw it or a false edge and eliminate it. When the boundary is drawn, it can be examined in the colored image TEMP which cell was divided. With the divided-cell number it is known the location of the area of that specific cell on the COUNT array where all the areas are stored (the location on the array equals the cell number on TEMP.) This number is automatically divided by two and copied one more time to make it count as the new cell that was formed when the big one was divided.

When false boundaries have to be eliminated, the mouse is positioned and clicked inside the pieces of cell that should form one whole cell. The areas that correspond to the two pieces that are going to merge are added and the two separate area are turned to zero. Figure 4.1a.2. shows the image on Figure 4.1a.1. after it has been edited. Figure 4.1a.3. shows the editing algorithm.

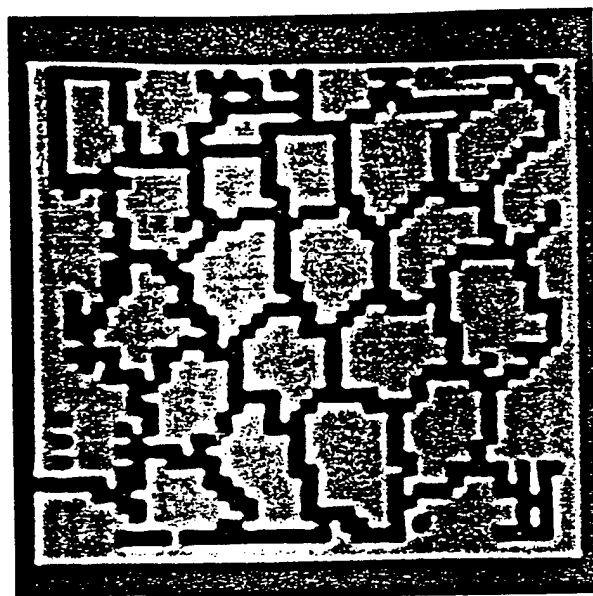


Figure 4.1a.2. Image shown on Fig. 4.1a.1. after editing.

After performing several experiments it was shown that the standard deviation decreased considerably when editing the images and the mean cell area resembled more to the one obtained with manual methods. Figure 4.1a.4a shows the cell distribution function of a sample of approximately 100 cells of a cat's eye obtained with the automated technique without editing the dilated image and the cell distribution function obtained from the same sample but after editing the dilated image. It is clearly shown that the distribution function of the edited image. is more smooth and it has a better Gaussian distribution than the unedited one.

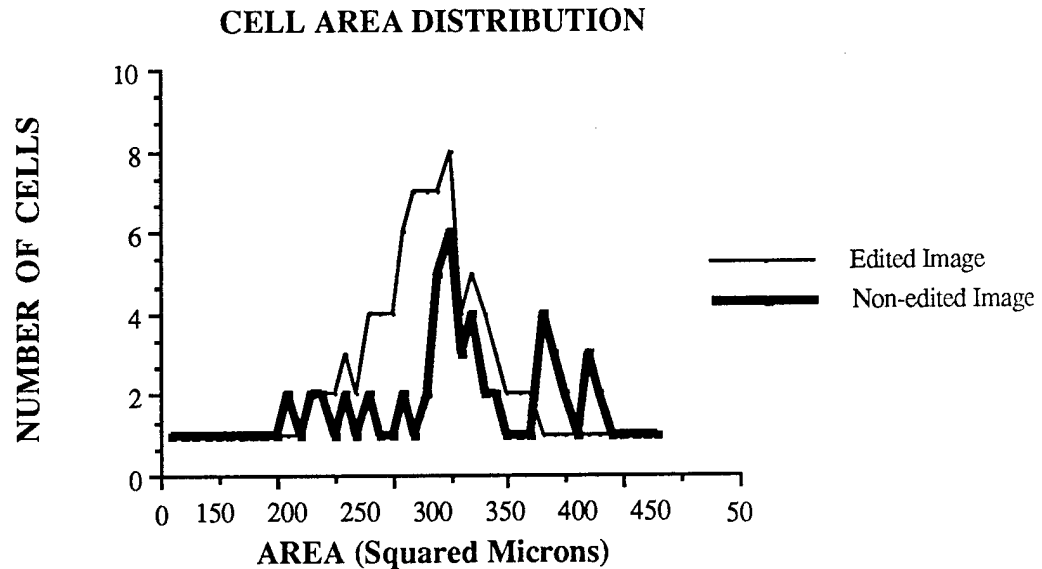


Figure 4.1a.4. Cell area distribution obtained with the automated algorithm.

(Mean Cell Area = 298 m^2 . Standard Deviation = 62) and after editing the resulting image (Mean Cell Area = 310 m^2 . Standard Deviation = 48.)

The area size has to be translated from pixels to squared microns. The width of the slit image obtained from the slit lamp is $0.2 \text{ mm} = 200 \text{ m} = 186$ pixels. The pixel (picture element) is assumed to be squared. From the above equation is deduced that one side of a pixel measures 1.0753 m . The area of one pixel will therefore be 1.1562 m^2 . To obtain the area of the cells in microns the values obtained have to be multiplied by 1.1562 before plotting the area distribution function. Figure 4.1.14 shows the cell area distribution of a normal corneal endothelium containing approximately 100 cells per unit area.

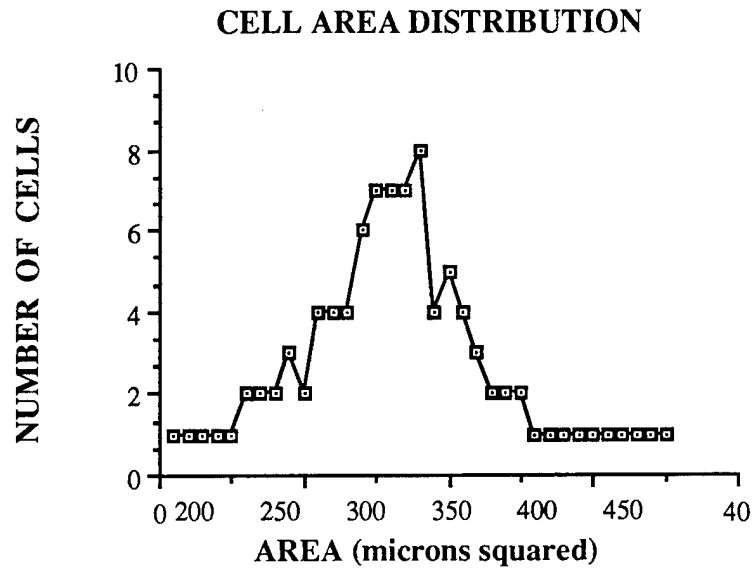


Figure 4.1.14. Cell area distribution of a normal corneal endothelium (100 cells.)

$$\text{BIN}(i,j) = \begin{cases} 1 & \text{if } \sum_{x=i-2}^{i+2} \sum_{y=j-2}^{j+2} \text{bin}(x,y) T(i-x,j-y) \neq 0 \\ 0 & \text{otherwise} \end{cases} \quad (2)$$

$$\text{SUM} = \sum_{x=i-1}^{i+1} \sum_{y=j-1}^{j+1} \text{bin}(x,y) T(i-x,j-y)$$

4.2. HAND-TRACED ALGORITHM

A hand-traced algorithm was implemented in order to measure the accuracy of the automated technique previously described. This algorithm consists of drawing a white line over the cell boundaries. To draw the cell boundaries the Bresenham algorithm was implemented [56]. This algorithm consists of calculating the most optimal way of drawing a line between two pixel coordinates.

The cells are traced one at a time and at the end of each trace, the area for that specific cell is calculated by summing area of triangles. Figure 1 shows how any polygon can be divided into a number of triangles. This implies that the sum of the areas of all the triangles that form the polygon equal the area of the polygon itself.

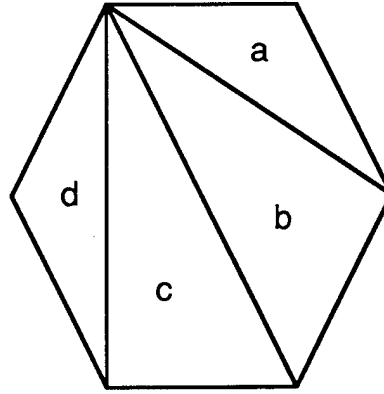


Figure 1. Area of hexagon = $a+b+c+d$

Figure 2 shows how the area of each of the triangles in a coordinate system is calculated.

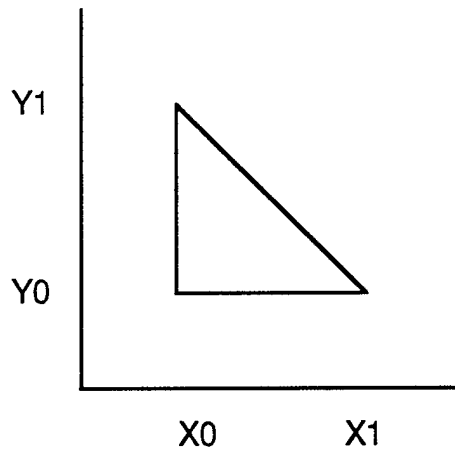


Figure 2. Area of triangle = $((x1-x0) * (y1-y0))/2$

After calculating the areas of the four triangles that form the hexagon, these are stored in an array ,COUNTij, to calculate the cell area distribution. Once the areas are calculated, the same algorithm applied for obtaining the

cell area distribution on the automated technique in chapter 4.1 is applied to the values obtained with the hand-traced algorithm. Figure 3 shows the resulting original image after hand-tracing the cell boundaries.

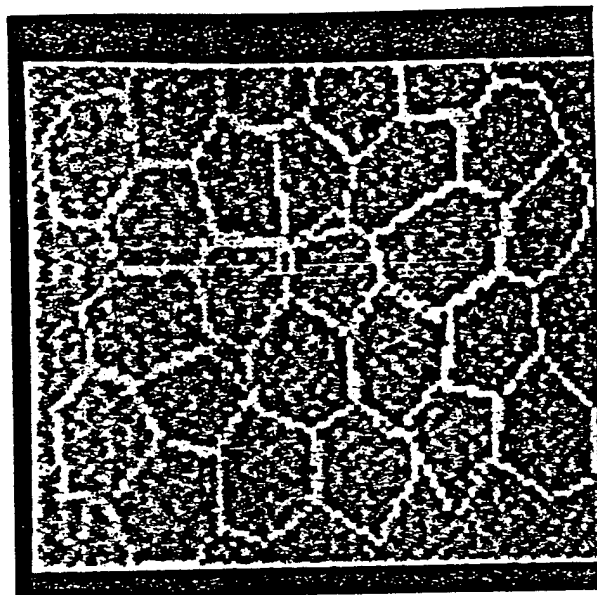


Figure 3. Image with hand-traced boundaries.

After both methods have been applied to the same image, the cell area distributions obtained by both methods are compared to see how accurate the automated method is.

COMPARISON OF AUTOMATED AND MANUAL METHODS FOR CELL SIZE AND DISTRIBUTION

To measure the accuracy and consistency of the automated method, a manual tracing method was also applied to analyze a specific set of data. The binary image containing the cell centers was overlaid on the manual traced image. Figure 5.1. shows that every cell center obtained with the automated method corresponds to one specific cell in the original image.

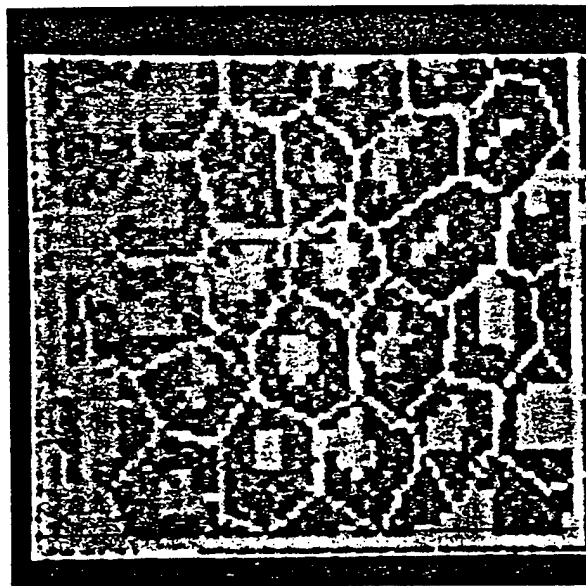


Figure 5.1. Manual traced image with binary image overlaid.

Five cat's eyes and five rabbit's eyes were analyzed. Several images were obtained from each eye to choose those with the best resolution. The animals were put under anesthesia for a period of two hours each session.

During this time, an average of five images were digitized and stored in the IBM PC. Approximately one hundred cells were counted in each eye to obtain a statistically significant population, requiring a minimum of two images for each eye to be analyzed.

The average size of an endothelial cell from a cat and from a rabbit is $320 \mu^2$ and $304 \mu^2$, respectively [73,74]. The corneal endothelial cell area distribution, in general, resembles a Gaussian distribution, like the one in figure 5.1a. When the cells are damaged, this function becomes more spread out (see Figure 5.1b.)

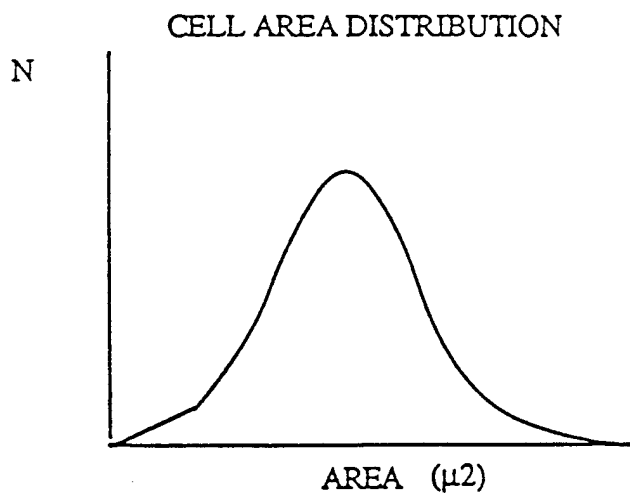


Figure 5.1a. Cell area distribution of a normal cornea.

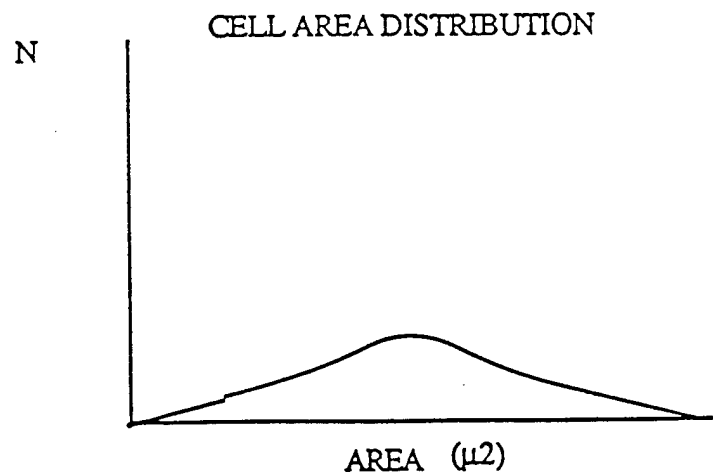


Figure 5.1b. Cell area distribution of a damaged cornea.

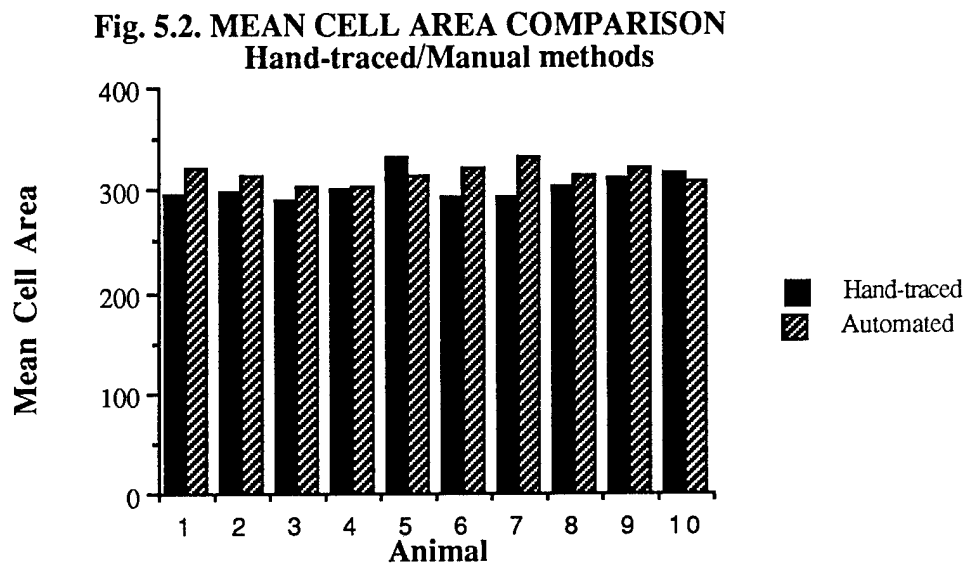
The same portion of the digitized image was analyzed by the automated and the manual method. The same number of cells were counted

with each method. With the hand-traced technique only the cells that are completely inside the image were counted because the ones near the boundary have very blurred edges and are indistinguishable to the human eye. For this reason, when the image is analyzed with the automated algorithm, once it has found all the boundaries, the algorithm discards all the cells which have a part touching the edge of the analysis window. Table 5.1 shows the cell area distributions obtained with the hand-traced and automated techniques.

Hand-traced Method		Automated Method	
Mean Area	Std. Deviation	Mean Area	Std. Deviation
296	49	322	65
298	51	315	58
290	48	304	66
300	53	302	59
332	66	315	67
293	56	322	58
294	52	332	59
304	41	315	61
310	47	321	61
316	54	308	64

Table 5.1. Comparison of mean cell areas obtained with the hand-traced and automated techniques from samples of cats (1-5) and rabbits (6-10) corneal endothelium. Each sample consisted of @ 100 cells.

Figure 5.2 shows the correlation between the mean cell areas of the different populations of eyes of cats (animal No.'s 1-5) and rabbits (No.'s 6-10) analyzed by both methods.



In some of the experiments the mean cell area in the automated techniques resulted somewhat larger than the ones measured with the hand-traced algorithm because the automated algorithm assumes that all objects bigger than a certain size are cells. Even though most of the objects bigger than the size set as threshold are indeed cells, some of them are noise from the image. The threshold could not be set any lower because it would have removed all the smaller cells from the image and the cell area distribution would have been biased. Another situation where cells are treated differently on both methods is when they lay near the image boundaries. In the automated method these cells may be dilated until they touch the boundary, but they are totally inside the image so they are counted as a complete cell. Sometimes they are dilated to a size a little bigger than their original size so

they bring up the mean area of the population of cells. This does not happen very often and when it does happen, they are removed from the image because they are not considered as part of the window.

The subjectivity with which the operator traces the cells must be considered. A distance of a few pixels is beyond the resolution of the human eye, but it corresponds to 15-20 μm^2 on the image; one can not really say that the hand-traced cells correspond exactly to the real cell boundaries.

The distribution functions obtained using the two techniques came out satisfactorily similar. The cell areas calculated with the hand-traced technique were more uniform than the ones obtained with the automated algorithm; the standard deviation was a little greater on the automatic counting but the average areas were very similar; they did not differ in more than 10% in any of the cases studied. Figures 5.2a through 5.7b show the cell area distribution function of each cat's eye obtained with the manual tracing and automated method. Figures 5.8a through 5.11b correspond to the cell area distribution of the five rabbit's eyes analyzed.

The averages were taken from a population of 100 cells (± 5 .) The average of the ten averages taken was 303.3 $\mu\text{m}^2 \pm 48$ for the manual-traced technique and 315.3 $\mu\text{m}^2 \pm 62$ for the automated techniques. The results obtained with the automated method were very close to the ones obtained with the hand-traced method and similar to values for the mean cell areas obtained in the literature [73-76]. There was not a noticeable difference between the analysis made on the cats' eyes and the ones made on the rabbits' eyes.

EVALUATION OF THE AUTOMATED IMAGE ANALYSIS OF CORNEAL ENDOTHELIAL CELLS

The automated algorithm was successfully applied to a number of images of corneal endothelial cells of rabbits and cats. The results obtained with the automated method were satisfactorily similar to the ones obtained with the hand-traced technique.

The method chosen to grab the image, directly from the microscope to the computer through a frame grabber board, proved to be the optimal one. It permitted immediate checking of the quality of the stored image information; no intermediate processing such as recording on video tape was necessary. The use of the strobe light proved an excellent choice for minimizing the blurring of images due to eye movements.

To improve the accuracy of the analysis, an image editing technique was sometimes necessary. When the binary image contains cell centers that are connected with each other they are dilated as one big cell. This brings as a consequence a considerable increase on the standard deviation of the cell area distribution function corresponding to that window. In this cases, an image editing technique is applied where missing boundaries are added to the image to divide two or more cells. It is also applied when false boundaries are formed and need to be removed. This improved the mean cell area as well as the standard deviation on the experimental protocol.

A population of one hundred cells were analyzed from each of the eyes chosen. To achieve this, a minimum of two images of each eye had to be analyzed because of the small amount of cells that were traceable in each image. In some of the experiments the mean cell area in the automated techniques resulted larger than the ones measured with the hand-traced algorithm but the differences were not statistically significant. The processed image physically resembled the original image; there were no false or incomplete boundaries.

A total of five rabbits and five cats were analyzed. The results obtained by both methods did not differ in more than 10% in any of the cases studied. It was proven that the automated method implemented is accurate enough to be used for analysis of endothelial cell morphology.

Another parameter that could be measured in the future with the automated algorithm is the polygonality of the corneal endothelial cells [75]. It has been proven that cells lose their shape due to different factors like age, trauma and surgeries [52,53,57,7]. The polygonality can be analyzed by counting the number of neighboring cells. Since in the algorithm explained each cell has a number assigned, it would be very easy to count how many different cells are neighbors of a specific cell.

Chapter 6

EXPERIMENTAL METHODS AND MATERIALS FOR DATA COLLECTION AT THE RF FACILITY AT BROOKS AIR FORCE BASE, SAN ANTONIO, TEXAS

6.1 ANIMAL RESTRAINT AND HARDWARE SPECIFICATIONS

6.1.1 Animal Selection

The rabbit corneal endothelium is known to regenerate itself through cell division regaining its normal state within days. In contrast, cat endothelium wound repair takes place without cell division and is more analogous to that of man [78]. Due to this similarity between the endothelium of the cat and man, the cat was chosen as a good model for the study of RFR effects. Once a cell is damaged cells surrounding the wound undergo enlargement, elongation towards the wound to cover the defect. Next cells rearrange by changing neighbors in such a way that they retained their enlarged size but recovered their elongated shape. An overall reduction in the number of cells per area results. Another factor which is important in selecting cats over rabbits and monkeys is that rabbits are severely myopic with a very large lens approximately 7-8 mm thick, which is almost one half of the entire diameter of the eyeball. In the monkey, man and cats the lens is about 4 mm thick and occupies about one fifth of the diameter of the eyeball. But the monkey has deep-seated eyes and well developed orbital rims that act to shield the eye more effectively from RFR exposure. In contrast humans and cats have less deep-seated eyes and less developed orbital rims. Overall,

the cat eye due to its similarity in endothelial cell healing and in anatomy proves to be the best model for man.

6.1.2 EXPERIMENTAL APPARATUS

Figure 6-1 is a block diagram of the experimental apparatus. The important components utilized in obtaining the endothelial micrographs and the thermal data are shown. The animal was given a preanesthetic Ketamine at a dose of 20 mg/kg and then were given an anesthetic, Xylazine, at a dose of 1 mg/kg. This dose keeps the animal under for a period of two hours. The eye is moisturized with a saline solution every five minute so it will not dry out. The animal's head is put in an orthoplast mask. This mask is made of orthoplast, a porous material that, when heated, can be bent into a desired position and once it is cold it stays in that position permanently. Each animal has its own mask because every head has different dimensions and shapes. This mask is placed on the animals head and is tied, through some of the holes present in the material, to the head holder bar. This configuration was proven the most optimal for reducing head movement. The body of the animal was supported on a bed of foam on a platform which was isolated from the head restraining apparatus. This attenuated the movements of the body caused by ventilation from being transmitted to the head during the RF exposure. The animal and restraining apparatus were placed in a 4.5 X 6 X 3m anechoic chamber which had absorbing material on all sides and on the floor to prevent RFR scattering. An air conditioning vent was located at the top of the room which allowed for convective air flow around the animal. The temperature inside the chamber was measured during exposure sessions and remained within ± 2 C of 25 C. The 35 GHz continuous wave microwaves were generated by the Millimeter Wave Exposure System made by Applied

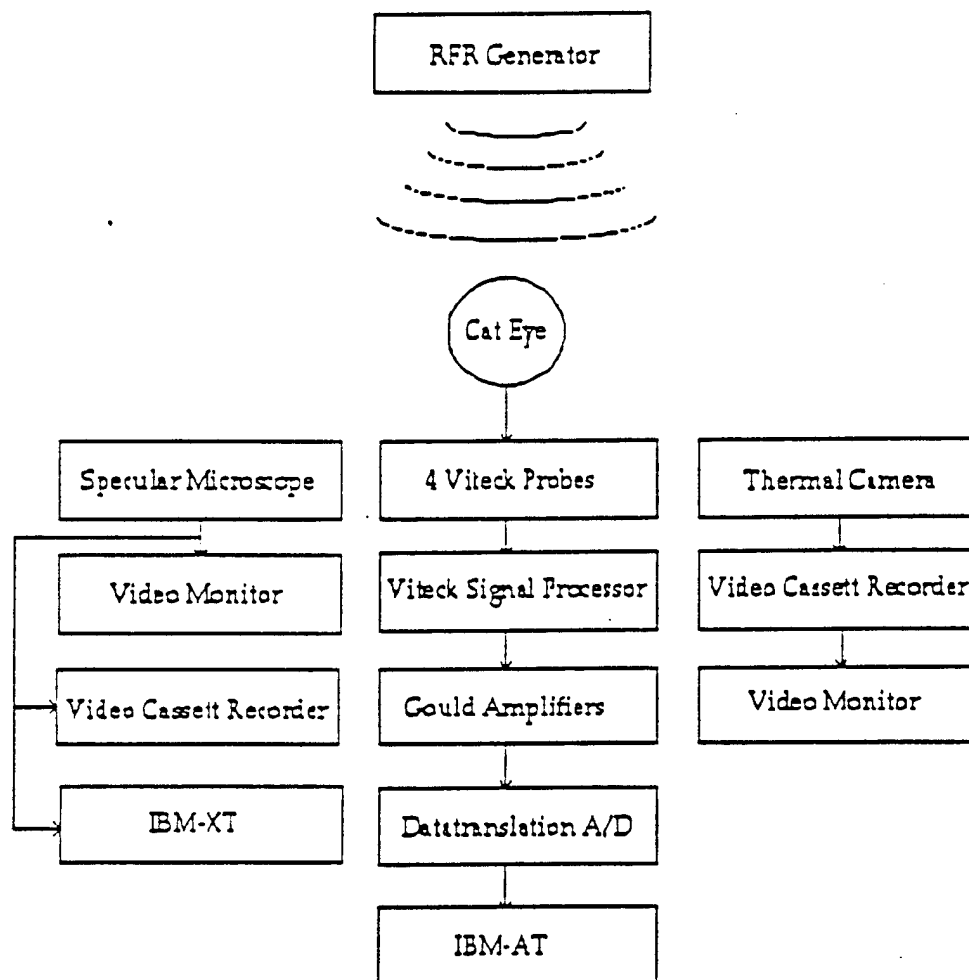


Figure 6.1 Block Diagram of Experimental Apparatus
Used in Obtaining Thermal Data from the Eye of Cats
Being Exposed to Radiofrequency Radiation.

Electromagnetics, Inc. The system characteristics for 35 GHz and 94.5 GHz are given in Table 6-1.

Table 6-1.

Transmitter Characteristics at 35 GHz and 94.5 GHz [51].

RF Frequencies:	35 and 94.5 GHz, +/- 1%
RF Power @ 35 GHz:	75 watts minimum
RF Power @ 94.5 GHz:	50 watts minimum
Modes:	Continuous Wave or Pulsed
Pulse Repetition Frequency:	10 kHz to 100 kHz

The Millimeter Wave Exposure system was calibrated at 94.5 GHz March 10, 1988 by the Varian Canada Microwave Division.

The animal and the restraining apparatus were positioned so that a specular microscope could view the eye during microwave exposure. The specular microscope was at a 45° angle from the plane of the eye and microwave source, and the specular microscope was positioned during the exposure so that the endothelial cells could be viewed. In focus the microscope was at a distance of 1.5 cm from the cornea. The specular microscope partially blocked one eye from microwave radiation. The eye of the cat under study was kept open by a speculum and 1 drop of .45% N salt solution every 90 seconds lubricated the eye during the exposure.

The microwave power density at the cornea was determined prior to each exposure through a 35 GHz electromagnetic probe. During several 10 mW/cm² exposures, body core temperatures were monitored to examine the effects of the anesthesia on the core temperature. At this low power dosage

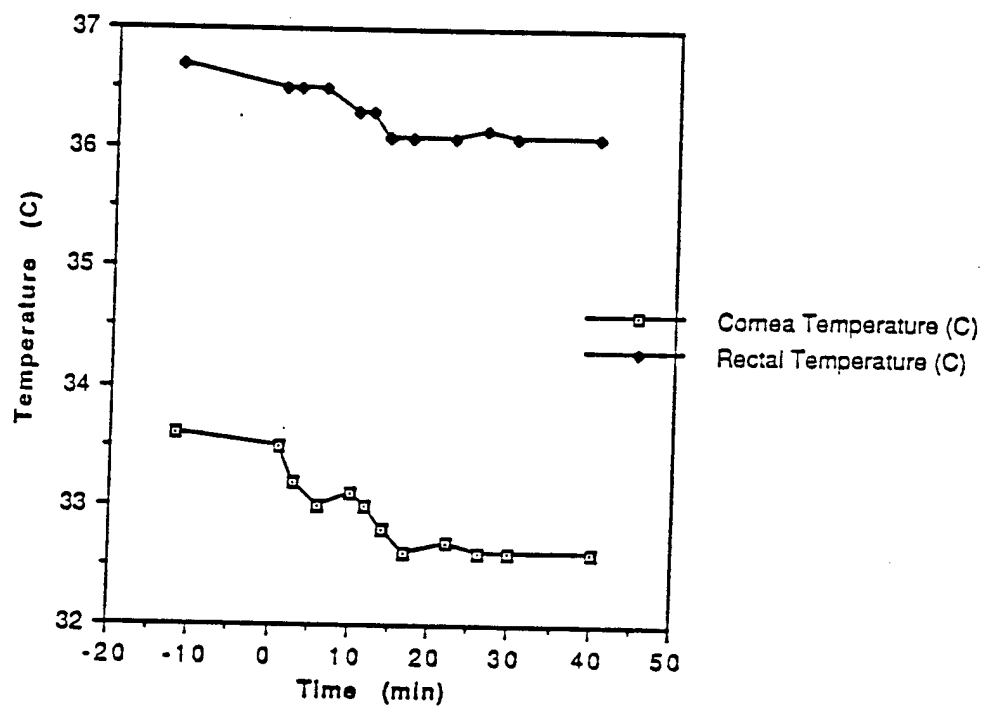


Figure 6.2. Effects of anesthesia during 35 GHz 10 mW/cm² exposure.

very little heating on the surface of the eye was detected. A baseline temperature of 36.5 C was a typical core temperature measured 10 minutes prior to exposure. The rectal temperature was recorded every 5 minutes for one hour after the exposure was initiated. A steady decrease in temperature was noted until an average steady-state condition of 36.0 C was reached. Figure 6-2 shows the typical effects of the anesthesia on the core temperature of the animal during 10 mW/cm² exposure. The anesthesia had the tendency to slow metabolism; thus, lowering the body temperature.

6.3 ENDOTHELIAL CELL MORPHOLOGY ACQUISITION

The images to be analyzed are obtained from the corneal endothelial cells of cats as viewed through a TOPCON slit lamp specular photo microscope model SL-6E.

The endothelial cells are observed from the center of the field of view, allowing for evaluation of the shape and spatial density. The area photographed is 1.0 mm long by 0.16 mm wide. The distance between the objective lens of the specular microscope and the corneal vertex of the animal's eye is 15 mm.

Two stepper motors are attached to the slit lamp that allow remote focusing and scanning for operation of experiments conducted in intense electromagnetic fields. A DAGE model CCD71 video camera, designed specifically for low light microscopy and quantitative electronic imaging is also attached to the microscope. This configuration is shown on figure 3.1.

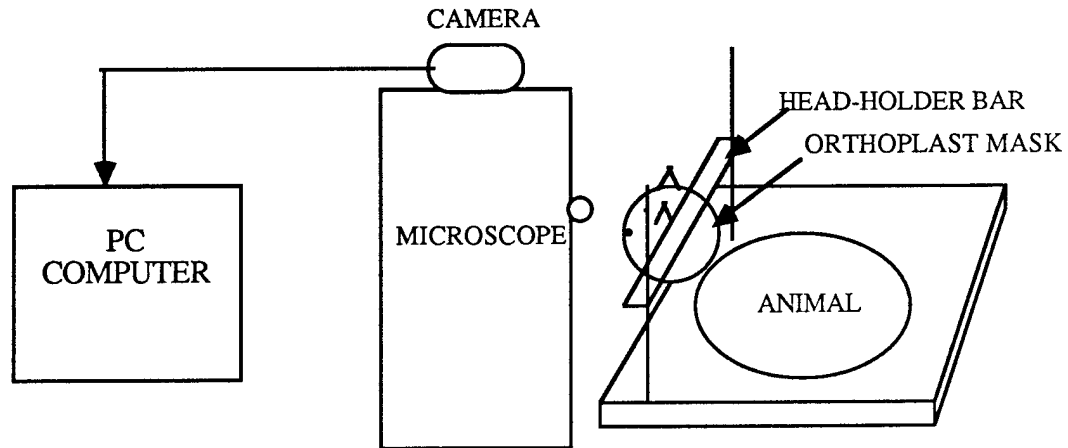


Figure 6.3. Animal set-up and system configuration for obtaining images.

The analog signal is converted into a digital image through a frame grabber board and is stored in the memory of a computer for subsequent analysis.

The image acquisition process has been implemented on an IBM PC/AT microcomputer system equipped with a Metrabyte frame grabber board which can convert a single video frame into a 512 X 480 image in 1/30 sec. The microcomputer has 512 Kbytes RAM on board and a 20 Mbyte hard disk. Image acquisition is performed in sync with the slit lamp strobe light and the video camera through a sync controller box. This box controls the vertical sync of the camera and the strobe controller box which turns the strobe light on when the control manual switch is pressed. At the same instant the switch is pressed the image that is being displayed on the monitor

is grabbed by the frame grabber board. The function of the strobe light in this configuration is to freeze the moving images in time by providing an illumination period that is short with respect to the time constant for minor eye movement. At the operator's discretion, the frozen image is stored on the hard disk for later analysis. Figure 6.3 shows the configuration of the image grabbing system.

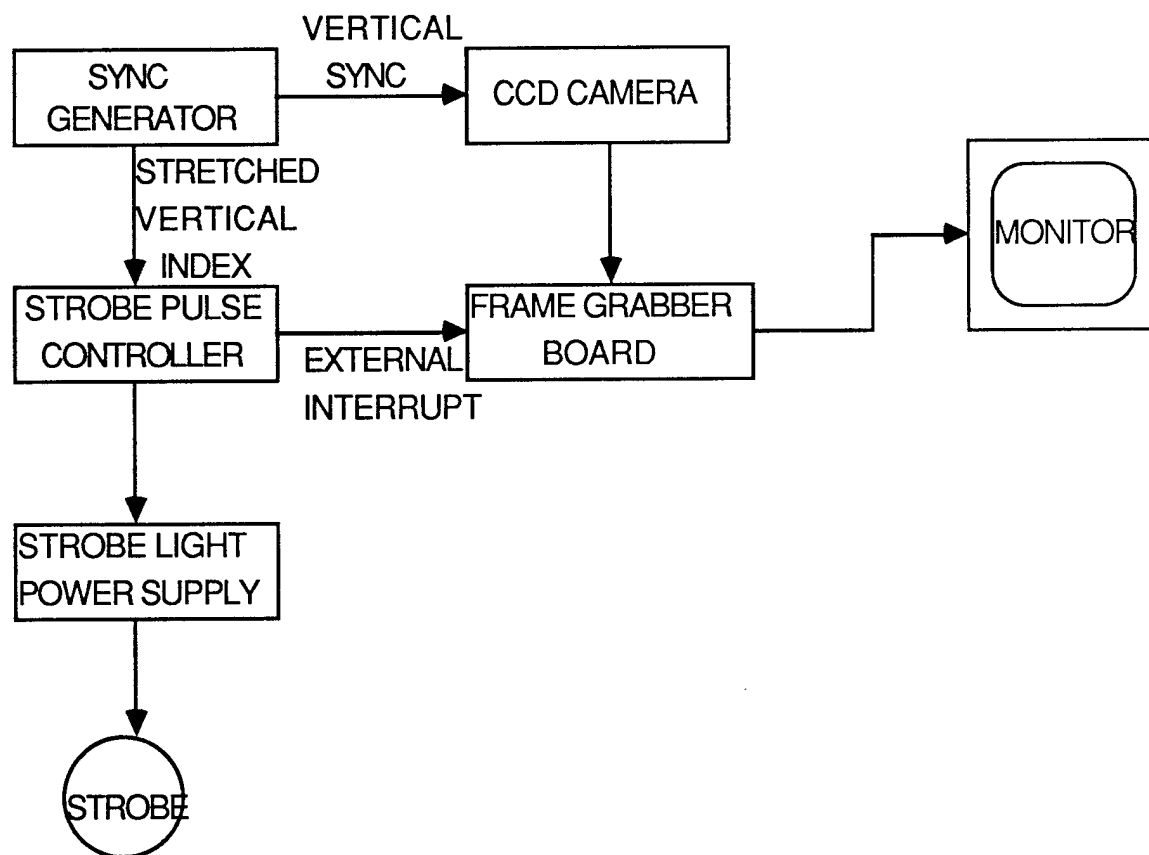


Figure 6.4. Configuration of the image grabbing and digitizing system.

6.4 THERMAL DATA ACQUISITION

To obtain internal thermal data of the eye Vitech thermistor probes were used. The thermistors were surgically implanted and were placed 3mm, 8mm and 15 mm from the apex of the cornea and within the fat region surrounding the eye. These locations correspond to the anterior chamber, retrolenticular region, vitreous humor and periorbital region. The signal from the thermistors was amplified by Gould amplifiers and then transmitted to an Datatranslation 2801 analog to digital board for digitizing. The 4 digitized signals were then stored onto a harddisk. Surface thermal data for eye was obtained with an Inframetrics 600L thermal camera and stored on a video cassette recorder.

6.5 Thermal Camera Characteristics

Thermographic analysis of the eye was achieved by the use of the model 600L infrared thermal imaging system (Inframetrics, Inc., Bedford, Massachusetts). The system operates in the 8-14 μ m wavelength and utilizes the relationship between infrared radiation, emissivity, and absolute temperature in order to produce a two-dimensional image of a surface. Two low inertia scanning mirrors which are rotated by a magnetic field guide the infrared radiation to a liquid nitrogen-cooled Mercury-Cadmium-Telluride (HgCdTe) detector which converts the radiation to an electrical signal that can be viewed as video. The thermal camera was calibrated with a black body. Black bodies are designed to remain at constant temperature and give an emissivity of approximately one. By monitoring the temperature of the body with thermistors, the temperatures in the image can be calibrated with respect to their gray levels.

The field of view of the camera was adjusted so that the entire eye could be easily discerned on the monitor. The temperature range was set to 20.0 C, with a lower bound of 25.0 C and an upper bound of 45.0 C. The range adjustment acts as a DC offset in determining which particular temperature range is monitored, determining the minimum and maximum temperature which can be measured. An option that allowed for the temperature of a square area to be display on the monitor was used to evaluate the surface temperature of the cat eye. This option was used to obtain an average temperature over the surface of the eye which was recorded on video.

Since the thermal camera was positioned within the anechoic chamber, refilling with liquid nitrogen could not be performed during the 2 hour exposure time. The thermal camera tended to shut down 1 to 1.5 hours after exposure was initiated depending on the amount of liquid nitrogen in the thermal camera.

6.6 Thermistor Digitization

Viteck Model 101 Electrothermia Monitor are specifically designed to measure temperature in lossy materials, such as animal tissue or substance with high water content, that are being heated with electromagnetic energy. The monitor consists of a thermistor probe, an electronics package and an interconnecting cable. The thermistor tips are constructed of four slightly conducting plastic leads in teflon sheaths which are 1 mm in diameter and 37 cm long. The thermistor leads have linear resistances greater than 100 kohm/cm and cause only slight perturbations of the electrical field in lossy materials [38]. The thermistor resistance is sensed by passing a current through the thermistor by means of two leads and observing the thermistor

voltage developed by the current. The voltage is sensed with a high-input-impedance amplifier so that no significant voltage drop occurs across the very high lead resistance.

The electronics package is designed to operate and provide accurate temperatures over the important range of 20 C to 50 C. In addition to a digital display (0.1 resolution), two analog outputs are provided for recording purposes. Table 6-2 gives the characteristic performance of the Viteck Model 101.

Table 6-2.
Viteck Model 101 typical characteristics [50].

Sensitivity	0.01 C
Linearity	+/- 0.07 form 20 to 50 C
Accuracy	.1 C

The thermistors were surgically implanted prior to the animal being placed on the restraining apparatus. Extension cables were connected to the thermistors. The cables were guided outside of the anechoic chamber through a small hole in the wall. The signal was then processed by a the small Viteck electronics package to give an output signal of 10 mV/C. This signal was then amplified by a factor of 10 by a Gould amplifier; thus, the signal entering the Datatranslation 2801 A/D board was at 0.1 V/ C. The A/D board is a 12 bit board; thus, the smallest temperature difference that could be detected was .024 C. The lowest possible measurable temperature is 0 C while the highest possible measurable temperature is 100 C. The dynamic

temperature range expected for the eye was between 25 C and 45 C for the power densities and frequencies that were used. The 4 channels to the A/D board were scanned at 4 channels per second for a total of 7000 seconds.

CHAPTER 7

EXPERIMENTAL RESULTS

7.1 Eye Temperature Experimental Results

The experimental thermal data obtained using three thermal couples positioned axially through the eye and one thermal couple in a periorbital position in a fat layer surrounding the eye are shown for different exposure power densities in Figures 7.1 and Figure 7.2.

The results of exposure at 75 mW/cm^2 is shown in Figure 7.1. The decrease in temperature at 1400, 2300 and 3200 seconds was caused by loss of microwave energy due to the generator overheating and then shutting down. Although the generator shut down, enough data was obtained to make some observations.

The experimental data did not agree with predicted temperature contours produced by the transient two-dimensional axisymmetric SAR forcing function model. The trends shown in the experimental data can be compared to computer simulation runs at 200 mW/cm^2 and 2.45 GHz in Chapter 3. Figure 3-10 shows the temperature contours which are to be expected with normal perfusion rates. The figure shows that the temperatures within the tissue layers should vary from highest to lowest in the order of: the lens, anterior chamber and vitreous humor. This does not agree with the experimental data which shows that the vitreous humor reaches the highest temperature followed by periorbital region, the lens and the anterior chamber. One problem that is obvious with the simulated runs is that the entire eye was assumed to be at a initial temperature of 34 C. The experimental data clearly shows that the tissue layers are initially at different temperatures.

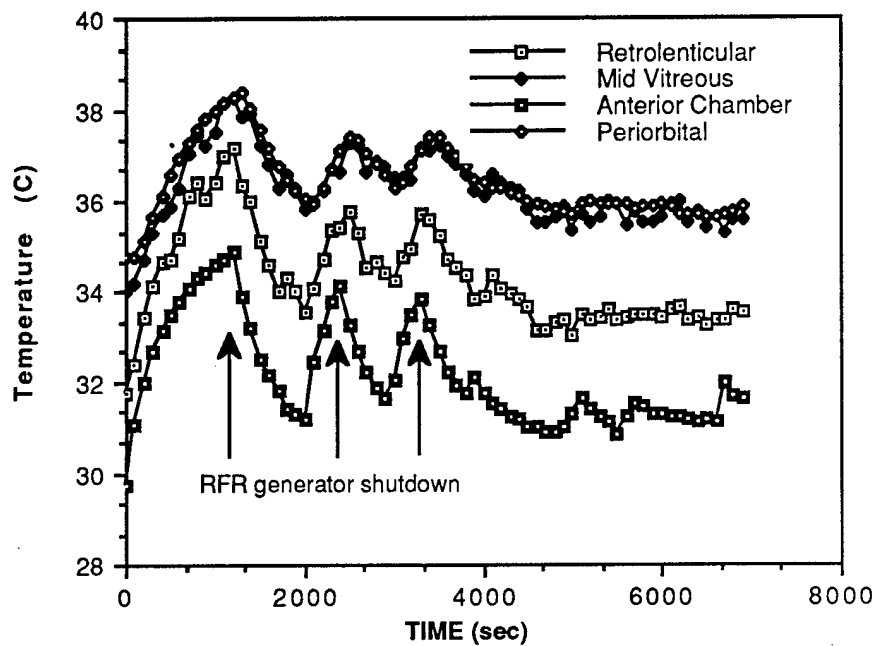


Figure 7.1 Measured temperatures within the eye and surrounding tissue during 35 GHz 125 mW/cm sq exposure

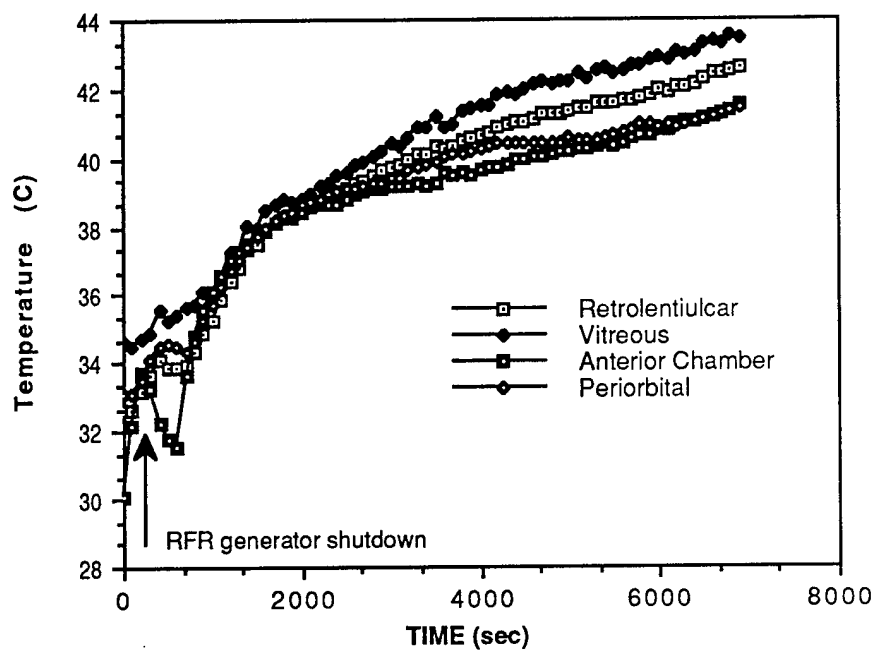


Figure 7.2 Measured temperatures within the eye and surrounding tissue during 35 GHz 125 mW/cm sq exposure.

The results of exposure at 125 mW/cm^2 is shown in Figure 7.2. The microwave generator once again shut down due to overheating early in the study. The discontinuity of the heating source is clearly evident in the experimental record at 700 seconds. The temperatures of the tissue layers closer to the front of the eye show a greater response to the removal of the heat source than do the deeper seated tissues; thus, the effects of convection to the ambient temperature are clearly shown. Unlike the previous study the highest temperatures occurred in the periorbital region. The depth of insertion of the probe probably was not the same in both experiments. The probe in the periorbital region was not sutured into place as the other probes were, so it could of come out of position. But, both experiments show that the periorbital region is heating relatively high. Another reason for the discrepancy between the experimental data and the the finite element model is that the core body temperature increased with time greater than expected. In later studies, animals which were repeatedly exposed to 100 mW/cm^2 developed third degree burns in the chest area. This revealed that the peak power intensity was not occurring at eye level as desired. This oversight lead to the body temperature and the perfused blood temperature within the eye to increase with time. The rectal temperature during the experiment increased from 36.5 C to 39.0 C . It is also should be noted that the curves tend not to go to steady state. This also can be attributed to the body temperature of the animal increasing throughout the study.

7.2 Discussion of Experimental Thermal Results

An initial temperature gradient which takes care of the problem mentioned earlier associated with the entire eye assumed to be at 34 C , and

the convection coefficient should be changed to $.01 \text{ W/cm}^2 \text{ C}$ from $.001 \text{ W/cm}^2 \text{ C}$ at the surface of the cornea because the eye solution that is dropped onto the eye every 90 seconds tended to accumulate. The change in the convection data is warranted because in our experimental protocol we lubricated the eye; whereas, Kramar et al. [19] did not lubricate the eye. The convection coefficient for the rest of the tissue exposed to the ambient temperature will be left at $.001 \text{ W/cm}^2$. Also, the blood perfusion temperature of 34 C is rather low. The perfused blood being maintained at 38 C is a better simulation due to the increase in core temperature at high dosages which occurred in the experimental runs. At doses above 75 mW/cm^2 , the core body temperature elevated to as high as 39.5 degrees during the exposure. Also, including a no flow boundary condition at the lower boundary would have a tendency to cause heat to accumulate in the posterior regions of the eye. Overall, the initial temperature gradient, the higher blood perfusion temperature, and implementing no flow boundary conditions at the lower boundary will cause the peak temperatures to be more posterior as in the experimental data. Also, including a forcing function that is dependent on the frequency and electrical properties of the tissue may give other insights into the reason why the highest temperatures occur posteriorly and in the periorbital fatty region of the eye.

7.3 Running the Code for the Thermal Modelling

The corner nodal points for the rectangular and triangular elements in Figure 3-2 were calculated by hand in square units and then a preprocessing program calculated the interior nodes and then all the nodes were mapped onto a x, y coordinate system. The preprocessor also allowed for node

numbers that were inadvertently left out. The preprocessor also typed out the nodal coordinates into a form that could be incorporated into a datadeck which then was used as input data by the finite element code, PARAB, which was developed by H. J. Chang and L. J. Hayes [77]. The code PARAB is used to solve two-dimensional, linear, scalar, parabolic boundary value problems such as the bioheat transfer equation. PARAB uses isoparametric elements; a backward time-selecting method was selected in all studies. A representative copy of the datadeck for this code is given in Appendix A. The datadeck in Appendix A is for SAR heating and normal perfusion rates and $h = .001 \text{ W/cm}^2\text{-C}$. A users guide for the PARAB program was published by L. J. Hayes [79]. Several changes were made to the code namely; the code was made axisymmetric, the subroutine SRHSD was modified to allow for heating via SAR patterns or electrical field equations, and subroutine UINIT was modified to generate an initial temperature gradient. Subroutine SRHSD which calculates the forcing function from either SAR patterns or electrical field equations is given in Appendices B and C.

The code was run on the CDC 7600 computer and accessed through the VERSATERM-PRO communications package. After the code was run, the output data, TAPE7, was sent to a post processor so the data could be arranged for display via a contouring package. The contouring package, FIDAP, is a commercial code developed by Fluid Dynamics International [80]. This code allows for the data to be plotted as isotherm regions. In order to run the file BCONT which is the compiled version of FIDAP, TAPE7 must be in the filespace and a data deck must be created for the contouring package.

7.4 Transient two-dimensional axisymmetric model of the eye using electromagnetic power absorption as a forcing function

The final stage of developing a model to predict heating within the eye due to microwave exposure incorporates a forcing function that is dependent on the frequency and electrical properties of the tissue. Equation (2-10) which is solved using the finite element grid shown in Figure 3-7. The thermal properties of Table 2-1, perfusion rates from Table 2-2 and the electrical properties from Tables 2-3 and 2-4 have been used. Several improvements over the previous SAR forcing function model have been implemented due to knowledge gained from the experimental data. First, an initial condition temperature gradient along the center line of the eye has been implemented that increases linearly from 32 C at the apex of the cornea to 37 C at 11.65 mm in the eye. All of the temperatures along a horizontal line within the eye grid are at the same initial temperature. Second, the boundary condition at the surface of the eye was increased to .01 from .001 W/cm² C. This simulated the experimental conditions since the eye moisturizing solution that was dropped onto the cornea every 90 seconds collected within the eye speculum that kept the eye open during exposure. Also, the boundary conditions at the front of the eye were calculated by experimentally measuring power density in W/cm² before each exposure and using equation 2-8 to evaluate the electrical field intensity, E (V/cm), for that particular interface. Third, the boundary condition posterior to the choroid was changed from a Dirichlet boundary condition at 34 C to a no flow condition since anatomically there is a large layer of fat and experimental data showed that temperatures posterior to the lens were increasing significantly, Figures 7.1 and 7.2. Four, the heat

generation term was calculated from the electrical field equations for each tissue rather than extrapolated from the SAR function along the center of the eye.

7.5 Depth of Penetration

Since tissue exposed to a RFR can be represented as a lossy dielectrics the decay of power in a volumetric since may be written as in equation 2-9 as:

$$P_{z,vol} = (|E_{x0}|^2 \alpha e^{-2\alpha z} / \eta_m) \cos(\theta_\eta)$$

As the power is dissipated through the media. The amplitude will be attenuated by a factor of $e^{-2\alpha z}$. Over a distance of

$$\delta = 1/2\alpha \quad (7-1)$$

where,

$$\alpha = \omega(\mu\epsilon)^{1/2} \{ [1 + (\sigma/\omega\epsilon)^2]^{1/2} - 1 \}^{1/2} \quad (7-2)$$

The magnitude of the wave will be reduced by $1/e$, or 37 percent. The quantity δ is termed the depth of penetration, of the tissue [46]. The term α is proportional to ω ; thus, causing a decrease in the penetration depth. The conductivity and the permittivity are also dependent on the frequency. For biological tissues the conductivity tends to decrease with frequency and the permittivity tends to increase causing a further decrease in the penetration depth. Figure 7.3 shows the relationship of the rate of heat generation for the lens nucleus and fat at 2.45 GHz at an irradiance of 125 mW/cm² calculated from the electrical field equations and heat generation at the same frequency

calculated from the SAR function. In this final version of the model, the electrical properties of the aqueous humor and vitreous humor were assumed to be similar to that of the lens nucleus.

Note that the attenuation of the power is greater in the fat than in the eye tissue. Figure 7.4 shows the same relationship at 35 GHz and 125 mW/cm². Note that there is an even greater attenuation of both the fat and eye tissue but now the heat generation within the fat is greater than that in the eye tissue. The depth of penetration for fat at 2.45 GHz is 5.94 mm but due to its characteristic high impedance, η_m , of 167.6 Ohms and its relatively low α the power delivered is much less. Table 7-3 gives the characteristic impedance, attenuation constant and phase angle calculations for 2.45 GHz and 35 GHz. Therefore, at 2.45 GHz heating within the eye tissue itself is the primary contributor to the thermal contours, while at 35 GHz heating within the surrounding tissue, fat primarily, is the primary contributor to the thermal patterns.

Table 7.1
Attenuation Constant, Characteristic Impedance, and Phase Angle at 2.45 GHz
and 35 GHz

Tissue	$\alpha(1/\text{mm})$	$\eta_m(\text{Ohms})$	$\cos\theta_\eta$
Fat @ 2.45 GHz	0.084	167.6	.997
Fat @ 35 GHz	2.634	191.8	.991
Eye tissue @ 2.45 GHz	0.375	67.6	.990
Eye tissue @ 35 GHz	9.945	106.2	.922

7.6 Computer Runs Using the Electrical Field as a Forcing Function

First the model using the electrical field as the forcing function was compared to the model using SAR forcing functions. Figure 7.5 shows the temperature contours via electrical field equations when the new boundary conditions and temperature gradients were implemented for a frequency of 2.45 GHz and an irradiation of 125 mW/cm^2 for 2400 seconds with normal perfusion rates. Figure 7.6 shows the temperature contours via SAR patterns for the same conditions. Both contours show a peak temperature within the vitreous humor and the same trends in isotherm contours, but the SAR generated contours tend to be several degrees higher in the vitreous humor. This can be attributed to the same SAR forcing function for the center of the eye being applied for the fat and muscle which has been shown in Figure 5-1 not to be the case.

Since increased blood perfusion is expected, a run was made with ten times the normal perfusion rate. Figure 7.7 shows the results, the higher perfusion rates cause the isotherms to be more conformed to the circular shape of the choroid. Also, fat is a good thermal insulator so heat is not readily conducted away from the eyeball where greater heat is being generated.

Next, a run at 35 GHz was made with ten times the normal perfusion rate. The isotherms temperatures in Figure 7.8 tend to be much greater in the fat region at the upper boundary. This is due to the higher heat generation term for fat at this frequency shown in Figure 7.4. The contours in Figure 7.8 predict very similar heating for the eyeball and surrounding tissue beyond the lens. This correlates well to experimental data Figure 7.2. Also, the thermal

characteristics, good insulation, of the lens are shown since heat that is being convected off the surface of the eye is slowed at the lens. The peak contours, 40.0 C, along the axis of the eye occur in the lens. The fat closest to the surface generates heat and then the heat is conducted from the fat to the aqueous humor and then it is convected off the surface of the eye. Similar contours at much higher temperatures were obtained with normal perfusion rates. Figure 7.9 shows the results, once again the highest temperatures occur along the axis of the eye occur within the lens.

Next several runs at 35 GHz and 125 mW/cm² were made to give a temperature versus time relationship for a node which corresponds to the placement of the thermistor probe in the vitreous humor during 35 GHz and 125 mW/cm². These runs were made at 0, 1, and 10 times the normal perfusion rate. Figure 7.9 shows the results of these runs. The no perfusion case has very high heating at a fast rate. This is to be expected since the only mechanisms to remove heat are the convective surface of the eye and surrounding tissue. The high perfusion rate condition went to a steady state value at 38.5 C within a few minutes after exposure. The normal perfusion case tends to go to a temperature of 44.0 C after 2400 seconds. This correlates well to the experimental data where the vitreous humor went to a temperature of 39.5 C after 2400 seconds. The discrepancies in temperatures at this time may be due to an increase in perfusion but not as great as 10 times.

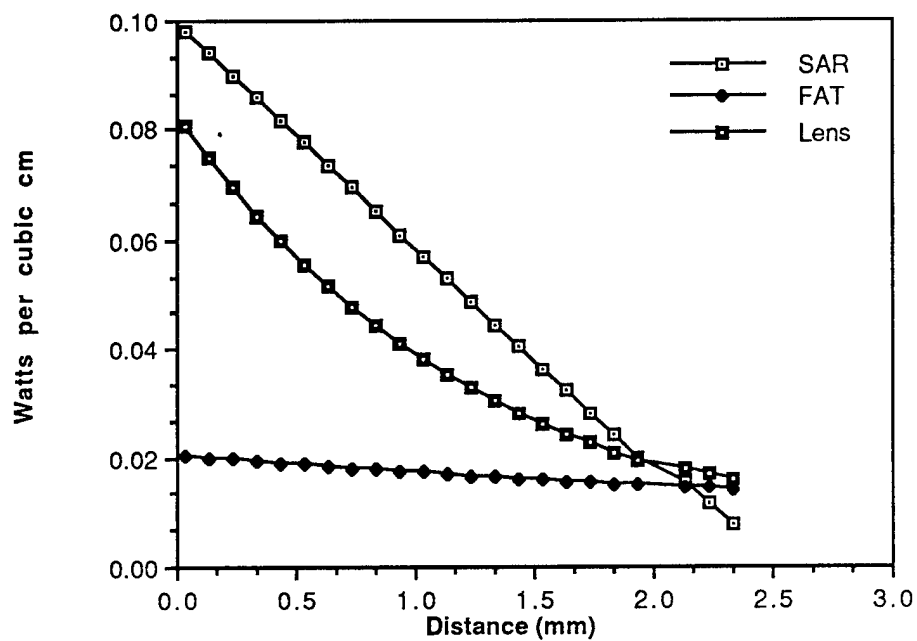


Figure 7.3 Calculated heat generation for the lens nucleus and fat at 2.45 GHz and experimental measured heat generation (SAR).

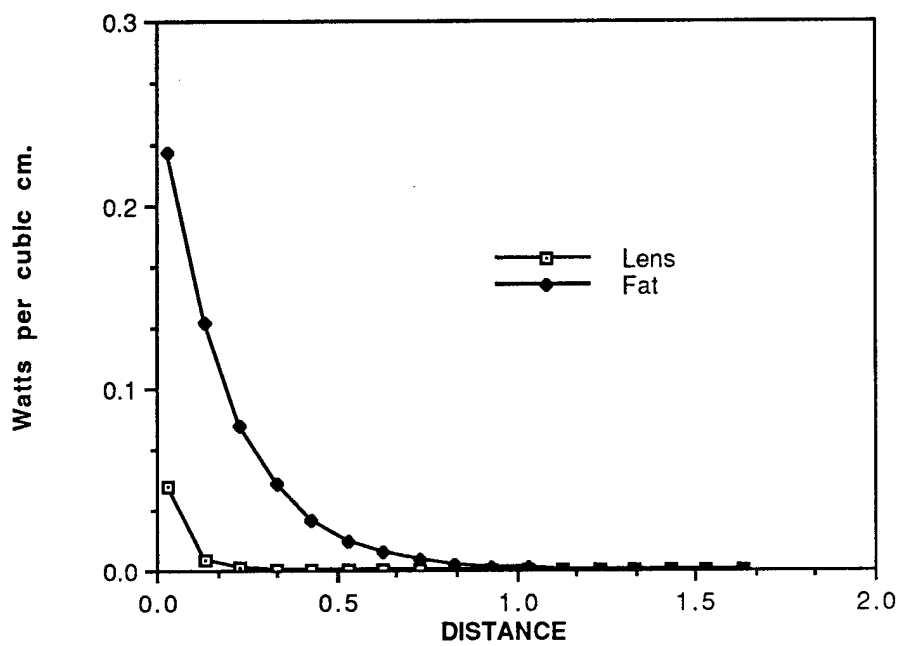


Figure 7.4 Calculated heat generation at 35 GHz and 125 mW/cm sq.

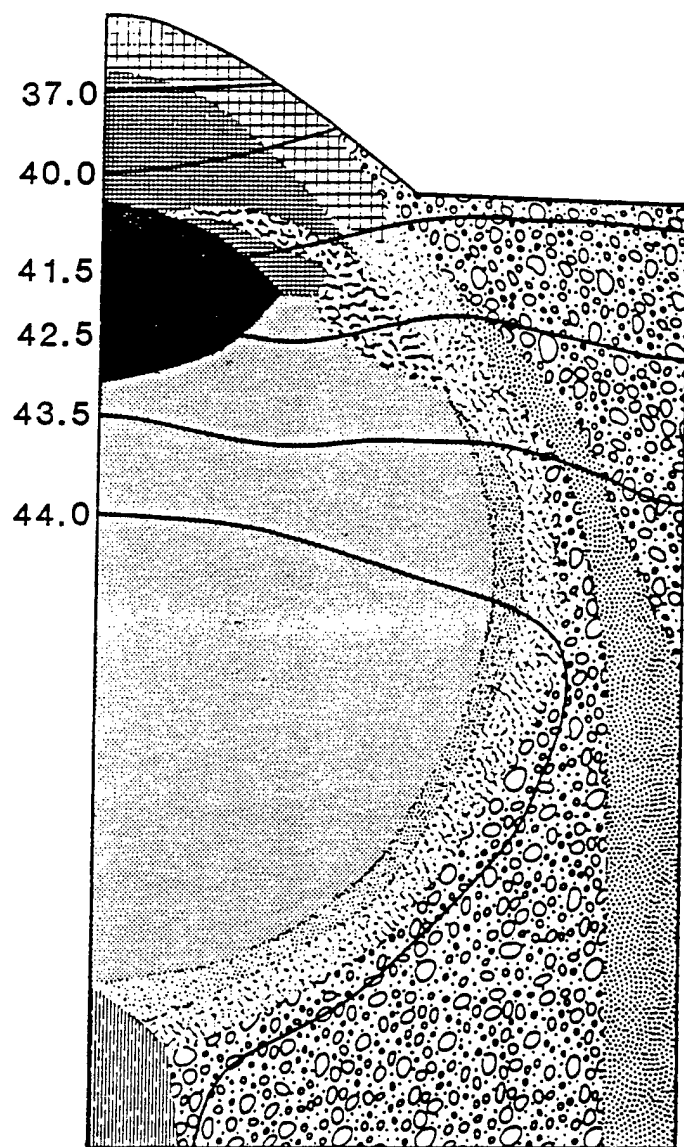


Figure 7.5 Computed temperature contours for the eye exposed to 2.45 GHz (power density of 125 mW/cm^2) for 2400 sec using electrical field equations as forcing function.

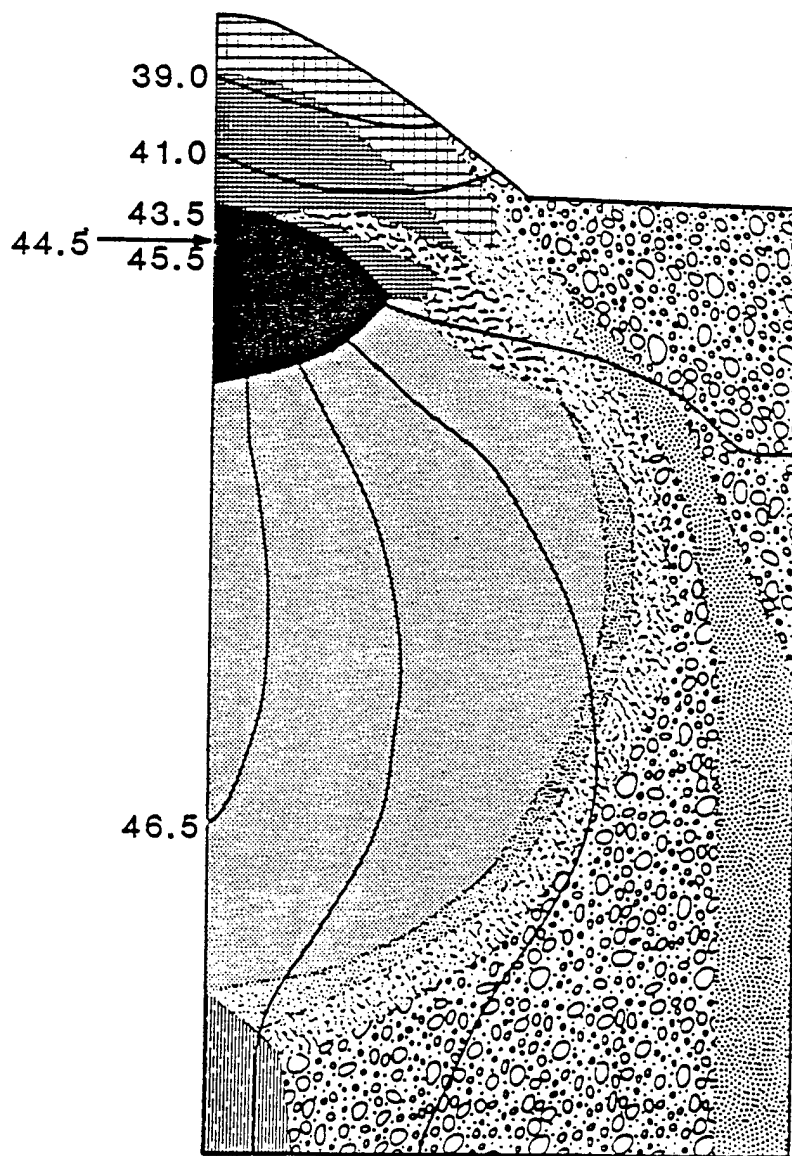


Figure 7.6 Computed temperature contours for the eye exposed to 2.45 GHz (power density of 125 mW/cm^2) for 2400 sec using SAR pattern as forcing function.

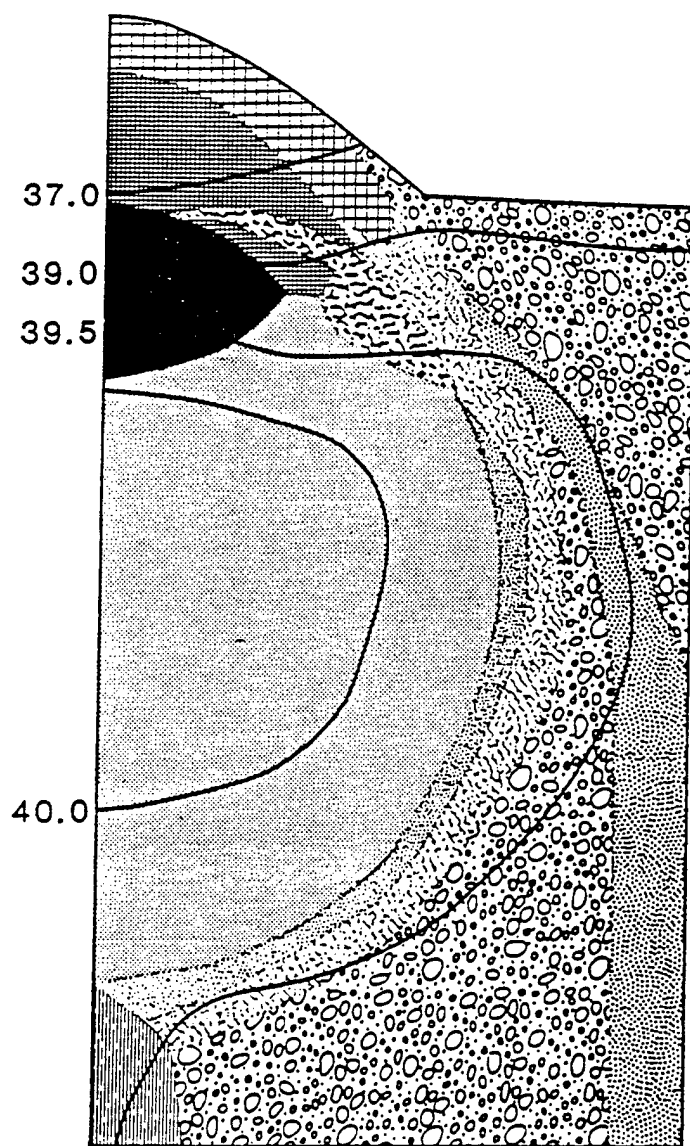


Figure 7.7 Computed temperature contours for the eye exposed to 2.45 GHz (power density of 125 mW/cm^2) for 2400 sec assuming 10 times normal perfusion.

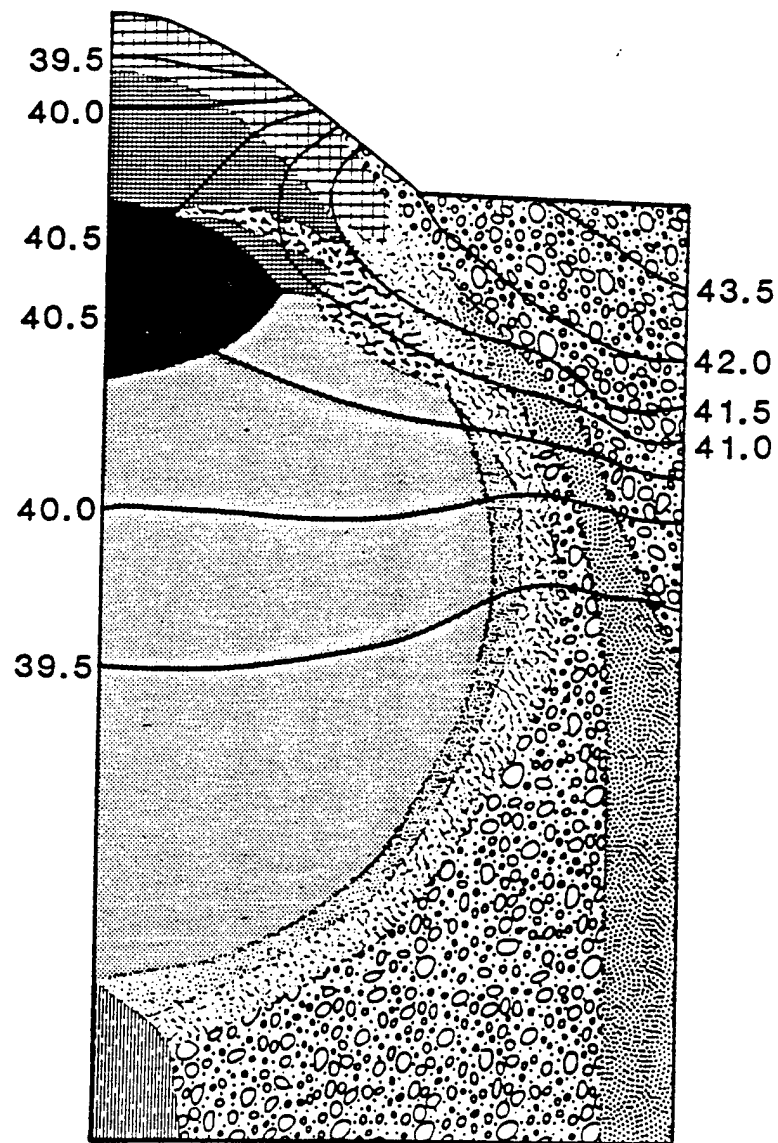


Figure 7.8 Computed temperature contours for the eye exposed to 35 GHz (power density of 125 mW/cm^2) for 2400 sec assuming 10 times normal perfusion.

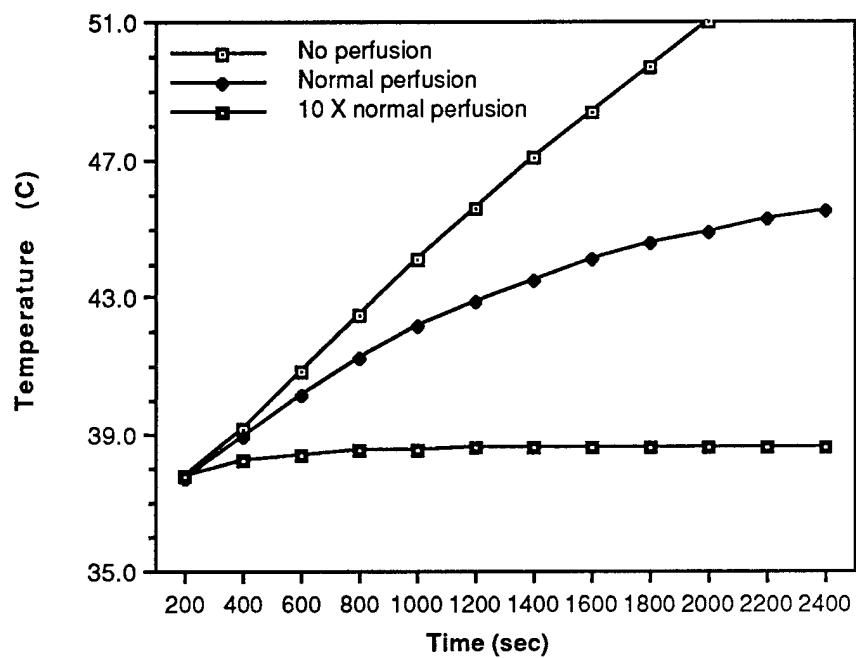


Figure 7.9 Temperature history for node 298 within periorbital fat. (35 GHz and 125 mW per sq cm)

EXPERIMENTAL RESULTS OF CHRONIC EXPOSURE TO 10 AND 100mW/cm² OVER a TWO-WEEK PERIOD OF TIME

The purpose of this research was to determine the injury threshold of the cat's corneal endothelium to 35 GHz microwave radiation. Injury threshold was defined as a statistically significant increase in mean corneal endothelial cell area compared with a non-irradiated, sham-exposed control.

Method

Experiments were conducted at two exposure levels at the microwave radiation facilities of BASM. Exposure levels were measured and adjusted using dosimetry at the eye. The first series of four cats were each exposed two hours/day on alternate days over a period of two weeks for a total of six exposures /cat (12 hours total exposure/cat) to 100 mW/cm², 35 GHz radiation. The second series of four cats were each exposed to 10 mW/cm² radiation two hours/day on alternate days over a period of two weeks for a total of six exposures/cat (12 hours total exposure/cat). Four cats had previously been studied under identical experimental conditions (except no microwave radiation) at U.T. Austin and were used as controls.

Cats were given a preanesthetic Ketamine at a dose of 20 mg/kg and then were given an anesthetic, Xylazine, at a dose of 1 mg/kg, (this dose keeps the animals under for a period of two hours) and placed in a head clamp positioned in front of the non-contact specular microscope. A plastic irrigating eyelid speculum exposed the cornea and maintained an adequate tear film throughout the experiment. The slit lamp was modified with a remote controller that allowed horizontal position and focus control outside the irradiation facility.

Analog video images were obtained from a DAGE model CCD71 camera attached to a TOPCON SL-6E slit-lamp microscope with a non-contact specular lens. Continuous low illumination from the slit lamp allowed the observer to remotely focus the system to obtain a clear image of the corneal endothelium on the video monitor outside the radiation facility. User selected frames from the video camera were digitized on-line using a METRABYTE MV-1 frame-grabber board interfaced with an IBM PC-AT. The slit-lamp strobe light synchronized with the vertical sync. of the camera was used to reduce motion artifact in the digitized frames. One frame was recorded each 30 minutes during the 2 hour exposure session for a total of at least 4 frames/exposure session. The images were stored on floppy discs with identification labels and returned to U.T. Austin for analysis.

The digital images were of insufficient quality to obtain cell boundaries by simple thresholding so the following sequence of image processing techniques were applied. The operator first chose a window subset of the full frame that contained the cellular information relevant to the analysis. Next, a linear gray level operator was applied to the selected window to compensate for the gray level variation inherent in the slit beam. Intracellular granularity was removed by applying a medium filter of size (3x3). Next, a circularly symmetric Gaussian filter was used to blur cell detail smaller than the boundaries, and the resulting image was then convolved with a (3x3) Laplacian template (which is a differential operator) to enhance edges. The resulting image was rendered binary by setting all positive pixels equal to one and all negative pixels equal to zero. The resulting image did not contain well-defined boundaries but it did indicate the cell centers. At this point the number of cells/unit area could be determined, but little morphological detail was present. To enhance boundary information and reduce noise, the signal

content in the Laplacian of the Gaussian image (LOG) was scaled between 0 and 255 to enhance contrast. A gray level threshold was then applied to the resulting image to obtain a binary image with the cell centers equal to one and the boundaries equal to zero. The boundaries were thick in the resulting binary image (BIN) but the centers of the cells were well defined.

Blob coloring was then used to count the number of cells in the image. In this case, the colors were numbers from 0 to N, where N is the number of cells contained in the image. While the blob coloring algorithm counted the blobs, it also counted how many pixels formed each blob. The resulting output was the array $\text{Count}(i,j)$ = number of pixels in the center of each cell and $\text{Temp}(i,j)$ = numbered centers of the cells.

The boundaries were then thinned using a contour following, region growing algorithm which dilated the individual cell centers while preserving the individual cell shapes. A 5×5 template in the shape of a cross was convolved with the binary image (BIN) to grow the cell centers recursively until they reach the limiting criterion. The limiting criterion was that if a pixel was already a neighbor of some other object, then it was not incorporated as part of the object being dilated but rather assigned as a boundary between the two objects. Once the dilation was complete, the number of pixels inside each boundary was computed by adding the number of dilation pixels to the number of center pixels ($\text{Count}(i,j)$). Those cells which touched the edges of the selected window were discarded because they were incomplete cells. The location in the array $\text{Count}(i,j)$ where the incomplete cell was stored was set to zero and this cell was excluded from any further analysis.

Finally, the completed boundaries were overlaid on the original image for the user to edit for any incomplete or duplicated cells. These errors

usually occurred because two cell centers incorrectly connected together in the BIN image were dilated into one erroneously big cell instead of the original two cells. The editing process consisted of drawing with the mouse (or other input device) boundaries where they were missing and elimination of any false boundaries. The arrays Count (i,j) and Temp (i,j) were then corrected for the final edited image. The following cell statistics were then displayed: mean cell area, standard deviation of mean cells area, number of cells/unit area, and and the cell distribution function.

At least 100 cells were measured for each animal at each exposure-recording session. Images were generally of highest quality at the beginning of the exposure session and became blurred as the session continued due to superficial epithelial keratitis induced by the lack of blinking and the radiation itself.

Results

A typical cell area distribution function is shown in figure 8.1. The distribution is sufficiently normal to allow a comparison of means to test the hypothesis that damage occurred.

Graphs of mean cell area bounded by one standard deviation are shown in figures 8.2 for the 100 mW/cm² exposures and in figures 8.3 for the 10 mW/cm² exposures. A typical control measurement is shown in figure 8.4.

Discussion

None of the exposures resulted in an increase in mean cell area. Therefore, the damage threshold (as defined for this research) was not determined but is presumably greater than 100 mW/cm². Future

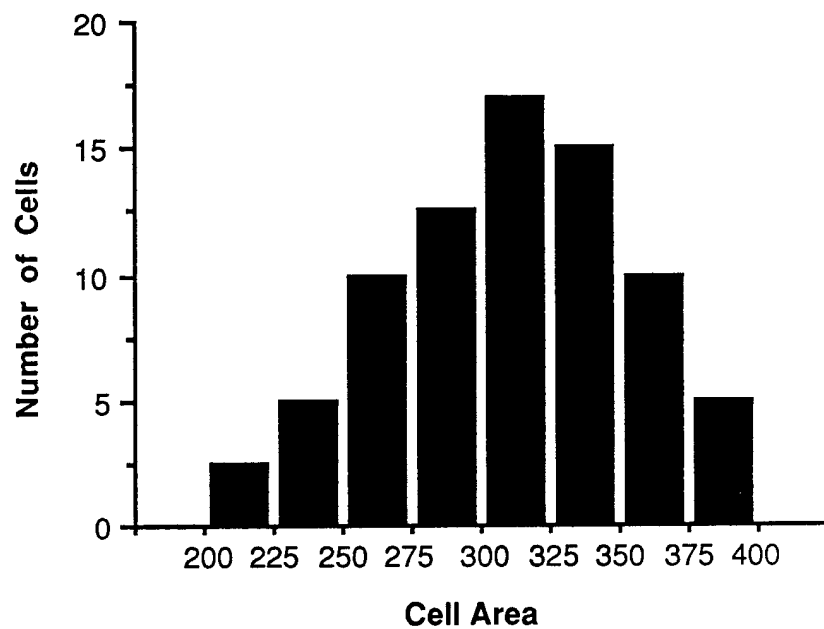


Figure 1: Typical Mean Cell Area Distribution Factor

10 mW/cm² Exposure

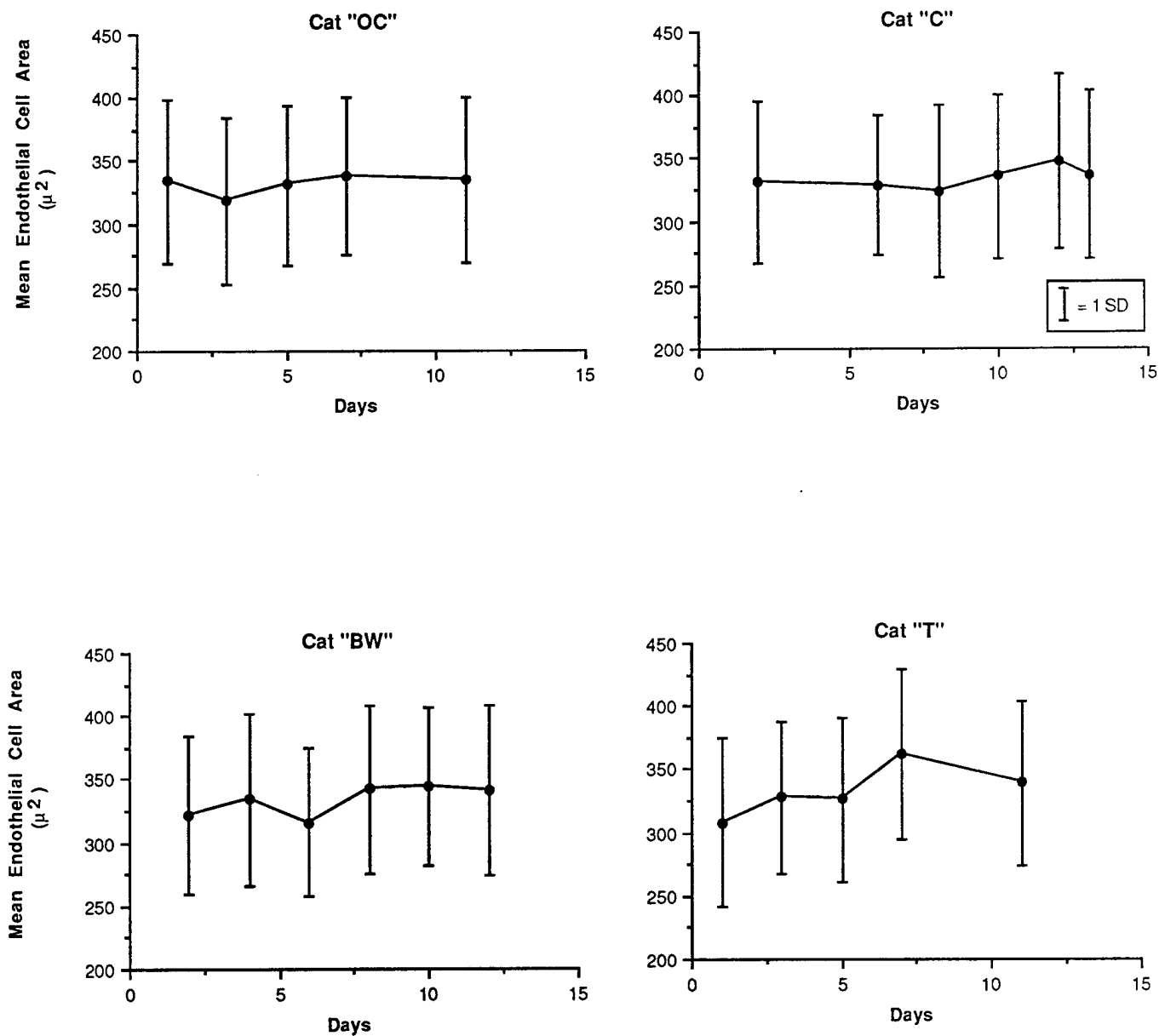


Figure 2: Mean Cell Area For 10 Mw/Cm² Exposure

100 mW/cm² Exposure

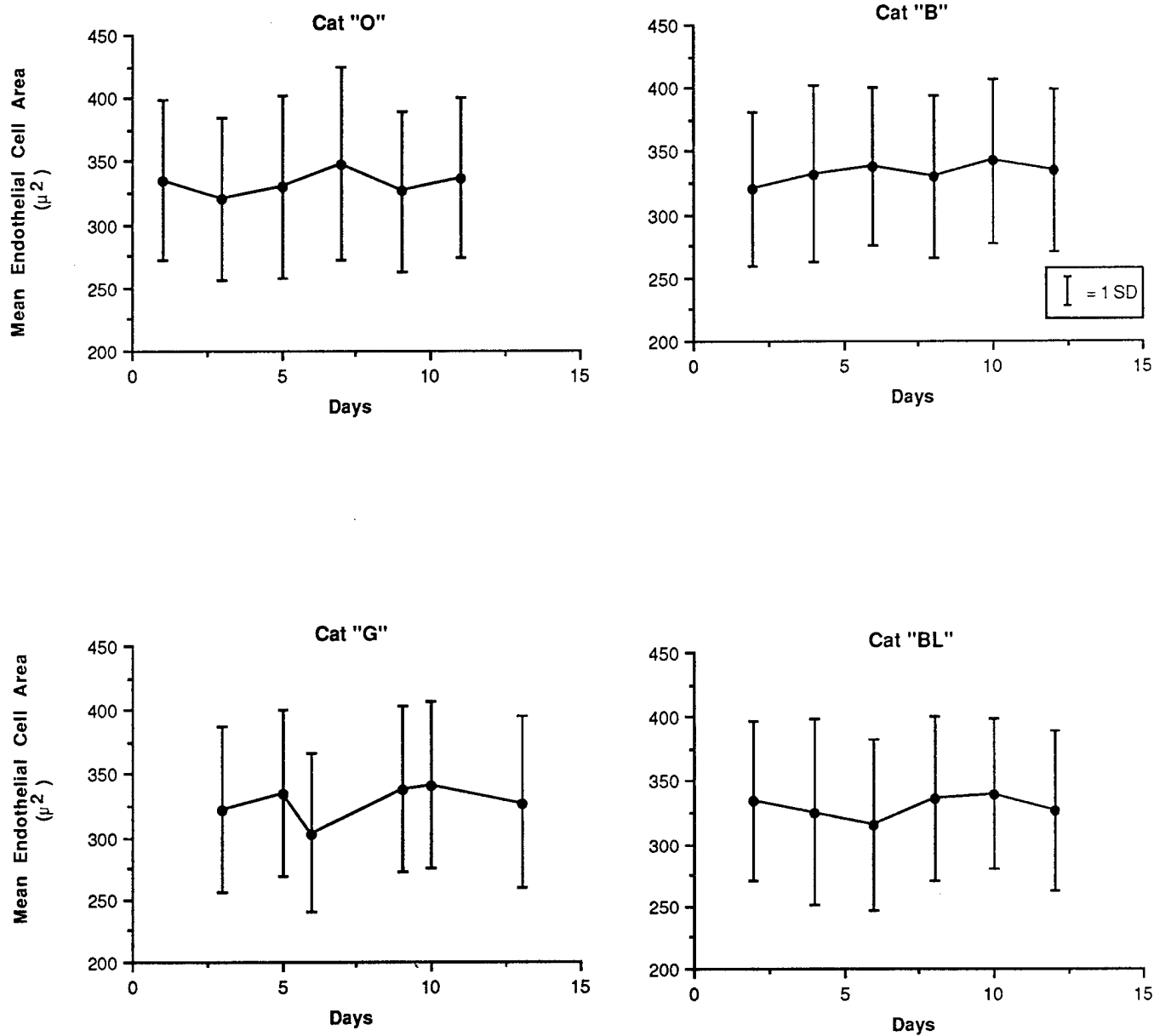


Figure 3: Mean Cell Area For 100 Mw/Cm² Exposure

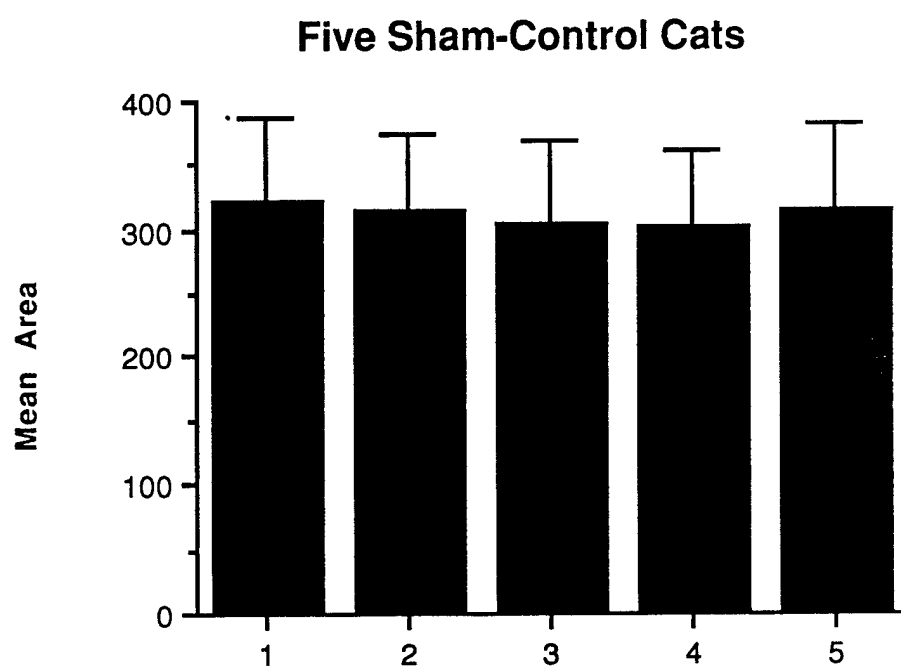


Figure 4: Control Measurement

experiments will require a lens to focus the radiation on the eye to achieve levels of 200 to 500 mW/cm².

Some of the final images of cats exposed at 100 mW/cm² showed occasional missing cells and some guttata, but the effect was not large enough to result in generalized cell hypertrophy and the corneas remained clear.

A technique for detecting missing and damaged cells is being evaluated and may provide a more sensitive measure of the earliest possible radiation effect than the measurement of mean cell area. Mean cell area is still the most important measurement of the integrity of the corneal endothelium and its ability to dehydrate the corneal stroma.

Conclusions

The cat's corneal endothelium is not significantly damaged by 12 hours of exposure to 30 GHz microwave radiation at levels below 100 mW/cm².

REFERENCES

1. Barnes, F.S. and Hu, C.-L.J., "Model for Some Nonthermal Effects of Radio and Microwave Fields on Biological Membranes," IEEE Trans. Microwave Theory Tech., Vol. 3, No. 2, 1977, pp. 193-201.
2. Carpenter, R. L. and Van Ummersen, C. A., "The Action of Microwave Radiation on the Eye," Journal Microwave Power, Vol. 3, 1968, pp. 3-19.
3. Cleary, S. F., "Microwave Cataractogenesis," Proc. IEEE, Vol. 68, 1980, pp. 49-55.
7. Heynick, L. N. ,(1987). Critique of the Literature on Bioeffects of Radiofrequency Radiation: A Comprehensive Review Pertinent to Air Force Operations. USAFSAM-TR-87-3 pp. 18-21.
8. Guy, A.W. "Analyses of Electromagnetic Fields Induced in Biological Tissues By thermographic Studies on Equivalent Phantom Models," IEEE Trans. Microwave Theory Tech., Vol. 19, 1971, pp. 205-214.
9. Johnson, C.C., A. W. Guy, (1972). Nonionizing electromagnetic wave effects in biological materials and systems. Proc. IEEE, 60:692-718.
10. Durney, C.H., C. C. Johnson, P. W. Barber, H. Massoudi, M. F. Iskander, J. L. Lords, D. K. Hyser, S. J. Allen, J. C. Mitchell, (1978). Radiofrequency Radiation Dosimetry Handbook (2nd Ed.) SAM-TR-78-22, Brooks AFB, Texas.
11. Richardson, A.W., T. Duane, H. Hines, (1948). Experimental lenticular opacities produced by microwave radiations. Arch. Phys. Med. 765-769, Dec., 1948.
12. Daily, L.,D. Wakim, J. Herrick, E. Parkhill, W. Benedict, (1950). The effects of microwave diathermy on the eye. Amer. J. Ophthal. 33:1241-1254.
13. Daily, L.,D. Wakim, J. Herrick, E. Parkhill, W. Benedict, (1952). The effects of microwave diathermy on the eye. Amer. J. Ophthal. 35:1001-1017.
14. Williams, D.B., J.P. Monahan, W.J. Nicholson, J. J. Aldrich, (1956). Time and power thresholds for the production of lens opacities by 12.3 cm microwaves. IRE Trans. Bio-Med. Electron. 4:17-22.
18. Guy, A.W., P.O. Kramar, A. F. Emery, J.C. Lin, (1975). Effect of 2450-MHz radiation on the rabbit eye. IEEE trans. MTT 23:492-498.

* = Not Referenced in Text

19. Kramar, P., C. Harris, A. Emery, A. W. Guy, (1978). Acute Microwave Irradiation and Cataract Formation In Rabbits and Monkeys. J. Microwave Power. 13:239-249
20. O'Day, D. M., M.b. Fish, S. B. Aronson, M. Pollycone, A. Coon, (1971). Ocular perfusion measurments by nuclide labelled microsperes. Arch. Ophthal. 86:205-209.
21. White, T. J., M. A. Mainster, J. H. Tips, P. W. Wilson, (1970). Chorioretinal thermal effects. Bull. Math. Biophys. 32:315-322.
22. McAfee, R. D., A. Longacre, R. R. Bishop., S. T. Elder, J. G. May, M. G. Holland, R. Gordon (1979). Absence of ocular Pathology After Repeated Expsure of Unanesthetized Monkeys to 9.3-GHz Microwaves. J. Microwave Power, 14:41-44.
23. Appleton, B., S. E. Hirsch, P. V. K. Brown, (1975). Investigation of single-exposure microwave ocular effects at 3000 MHz. Ann. N.Y. Acad. Sci. 247:125-132.
24. Guy, A. W., P. O. Kramar, C. A. Harris, C. K. Chou, (1980). Long-term 2450-MHz CW Microwave Irradiation of Rabbits: Methodology and Evaluation of Ocular and Physiologic Effects. J. Microwave Power. 15:37-44.
25. Appleton, B. (1973). Experimental microwave ocular effects. In Biologic Effects and Health Hazards of Microwave Radiation, Proc. of an International Symp., Warsaw, October 15-18, Polish Medical Publishers, Warsaw, 1973, pp. 186-188.
4. Kues, H.A., L.W. Hirst, G.A. Lutty, S. A. D'Anna, G. R. Dunkelberger (1985). Effects of 2.45-GHz Microwaves on Primate Corneal Endothelium, Bioelectromagnetics 6:177-188.
26. Rao, G. N., E. L. Show, E. J. Arthur, J.V., (1979). Endothelial Cell Morphology and Corneal Deturgescence, Am. Ophthalmology, 1:885-889.
27. Kadry, A. A., A. A. Youssef, (1975). Biological Thermal Effects of Microwave Radiation on Human Eyes, Biological Effects of Electromagnetic Waves USNC/URSI Annual Meeting.
28. Hirsh, F.G., J. T. Parker, (1952). Bilateral Lenticular Opacities Occurring in a Technician Operating A Microwave Generator. AMA Arch. Ind. Hyg. Occup. Med., 6:512-517.

29. Zaret, M. (1969). Ophthalmic Hazard of Microwave and Laser Environments. 39th Ann. Sci. Meeting Aerosapce Med. Assoc., San Francisco, CA.
30. Issel, I., P. Emmerlich, (1981). Lens Clouding as a Result of The Effectrs of Microwaves. (Engl. Trans. of Linsenttruebun nfolge Micrwelleneinwirkung) Deutsche Gesundheitswesen, 36(18):17-19.
31. Pennes, H.H. "Analysis of Tissue and Arterial Blood Temperatures in the Resting Human Forearm". J. Appl. Physiol. 1(1948),93-122.
39. Hales, J.R., Fawcett, A.A., Bennett, J.W. and Needha, A.D., "Thermal Control of Blood Flow Through Capillaries and Arteriovenous Anastomoses in Skin of Sheep," Pflugers Arch., Vol. 378, 1978, pp. 55-63.
40. Tortora, G.J., Principles of Human Anatomy,3rd ed., Harper & Row, New York, 1983.
41. Dudar, T.E., and Jain, R.K. "Differential REsponse of Normal and Tumor Microcirculation to Hyperthermia". Cancer Res. 44 (1984), 605-612.
36. O'Day, D.M., Fish, M.B., Aronson, S.B., Pollycone, M., Coon, A., "Ocular Perfusion Measurements by Nuclide Labelled Microspheres," Arch. Ophthal. Vol. 86, No. 2,1971, pp.205-209.
37. Rudolph, A.M. and Heymann, M.A., "Circulation of the Fetus in Utero: Methods for Studying Distribution of Cardiac Output and Organ Blood Flow," Circ. Res., Vol. 21, 1967, pp. 163.
32. Mitchell, J.W., Galvez, T., Hengle, J., Myers, G.E. and Siebecker, K., "Thermal Response of Human Legs During Cooling," J. Appl. Physiol., Vol. 29, 1970, pp. 859-865.
33. Sekings, K.M., "Microwave Hyperthermia in Human Muscle: An Experimental and Numerical Investigation of the Temperature and Blood Flow Fields Occurring During 915 MHz Diathermy," Ph.D. Dissertation, University of Washington, 1981.
34. Kramar, J.C., Harris, C., Emery, A.F. and Guy, A.W., "Acute Microwave Irradiation and Cataract Formation in Rabbits and Monkeys," Journal of Microwave Power, Vol. 13, 1978, pp. 3.3.
35. Bowman, H.F., Cravalho, E.G. and Woods, M., "Theory, Measurement, and Application of Thermal Properties to Biomaterials," Ann. Rev. Biophys. Bioeng., Vol. 4, 1975, pp. 43-80.

5. Paulsson, L.E., Hamnerius, Y., Hansson, H.A. and Sjostrand, J., "Retinal Damage Experimentally Induced by Microwave Radiation at 55 mW/cm²," Acta Ophthalmol, Vol. 57, 1970, pp. 183-197.
6. Frei, M., J. Jauchem, F. Heinmets, (1988). Physiological effects of 2.8 GHz Radio-Frequency Radiation: A Comparison of Pulsed and Continuous Wave Radiation., J. Microwave Power. 23:85-93.
43. Dawkins, G., "Hyperthermi Dough: a Fat and Bone Equivalent Phantom t test Microwave/Radiofrequency Hyperthermia Heating Systems". Phys. Med. Biol., 1985, Vol. 30, No 7, 789-712.
44. Hurt, W.D., "Multiterm Debye Dispersion Relationf for Permittivity; of Muscle". IEEE Biomed. Eng., 1985, Vol. BME-32, No.1, 60-64.
45. Steel, M.C., Sheppard, R.J., "The Dielectric Properties of Rabbit Tissue, Pure Water and Various Liquids suitable for Tissue Phantoms at 35 GHz". Phys. Med. Biol., 1988, Vol. 33, No 4, 467-472.
46. Hyat, W.H., Engineering Electromagnetics, Mcgraw-Hill Inc., 1967, 333-342.
- * Becker, E.B., Carey, G.F., Oden, J.T., Finite Elements an Introduction, Vol. 1, Prentice-Hall, 1981.
72. Schwartz, B. and Feller, M.R., "Temperature Gradients in the Rabbit Eye," Invest. Ophth, Vol. 4, 1962, pp. 513-521.
79. Hayes, L.J, Chang, H. J., A users Gude to Parab - A Two-Dimensinal Linear Time-Dependent Finite Element Program, Texeas Institute for Computational Mechanics Report 80-10. 1980.
80. FIDAP.
78. Ling, T., Vannas, A., Holden, B.A., "Long-Term Changes in Corneal Endothelial Morphology Following Wounding in the Cat," Invest. Ophth. Vis. Sci., Vol. 29, No. 9., 1988. 1407-1412.
15. Carpenter,R., C. Van Ummersen, (1968). The action of microwave power on the eye. J. Microwave Power. 3:3-19.
16. Carpenter, R., E. S. Ferri, G. J. Hagan, (1972). Lens opacities in eyes of rabbits following repeated daily erradiation at 2.45 GHz. Microwave Power Symposium, Ottawa, Canada, May 24,1972 (iMPI),p. 143.

17. Kramar, P., A. Emery, A. Guy, J. Lin, (1975). The ocular effects of microwaves on hypothermic rabbits and study of microwave cataractogenic mechanisms. *Ann. N.Y. Acad. Sci.* 247:155-165.
38. Emery. A.F., Sekins, K.M., "The Use of Heat Transfer Principles in Desinging Optimal Diathermy and Cancer Treatment Modalities," *Int. J. Heat Mass Transfer.* Vol. 25, No.6, 823-834, 1982.
47. Ganong W.F.. Review of Medical Physiology. Englewood Cliffs, NJ: Prentice Hall, 1987.
48. Newell F.W. Ophthalmology: Principles and Concepts. St. Louis, MO: The C.V. Mosby Company, 1982.
50. Davson H. The Physiology of the Eye. New York: Academic Press, 1972.
49. Waring, III G.O., Bourne W.M., Edelhauser H.F., Kenyon K.R.: The corneal endothelium, normal and pathologic structure and function.
51. Binder PS, Akers P, Zavala EY: Endothelial Cell Density determined by specular microscopy in scanning electron microscopy. Ophthalmology, 86:1831-1847, 1979.
56. Waring III GO, Krohn MA, Ford GE, Harris RR, Rosenblatt LS: Four methods of measuring human corneal endothelial cells from specular photomicrographs. Archives of Ophthalmology, 98:848-855, 1980.
57. Rouhiainen H, Kemppinen P: Corneal endothelial cell density after trabeculoplasty. Ophthalmologica, 196:182-184, 1988.
52. Bourne WM, Kaufman HE: Specular microscopy of human corneal endothelium in vivo. American Journal of Ophthalmology, 81:319-323, 1976.
70. Geroski DH, Edelhauser HF: Morphometric analysis of the corneal endothelium. Investigative Ophthalmology & Visual Science, Vol 30, No 2:254-259, 1989.
71. Rao GN, Shaw El, Arthur EJ, Aquavella JV: Morphological appearance of the healing corneal endothelium. Archives of Ophthalmology, 96:2027-2030, 1978.
77. Mishima S: Clinical investigations on the corneal endothelium. American Journal of Ophthalmology. 93:1-15, 1982.
54. Maurice D.M.: Cellular membrane activity in the corneal endothelium of the intact eye. Experientia 24:1094, 1968.

55. Laing, R.A., Sandstrom, M.M., and Leibowitz, H.M.: In vivo photomicrograph of the corneal endothelium. Archives of Ophthalmology. 93:143,1975.
53. Laule A, Cable MK, Hoffman CE, Hanna C: Endothelial cell population changes of human corneal during life. Archives of Ophthalmology, 96:2031-2039 1978.
- * D.H. Ballard, C.M. Brown, Computer Vision. Englewood Cliffs, NJ: Prentice Hall, 1982.
- * A. Rosenfeld and A.C. Kak, Digital Picture Processing, Volume 2. Orlando, Fla: Academic Press, Inc.,1982.
- * A.C. Bovik, T.S. Huang, and D.C. Munson, Jr.: The Effect of Median Filtering on Edge Estimation and Detection, IEE Transactions on Pattern Analysis and Machine Intelligence, Vol. PAMI-9, N0. 2: 181-194, 1987.
- * N.H. Kim, A.B. Wysocki, A.C. Bovik, and K.R. Diller: A Microcomputer-Based Vision System for Area Measurement. Comput. Biol. Med. Vol 17, No. 3: 173-183, 1987.
- * J.D. Foley and D. Van Dam, Fundamentals of Interactive Computer Graphics. Addison Wesley,pp. 433-436, 1984.
65. D. Marr, Vision. New York: W.H. Freeman and Company, 1982.
58. Sun, Y.: Automated identification of vessel contours in coronary arteriograms by an adaptive tracking algorithm. IEEE Transactions on Medical, Imaging, Vol 8 No 1:78, 1989.
59. Yokoyama K., Ishii N., and Naka K.: Software system for neuron classification based on simple parameters. IEEE Transactions on Biomedical Engineering, Vol. BME-33, No. 3:308-313, 1986.
60. Diller, K.R., and Knox, J.M.: Identification and tracking of blurred boundaries in cluttered pictures. Proceedings, Pattern Recognition and Image Processing, IEEE Press, 137-139, 1981.
61. Frei W., Chen C.C.: Fast boundary detection: A generalization and a new algorithm. IEEE Transactions on Computers, Vol. c-26, 10:988-998, 1977.
67. Brenner JF, Gelsema ES, Necheles TF, Neurath PW, Selles WD, and Vastola E: Automated classification of normal and abnormal leukocytes. Journal Histochem. Cytochem, 22:697-706, 1974.

68. Image Analysis Systems: Reconstruction of grains and cell structures. Kontron Electronic Group.

69. Quantex OX-7 Image processing and analysis system. Quantex Corporation. Sunnyvale, California.

* Imagelab VGA. Werner Frei Associates. Venice, California.

62. Pfaltz, J.L., and Rosenfeld A.: Computer representation of planar regions by their skeletons.

63. Hawman E.G.: Digital boundary detection techniques for the analysis of gated cardiac scintigrams. SPIE Vol 206:224,233, 1979.

64. Chu C.H., Delp E.J., Duda A.J.: Detecting left ventricular and epicardial boundaries by digital two-dimensional echocardiography.

66. Yachida M, Ikeda M., and Tsuji S.: A plan-guided analysis of cineangiograms for measurement of dynamic behavior of heart wall. IEEE Transactions on Pattern Analysis and Machine Intelligence, Vol 2, No. 6:537-543, 1980.

* Yokoyama, K., Ishii N., Suzumura N., and Naka K.I.: Automatic classification of neurons. IEEE Transactions on Biomedical Engineering, Vol BME-33 No.3:308-313, 1986.

73. Ling et al.: Long-term changes in corneal endothelial morphology following wounding in the cat. Investigative Ophthalmology and Visual Science, 29: 1407-1412, 1988.

74. Minkowski et. al.: Corneal endothelial function and structure following cryo-injury in the rabbit. Investigative Ophthalmology and Visual Science, 25: 1416-1425, 1984.

75. Okihiro N, and Hanasaki K.: Automated determination of polygonality of corneal endothelial cells. Cornea, 8: 54-57, 1989.

76. Hartman, C., and Köditz, W.: Automated morphometric endothelial analysis combined with video specular microscopy. Cornea, 3: 155-167, 1984/1985.